Doctoral Dissertation
Doctoral Program in Energy Engineering (38^{th}cycle)

Heat Transfer Enhancement in Latent Heat Thermal Energy Storage Systems and High-Temperature Concentrating Solar Power Receivers

By

Arsham Mortazavi

******

Supervisor(s):
Prof. Eliodoro Chiavazzo, Supervisor
Prof. Pietro Asinari, Co-Supervisor
Prof. Matteo Morciano, Co-Supervisor

Doctoral Examination Committee:
Prof. Nicola Massarotti, Referee, Università degli Studi di Napoli "Parthenope"
Dr. Valeria Palomba, Referee, CNR–ITAE
Prof. Marcello Iasiello, Università di Napoli Federico II

Politecnico di Torino
2026

Declaration

I hereby declare that, the contents and organization of this dissertation constitute my own original work and does not compromise in any way the rights of third parties, including those relating to the security of personal data.

During the preparation of this work, the author used ChatGPT, an AI language model developed by OpenAI under the CC BY 4.0 license, to linguistically refine portions of the text. The author reviewed and edited all generated content as necessary and takes full responsibility for the final content.

Arsham Mortazavi
2026

* This dissertation is presented in partial fulfillment of the requirements for **Ph.D. degree** in the Graduate School of Politecnico di Torino (ScuDo).

This thesis is dedicated to my loving parents, whose endless support, sacrifices, and encouragement have shaped my life and made this achievement possible. I also dedicate this work to my beloved wife, whose love, patience, and constant support have accompanied me throughout this challenging yet rewarding journey.

Acknowledgements

I would like to express my deepest and most sincere gratitude to my supervisors, Prof. Eliodoro Chiavazzo, Prof. Pietro Asinari and Prof. Matteo Morciano, whose exceptional guidance, unwavering support, and constant encouragement have been fundamental throughout this journey. Their expertise, patience, and trust have not only shaped this research but have also contributed greatly to my personal and professional growth.

I would like to sincerely thank Prof. Federico Millo for his unwavering support and encouragement.

I would like to thank all my friends and colleagues at the multi-Scale ModeLing Laboratory (SMaLL) for their friendship, support, and for making this experience both rewarding and memorable.

Abstract

The continued rise in global energy demand, together with the need to limit greenhouse gas emissions, has increased interest in efficient renewable energy systems and reliable energy storage solutions. This trend calls for improvements in the efficiency and reliability of technologies based on renewable resources. In this context, concentrating solar power is particularly attractive, as it enables the production of high-temperature thermal energy. However, due to the intermittent nature of solar energy, thermal energy storage systems are essential to improve reliability and dispatchability. Among these, latent heat thermal energy storage systems are gaining attention due to their high energy density. Despite this potential, their widespread deployment remains limited by the very low thermal conductivity of phase-change materials, which results in slow charging and discharging rates.

This dissertation explores two approaches to improve heat transfer in concentrating solar power receivers and latent heat thermal energy storage systems. The first part focuses on the use of topology optimization to redesign the internal conductive structure of a compact latent heat thermal energy storage unit. The objective is to accelerate the phase-change process during discharge and achieve a more uniform temperature distribution without increasing the amount of highly conductive material. A density-based formulation is adopted, using the method of moving asymptotes together with adjoint sensitivity analysis to guide the optimization. The resulting design shows a measurable improvement in performance, reducing the time required to solidify 90% of the phase-change material (paraffin wax) by 12.3% compared to a well-performing reference case, while also promoting a more uniform temperature distribution.

The second part of the work examines the use of lattices based on triply periodic minimal surfaces to enhance heat transfer in concentrating solar power receivers. Four geometries—Diamond, Gyroid, SplitP, and Lidinoid—are analyzed numer-

ically in a tubular parabolic trough configuration under representative operating conditions. In addition to standard thermal metrics, entropy generation is used to assess thermodynamic performance. Based on these results, two designs—Diamond and SplitP—are selected for further experimental investigation using additively manufactured planar receiver mock-ups tested in a high-flux solar simulator. The findings indicate that structures based on triply periodic minimal surfaces can improve heat removal while keeping pressure losses at acceptable levels. In particular, the SplitP and Lidinoid geometries show a favorable balance, with lower entropy generation, reduced peak temperatures, and thermal efficiencies above 70%. These two mock-ups are further examined through numerical simulations to gain deeper insight into the temperature distribution on the heated surface and to identify which Reynolds-averaged Navier-Stokes turbulence models best predict their performance.

Overall, the results show that carefully designed internal geometries—whether obtained through topology optimization or implemented as lattices based on triply periodic minimal surfaces—can lead to tangible improvements in heat transfer. These findings contribute to the ongoing development of more efficient concentrating solar power receivers and latent heat thermal energy storage systems.

Contents

List of Figures **x**

List of Tables **xv**

Nomenclature **xvii**

1 Introduction **1**

1.1 Global Energy Consumption and Production Trends 1

1.2 Environmental and Climate Impacts of Current Energy Use 3

1.3 Energy Transition and the Imperative of Energy Management 4

1.4 Concentrating Solar Power and Thermal Energy Storage 5

1.4.1 CSP Technologies 6

1.4.2 Thermal Energy Storage 8

1.4.3 Phase Change Materials 9

1.5 Motivation for Performance Enhancement 13

1.5.1 Strategies for Improving Heat Extraction in CSP Receivers . 14

1.5.2 Strategies for Improving the Specific Power in LHTES Systems 18

1.5.3 Thesis Overview 21

2 Methodology **23**

2.1 Part 1: Topology Optimization Approach 23

2.1.1 Introduction to Optimization 24
2.1.2 The Density Method 27
2.1.3 Method of Moving Asymptotes and its extension 28
2.1.4 Adjoint Sensitivity Analysis 35
2.1.5 Material Interpolation: SIMP 36
2.1.6 Regularization: Filtering and Projection 38
2.2 Part 2: TPMS Lattices 43

3 Topology Optimization of a LHTES System 46
3.1 Physical Model 46
3.2 Topology Optimization Procedure 50
3.2.1 Objective Function and Constraints 50
3.3 Finite Element Model 51
3.4 Grid Study 54
3.5 Results 56
3.6 Conclusions 62

4 Performance Enhancement in CSP Receivers 64
4.1 Line-focus Solar Receivers equipped with TPMS 64
4.1.1 Introduction 64
4.1.2 Simulation Setup and Boundary Conditions 66
4.1.3 Performance Assessment Methodology 71
4.1.4 Assessment of the Numerical Uncertainty 73
4.1.5 Results 75
4.2 Experimental Investigation of Point-focus Receivers with TPMS . . 81
4.2.1 Samples and Test Campaign 81
4.2.2 Experimental Procedure 86

4.2.3 Data Analysis 87
4.2.4 Analysis of Experimental Uncertainty 91
4.2.5 Results and Discussion 92
4.3 Numerical Investigation of Point-focus Receivers with TPMS 100
4.3.1 Numerical Model Setup and Boundary Conditions 100
4.3.2 Grid Study 103
4.3.3 Validation of the Results 105
4.3.4 Conclusions 108

5 Conclusions and Perspectives 111
5.1 Concluding Remarks 111
5.2 Perspectives 114
5.2.1 Artificial Intelligence-assisted Topology Optimization . . . 116

References 119

Appendix A Local Entropy Generation for the Turbulent Studies 142

Appendix B Benchmarking the Hydraulic Model of the Tubular Receivers against Experimental Data 144

List of Figures

1.1 Yearly global energy consumption from 1900 to 2024. 2

1.2 Yearly global energy-related CO_2 emissions from 1900-2023. 3

1.3 Schematic representation of key CSP technologies. 6

1.4 Classification of PCMs based on their composition. 11

2.1 Schematic illustration of a generic MMA approximation for (a) positive and (b) negative gradients. 31

2.2 A generic example of mesh dependence with (a) 20×20, (b) 40×40, and (c) 200×200 elements. 38

2.3 An example of the numerical instability: formation of checkerboard patterns. 39

2.4 Algorithm for the topology optimization problem. 43

2.5 Studied TPMS lattices (a) Diamond (b) Gyroid (c) Lidinoid (d) SplitP. 44

3.1 Comparison of the outlet temperature of the HTF with experimental data. 47

3.2 Design of the LHTES mock-up. 48

3.3 Evolution of the topology optimization design: (a) Initial guess of the design, (b) Filtered density of the material, ρ_f, (c) Final 2D geometry, and (d) Extruded 3D geometry including simulation domains. The simplified reference geometry is shown in (e). To reduce computational cost, geometric symmetries were exploited, and only one-eighth of the device was simulated. 49

3.4 Apparent specific heat capacity of the investigated PCM, with shaded regions indicating the uncertainty in the fitted curves based on the data provided in Table 3.1. 53

3.5 Liquid volume fraction for different grids at t = 10 s. 55

3.6 A view of the chosen computational grid. 55

3.7 Performance comparison between the simplified reference model and the topology-optimized (TO) model: (a) Thermal energy released, (b) Thermal energy stored and liquid volume fraction of the PCM during (c) discharging and (d) charging. 56

3.8 Time to store or release 90% of the latent energy and achieve 90% melting or solidification of the PCM. The vertical axis is normalized by the corresponding t_{90} value of the reference case. 57

3.9 Liquid volume fraction of the PCM during solidification at (a) t = 15 s, (b) t = 30 s, and (c) t = 52 s; Temperature maps during solidification at (d) t = 15 s, (e) t = 30 s, and (f) t = 52 s. 58

3.10 Liquid volume fraction of the PCM during melting at (a) t = 40 s, (b) t = 80 s, and (c) t = 130 s; Temperature maps during solidification at (d) t = 40 s, (e) t = 80 s, and (f) t = 130 s. 59

3.11 Thermal Uniformity Index for (a) discharging and (b) charging processes. 61

3.12 Latent and sensible contributions during charging (left) and discharging (right) in the optimized device. 62

4.1 Geometry and boundary conditions of the studied section of solar receivers equipped with a TPMS lattice. 67

4.2 LCR distribution along the LS2 receiver circumferential angles obtained from Equation (4.11). 71

4.3 A scene of the grid for D20 in a cross-section perpendicular to the axis of the receiver at 6.15 cm from the beginning of TPMS insert . 75

4.4 Temperature maps for the average inlet temperature of 400 K, shown in a cross-section at the lattice outlet: (a) Diamond, (b) Gyroid, (c) SplitP, and (d) Lidinoid. For each lattice, the top half corresponds to the unit-cell size of 20 mm, while the bottom half corresponds to the unit-cell size of 10 mm. 76

4.5 Temperature distribution on the reflector-facing external surface of the receiver segments for an average inlet temperature of 400 K: (a) Diamond, (b) Gyroid, (c) SplitP, and (d) Lidinoid. For each lattice, the top half corresponds to a unit-cell size of 20 mm, while the bottom half corresponds to a unit-cell size of 10 mm. 77

4.6 Hotspot temperatures for the inlet temperatures of: (a) 400 K and (b) 550 K. 78

4.7 Impact of different average inlet temperatures on the performance of the Diamond, Gyroid, SplitP, and Lidinoid lattices. The column on the left corresponds to a unit-cell size of 10 mm, while the column on the right corresponds to a unit-cell size of 20 mm. (a) and (b) $\dot{N}_S$; (c) and (d) thermal efficiency; (e) and (f) exergy efficiency. 79

4.8 Pressure drop in the studied cases with the inlet temperature of 400 K. 80

4.9 Design plan of the samples (dimensions in millimeters) and 3D CAD longitudinal cross-sectional views of the receiver with (d) Diamond lattice and (e) SplitP lattice. 82

4.10 Pictures of the manufactured samples with (a) Diamond lattice and (b) SplitP lattice. 83

4.11 (a) Hexagonal arrangement of Xenon lamps (b) The test table. . . . 84

4.12 Sketch of the experimental test setup showing (a) the locations of TC_1 and TC_3 on the samples and (b) the front side of the mounted sample. 85

4.13 Heat flux distribution based on Equation (4.28), and the location of the sample for a heat flux level of (a) 100 kW/m^2 and (b) 325 kW/m^2 89

4.14 An example of a test session with the mass flow rate of 0.5 g/s for sample with SplitP lattice. The temperature increase is referred to room temperature. 94

4.15 Temperature rise (relative to the initial temperature) at TC_3 for (a) Diamond and (b) SplitP samples, and at the outlet for (c) Diamond and (d) SplitP samples 95

4.16 Temperature increase (with respect to initial temperatures) of the four thermocouples on the samples for (a) mass flow rate of 0.5 and incident heat of 200 W and (b) mass flow rate of 2 g/s and the incident heat of 270 W 96

4.17 Useful heat absorbed by the samples at different mass flow rates and incident heat fluxes for (a) Diamond and (b) SplitP samples. 97

4.18 Normalized heat loss for (a) Diamond and (b) SplitP samples, thermal efficiency for (c) Diamond and (d) SplitP samples, and exergetic efficiency for (e) Diamond and (f) SplitP samples. 99

4.19 Geometry and boundary conditions of the mock-ups: (a) overall view; cross-sectional view at the middle of the receiver with (b) SplitP lattice and (c) Diamond lattice. 102

4.20 Thermal efficiency comparison between experimental and numerical (from Lag EB κ-ε model) results for different mass flow rates for (a) SplitP lattice (b) Diamond lattice. 104

4.21 Comparison of numerical results obtained with different RANS turbulence models for (a) SplitP and (b) Diamond lattices. 105

4.22 Location of TC_2 and TC_4 for the receiver with (a) the Diamond and (b) the SplitP lattices 106

4.23 Temperature rise relative to the initial temperature for the SplitP lattice at (a) TC_2 and (b) TC_4, and for the Diamond lattice at (c) TC_2 and (d) TC_4. 107

4.24 (a) Hotspot temperatures of the mock-ups for the studied mass flow rates; temperature maps at a mass flow rate of 0.5 g/s for (b) SplitP and (c) Diamond lattices. 107

4.25 Comparison of useful heat between the two lattices obtained with the Lag EB κ-ε model. 108

B.1 Comparison of the hydraulic model of the tubular receivers equipped with TPMS with experimental data of Piatti et al. 145

List of Tables

2.1 Level-set equations of the analysed TPMS structures. 45

3.1 Material-dependent coefficients of Equation 3.3 for c_p^a of paraffin RT70HC. 54

3.2 Details of the grid study. 55

4.1 Hydraulic diameter, porosity, and wetted area of studied TPMS lattices based on the unit cell size. 66

4.2 Thermophysical properties of Syltherm-800 at different temperatures. 67

4.3 Coefficients of the LCR curve fitting from Kaloudis et al. 70

4.4 Comparison of different grids for D20 75

4.5 Values of the porosity, surface-to-volume ratio, and mass of the samples. 82

4.6 Tests information containing the test names and their corresponding mass flow rate and heat flux level. 88

4.7 Vertical locations of the studied heat flux levels and their corresponding incident heat. 89

4.8 Experimental error sources and their relative uncertainty. 91

4.9 Reynolds number of the tests. 93

4.10 Thermal efficiencies of different solar air heaters, in a mass flow rate range relevant to the present study. 98

4.11 Experimental test parameters measured during the campaign and used for model development. 101

4.12 Grid study for the Lag EB κ-ε RANS model 104

Nomenclature

Acronyms / Abbreviations

CPC Compound Parabolic Concentrator

CSP Concentrating Solar Power

DNI Direct Normal Irradiance

DNI Direct Normal Irradiance

FPC Flat Plate Collector

GCI Grid Convergence Index

GCMMA Globally Convergent Method of Moving Asymptotes

HCM Highly Conductive Material

IEA International Energy Agency

IRENA International Renewable Energy Agency

LCOE Levelized Cost of Energy

LCR Local Concentration Ratio

LFR Linear Fresnel Reflector

LHF Local Heat Flux

LHTES Latent Heat Thermal Energy Storage

MMA Method of Moving Asymptotes

PCM Phase-Change material

PTC Parabolic Trough Collector

PV Photovoltaic

RANS Reynolds-averaged Navier–Stokes

SHTES Sensible Heat Thermal Energy Storage

SIMP Solid Isotropic Material with Penalization

TCS Thermochemical Heat Storage

TEF Thermal Enhancement Factor

TES Thermal Energy Storage

TPMS Triply Periodic Minimal Surface

TUI Thermal Uniformity Index

Chapter 1

Introduction

The global energy landscape is undergoing a profound transformation driven by a complex interplay of economic growth, technological innovation, policy frameworks, and environmental imperatives. Over the past decades, rising energy demand has placed unprecedented pressure on existing energy systems. At the same time, the urgent need to mitigate climate change and ensure long-term energy security is accelerating the deployment of low-carbon technologies and reshaping investment priorities.

This chapter provides a comprehensive overview of the current state and evolving dynamics of global energy systems, beginning with an examination of consumption and production trends, followed by a discussion of the environmental consequences of prevailing energy practices, and concluding with the role of emerging technologies—particularly concentrating solar power and thermal energy storage—in enabling a sustainable and resilient energy future.

1.1 Global Energy Consumption and Production Trends

Global energy demand has been rising steadily due to population growth, industrialization, and the increasing electrification of end-use sectors. In 2024, total primary energy demand increased by 2.2%, significantly higher than the decade-long average of 1.3% [1] (see Figure 1.1). This growth was driven primarily by emerging and developing economies where industrial output and infrastructure development are expanding rapidly. Electricity demand, in particular, has grown disproportionately.

In 2024, global electricity consumption rose by 4.3%, representing the largest annual increase on record—an amount equivalent to the entire annual electricity demand of Japan [1]. This increase was largely attributed to extreme weather events (heating and cooling needs), rising digital infrastructure (including AI and data centers), and the ongoing electrification of transport and industrial processes.

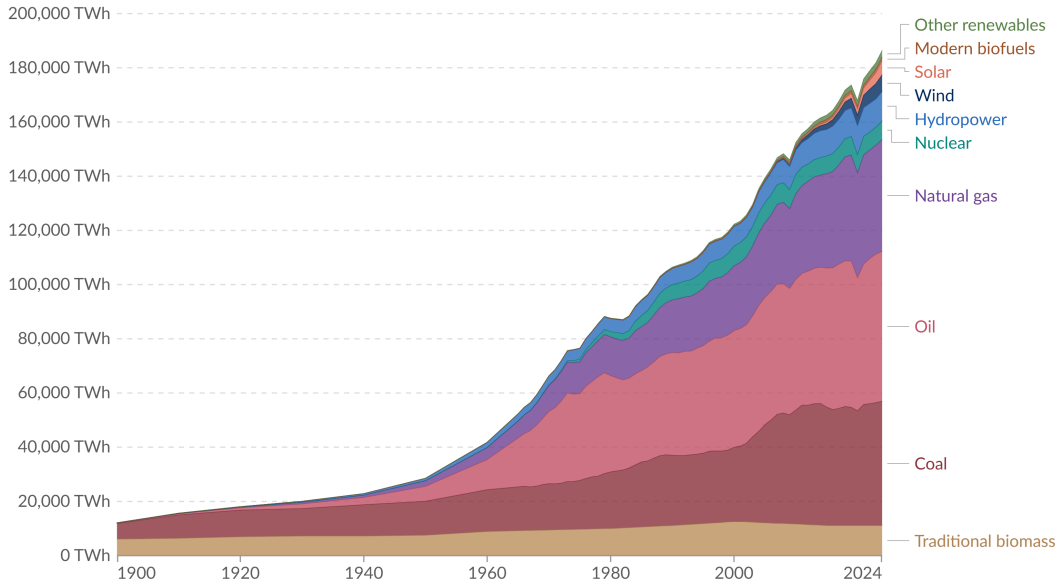


Fig. 1.1 Yearly global energy consumption from 1900 to 2024. Obtained from [2] based on data from [3].

Despite the growing deployment of renewable energy technologies, fossil fuels still supplied roughly 80% of global primary energy in 2023 [4]. However, in the power sector, the landscape is shifting: over 80% of the increase in electricity generation in 2024 was met by renewables and nuclear energy, signaling a clear momentum toward low-carbon sources [1]. According to the International Energy Agency (IEA), under current policy settings (the Stated Policies Scenario), fossil fuel demand is expected to peak before 2030, while renewables will dominate capacity additions and power sector investments [4]. According to the International Renewable Energy Agency's (IRENA) Renewable Capacity Statistics 2025, the world added 585 GW of renewable power in 2024, with cumulative renewable capacity reaching 4,448 GW—representing a 92.5% share of total capacity expansion and a 15.1% year-on-year increase, the fastest ever recorded [5].

1.2 Environmental and Climate Impacts of Current Energy Use

The prevailing reliance on fossil fuels has serious environmental and climatic consequences. In 2023, energy-related carbon dioxide (CO_2) emissions reached a record high of 37.4 Gt, representing an annual increase of 410 Mt compared to 2022 [6] (see Figure 1.2). Although the rate of emissions growth has slowed, current trajectories remain far above levels consistent with limiting global warming to 1.5 °C or even 2 °C above pre-industrial levels, as outlined in the Paris Agreement [4, 6].

Moreover, fossil fuel extraction and combustion contribute to severe air pollution, biodiversity loss, water contamination, and land degradation [7, 8], posing both environmental and public health risks [9].

The electricity sector is the single largest contributor to energy-related CO_2 emissions, accounting for approximately 40% of the total [6]. While the CO_2 intensity of electricity generation has started to decline, the absolute level of emissions remains dangerously high. The slow decarbonization of energy-intensive sectors—such as industry, transport, and buildings—further complicates climate mitigation efforts.

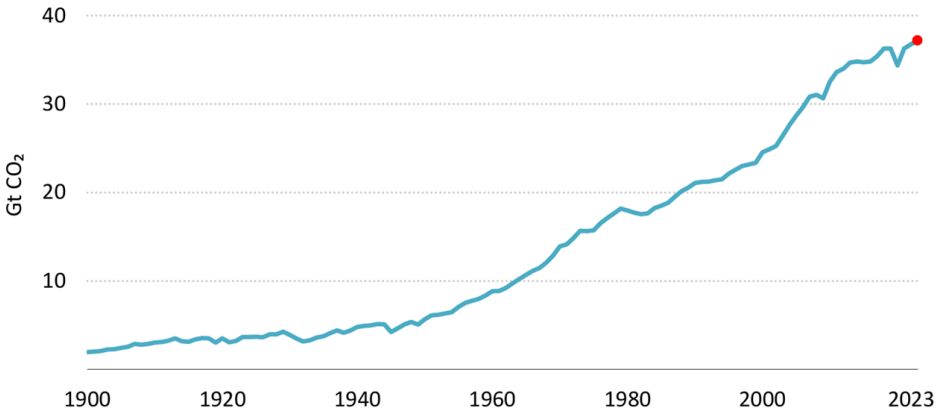


Fig. 1.2 Yearly global energy-related CO_2 emissions from 1900-2023. Derived from [6].

1.3 Energy Transition and the Imperative of Energy Management

The dual crises of climate change and energy security demand a comprehensive transformation of the global energy system. This transition rests on three interdependent pillars [4, 10, 11]:

1. Accelerated deployment of renewable energy technologies, particularly solar, wind, and hydropower;
2. Enhanced energy efficiency and integrated system planning, especially in electricity-intensive sectors;
3. Development and integration of robust energy storage and demand-side flexibility solutions, including thermal energy storage, battery systems, and smart grids.

Based on IRENA's *Capacity Statistics 2025* report, renewables accounted for 46.4% of electricity generation capacity worldwide in 2024, and 60.2% in Europe [5]. However, to meet the net-zero projections, total annual investments in clean energy must more than double—from approximately USD 1.8 trillion in 2023 to over USD 4.2 trillion by 2030, according to the IEA's *World Energy Outlook 2023* [10]. This highlights the urgency of continued research and innovation to improve the performance, efficiency, reliability, and integration of renewable energy technologies, which are central to the creation of stable and flexible low-carbon energy systems.

A successful energy transition must also be underpinned by sound energy management strategies that optimize energy production, conversion, distribution, and consumption. Effective energy management not only enhances system efficiency and reliability but also mitigates demand peaks, lowers emissions, and reduces operational costs. As renewable energy becomes a larger share of the energy mix, more sophisticated control and planning strategies will be essential to ensure system flexibility and resilience under variable and intermittent conditions.

1.4 Concentrating Solar Power and Thermal Energy Storage

Solar energy is the most abundant and universally available renewable energy resource on Earth [12]. Among various solar technologies, Concentrating Solar Power (CSP) holds significant promise due to its ability to generate high-temperature heat [13–15]. CSP systems use optical devices—such as parabolic trough collectors (PTCs), linear Fresnel reflectors (LFRs), or heliostat fields—to focus direct normal irradiance (DNI) onto a thermal receiver. The concentrated sunlight heats a working fluid (typically molten salts or thermal oil), which is then used to drive a thermodynamic cycle for electricity generation [16]. When coupled with Thermal Energy Storage (TES), CSP can deliver dispatchable electricity even after sunset, supporting both peak and base-load demands. This flexibility makes CSP a valuable solution for integrating higher shares of variable renewables like PV and wind into the grid. While primarily deployed in large-scale power plants, CSP also holds promise for industrial process heat, cogeneration, desalination, and small-scale applications relevant to developing regions [13].

Energy storage technologies are generally classified into five main categories: thermal, electrical, chemical, electrochemical, and mechanical storage systems [17]. Among these, TES is particularly important, as heat is involved in nearly 90% of global energy conversion, transfer, and storage processes [18]. Today, TES systems play a vital role in improving the dispatchability of CSP plants, making them a core component of modern CSP installations. TES technologies are especially well-suited for large-scale, long-duration energy storage—typically on the order of tens to hundreds of megawatts for several hours. In contrast, lithium-ion batteries, although widely deployed in combination with photovoltaic (PV) systems, are generally limited to shorter storage durations. For instance, a CSP plant equipped with molten salt storage can power a steam turbine for up to 10 hours, delivering approximately 1100 MWh of stored energy—nearly ten times the capacity of the largest lithium-ion battery systems currently installed for renewable energy integration [19]. Beyond CSP, TES systems are widely applicable in various sectors, including industrial process heating, space heating in buildings, and domestic hot water production [20]. They are also incorporated into Carnot batteries, where excess electricity is converted into heat, stored in a TES unit, and later reconverted into electricity when needed [21].

1.4.1 CSP Technologies

Currently, CSP technologies are classified into four main categories, based on how they concentrate solar radiation and the type of receiver system they employ [13]. Line-focus technologies, such as PTCs and LFRs, concentrate sunlight along a focal line. In contrast, point-focus technologies, including solar towers and parabolic dish reflectors, concentrate sunlight onto a single focal point. A schematic representation of these systems is shown in Figure 1.3.

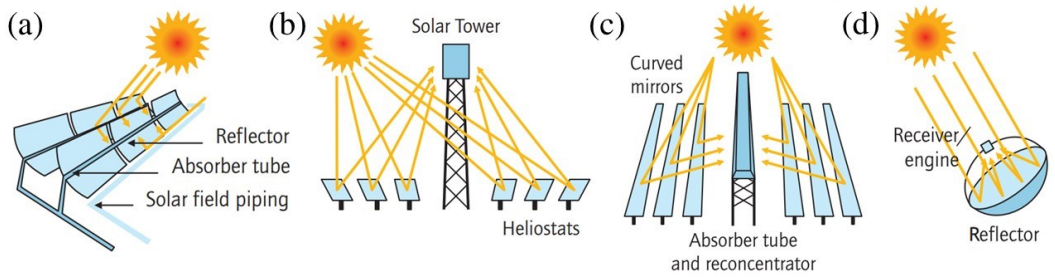


Fig. 1.3 Schematic representation of key CSP technologies: (**a**) parabolic trough collectors, (**b**) solar tower systems, (**c**) linear Fresnel reflectors, and (**d**) parabolic dish systems. Images adapted from Ref. [13].

Parabolic Trough Collectors

PTCs (Figure 1.3a) use mirrors curved along a single axis to concentrate sunlight onto a linear receiver tube. This tube, covered with a selective coating, is designed to absorb a high fraction of incoming solar radiation while minimizing thermal losses through infrared emission. To reduce convective and conductive heat losses, the receiver is enclosed within an evacuated glass envelope. Both the mirror and receiver tube track the sun's movement throughout the day to maintain optimal alignment.

The heat transfer fluid, typically synthetic oil, transports thermal energy from the collector field to heat exchangers, where it is used to preheat, evaporate, and superheat water. The resulting superheated steam drives a turbine connected to a generator to produce electricity. After condensation, the water is cycled back to the heat exchangers.

Parabolic trough technology is the most commercially developed among CSP systems and accounts for more than 82% of existing large-scale solar thermal power plants [22].

Solar Towers

Solar tower systems (Figure 1.3b), also known as central receiver systems, employ hundreds or even thousands of heliostats—sun-tracking mirrors—that reflect and concentrate sunlight onto a central receiver mounted atop a tall tower. In commercial applications, the receiver may use direct steam generation or molten salts, the latter serving as both the heat transfer fluid and the thermal energy storage medium.

Thanks to their high concentration ratios, solar towers can reach significantly higher temperatures than other CSP technologies. This leads to greater thermal-to-electric conversion efficiency. The system also offers a high degree of design flexibility, allowing for a wide range of heliostat types, receiver configurations, working fluids, and power block options. As of recent assessments, solar tower plants account for approximately 13 % of global CSP installations, making them the second most widely adopted CSP technology after parabolic trough systems [22].

Linear Fresnel Reflectors

LFR systems (Figure 1.3c) mimic the concentrating effect of PTCs by employing long rows of flat or slightly curved mirrors that direct sunlight onto a fixed, downward-facing linear receiver.

One of the primary advantages of this technology lies in its mechanical simplicity. The use of flexibly bent mirrors and stationary receivers reduces capital costs and enables direct steam generation, thereby eliminating the need for heat transfer fluids and intermediate heat exchangers. However, LFR systems generally exhibit lower thermal efficiency compared to PTCs, and their design presents greater challenges for integrating thermal energy storage [13].

Parabolic Dish Reflectors

Parabolic dish systems (Figure 1.3d) track the sun along two axes, focusing solar radiation onto a receiver positioned at the dish's focal point. The receiver absorbs the concentrated solar energy and transfers it as thermal energy to a circulating working fluid. This thermal energy can be converted into electricity either directly—using an integrated engine-generator—or transported via piping to a central power conversion unit.

These systems can achieve operating temperatures exceeding 1500 °C and typically reach concentration ratios between 600 and 2000, making them highly efficient in both thermal energy collection and power generation. Their modular design allows each dish-receiver unit to operate independently or as part of a larger, distributed array [23].

1.4.2 Thermal Energy Storage

TES systems are typically divided into three main categories based on their storage mechanism: sensible heat thermal energy storage (SHTES), latent heat thermal energy storage (LHTES), and thermochemical heat storage (TCS) [24].

Sensible Heat Thermal Energy Storage

SHTES is the most economically viable and technologically mature form of TES [25]. It operates by increasing or decreasing the temperature of a storage medium—such as molten salts, water, sand, or rocks—to store or release thermal energy. The quantity of energy stored depends on the material's specific heat capacity, the temperature variation during charging or discharging, and the mass of the medium [26]. SHTES systems are extensively investigated for a variety of applications, including space heating [27–29], industrial waste heat recovery [30–32], industrial process heat [33, 34], and solar energy utilization [35–37]. Despite its maturity and wide deployment [38], SHTES presents certain limitations. Achieving higher energy densities requires elevated storage temperatures, which leads to increased thermal losses through self-discharge. Furthermore, its inherently low energy density necessitates large storage volumes for meaningful capacity [24, 25].

Latent Heat Thermal Energy Storage

LHTES, by contrast, offers several advantages over SHTES. It provides significantly higher energy densities, allowing for more compact storage units tailored to specific applications. Moreover, LHTES systems release energy at nearly constant temperatures, making them ideal for temperature-sensitive processes [38]. Since heat can be stored and discharged at relatively low temperatures, heat losses are also minimized [39]. However, LHTES remains largely in the research and development

stage [25], signaling the need for continued exploration and offering considerable potential for technological advancement.

The core of LHTES systems lies in the use of phase-change materials (PCMs), which are broadly classified into organic, inorganic, and eutectic categories [26]. Among these, organic PCMs—particularly paraffins—are frequently used for medium-temperature applications [40]. They offer several practical advantages, including low supercooling, chemical stability, non-corrosiveness, and cost-effectiveness under diverse operating conditions [41, 42].

Thermochemical Energy Storage

TCS relies on the heat released or absorbed during reversible chemical reactions and/or sorption processes involving gases or vapors interacting with solids or liquids [43]. The endothermic reaction stage enables heat storage, while the exothermic stage facilitates its release [43]. Among the three main TES technologies, TCS offers the highest energy storage density. However, its development is still in early stages due to the technical complexity involved in implementing such systems [44]. Although still in the experimental stage, TCS systems show promise for real-world implementation by 2030 [25].

Key advantages of TCS include [44]:

- Long-term storage capability at ambient temperatures with minimal thermal losses
- High-temperature operation suitable for industrial and utility-scale applications
- Stable temperatures during charging and discharging, enhancing system performance and reliability

1.4.3 Phase Change Materials

Based on their composition, PCMs are classified as organic, inorganic, or eutectic substances capable of absorbing or releasing significant amounts of thermal energy during phase transitions. PCMs undergoing solid–gas or liquid–gas phase transitions have limited use in TES systems due to significant volume changes during the

transition, despite their high latent heat storage capacity. Solid–liquid PCMs are the most extensively studied category due to their favorable characteristics, including minimal volume change during phase transition, moderate design flexibility, cost-effectiveness, and relatively high energy storage density [45].

Thermal energy is stored and released during the solid–liquid and liquid–solid phase changes, respectively. These materials can undergo thousands of such cycles without significant degradation, maintaining their ability to store latent heat effectively over time [46].

PCMs have also been widely used in cold storage systems for cooling and air-conditioning applications. In such systems, the PCM solidifies (freezes) at low temperatures during the charging process, while during discharge it provides the cooling effect.

The classification of PCMs based on their composition could be seen in Figure 1.4.

Organic PCMs

Organic PCMs are primarily composed of carbon-based compounds, which can originate from natural sources or be synthesized chemically. This category encompass a broad variety of materials, including paraffins, fatty acids, esters, and other organic compounds. Organic PCMs has been successfully utilized in numerous applications, such as space heating, electronic device cooling, refrigeration, solar heating, automotive systems, food processing and storage, and aerospace technologies [46].

Paraffin, composed of straight-chain hydrocarbons, is one of the most widely used organic PCMs due to its broad range of melting temperatures, chemical stability below 500 °C, homogeneous melting behavior, and its ability to form stable cores [47]. However, organic PCMs—such as paraffins—generally exhibit low thermal conductivity, which necessitates larger heat transfer surfaces to meet thermal demands. Additionally, they pose challenges related to flammability.

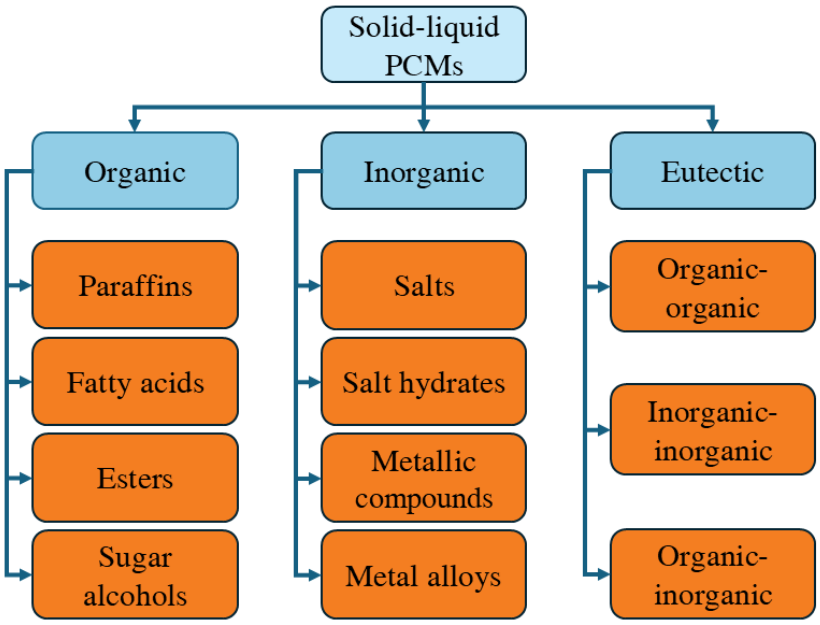


Fig. 1.4 Classification of PCMs based on their composition [48].

Inorganic PCMs

Inorganic phase change materials are primarily categorized into two types: salts and salt hydrates, and metals and their alloys. They offer advantages such as high latent heat per unit mass and volume, good cyclic stability, and relatively high thermal conductivity. However, salt hydrates are susceptible to phase segregation and subcooling, which can affect their performance. Additionally, the corrosive nature of inorganic salts poses a significant challenge [49], necessitating the use of high-grade containment materials—ultimately increasing system costs [47]. Another important characteristic of salts to consider is their inherently low thermal conductivity [50].

Another category of inorganic PCMs includes metals and metallic alloys. Their primary limitation lies in their low heat of fusion per unit mass, which results in a high weight penalty and has limited their widespread adoption as PCMs. Nevertheless, metals and metallic alloys offer promising potential for thermal energy storage, particularly in high-temperature applications, as they overcome several challenges associated with salt-based PCMs—including low thermal conductivity, significant supercooling, large volume changes during phase transitions, and corrosiveness. Despite their lower energy storage density, their stability and favorable thermal properties make them viable candidates in specific use cases [50].

Eutectic PCMs

Eutectic PCMs are homogeneous mixtures composed of two or more components—forming binary, ternary, or multicomponent systems—that are completely miscible in the liquid phase. They can be classified as organic–organic, inorganic–inorganic, or organic–inorganic systems. Eutectic PCMs melt at a unique temperature that is lower than the melting temperature of any individual constituent. This characteristic enables phase change temperature ranges that cannot be achieved by single-component PCMs, allowing precise tuning of the melting temperature and latent heat to meet specific thermal energy storage requirements through adjustment of the constituent weight ratios [48].

It has been reported that eutectic formulations can alleviate phase separation commonly observed in single-component salt hydrates by promoting more uniform melting and solidification behavior [48]. Although organic–inorganic eutectics are comparatively less explored, available studies suggest that such systems may exhibit complementary behavior, including enhanced latent heat of fusion and reduced supercooling and phase segregation, contributing to improved thermal stability [51].

Nevertheless, eutectic PCMs still face several limitations, including low thermal conductivity (particularly in organic–organic eutectic systems), as well as supercooling and residual phase separation, especially in salt-hydrate brine systems [48].

Limitations of PCMs

Although PCMs hold great promise for thermal energy storage, they also face some limitations [52]:

- **Low thermal conductivity:** Most phase change materials, particularly organic types, exhibit low thermal conductivity, which hinders heat transfer during phase transitions and results in prolonged charging and discharging times (i.e., low specific power).
- **Supercooling:** It is a phenomenon in which PCMs remain in the liquid state even below their melting point, potentially affecting the performance reliability of certain inorganic PCMs, such as salt hydrates.

- **Phase separation:** Phase separation may occur during melting and freezing cycles, particularly in eutectic and inorganic PCMs, which can ultimately lead to a reduction in their latent heat storage capacity.
- **Volume change:** During phase transitions, PCMs can experience significant volume changes, potentially causing material degradation or system instability over long-term use.
- **Temperature range:** PCMs have a limited working temperature, beyond which they may experience degradation.
- **Cost:** One of the primary limitations in the widespread adoption of PCMs, particularly advanced or high-performance types, is their cost.
- **Environmental impact:** One of the most significant challenges associated with PCM integration is leakage and the potential loss of material to the environment. Therefore, ensuring the non-toxicity of the PCM is critically important.

Paraffin wax is widely used in TES systems due to its negligible or absent supercooling, low toxicity, low vapor pressure, and good recyclability. It is also chemically stable and non-corrosive [48]. Although paraffin wax is considered an affordable PCM [48], it is still more expensive than salt hydrates [53].

1.5 Motivation for Performance Enhancement

The growing global energy demand, coupled with the detrimental environmental effects of conventional fossil fuels, underscores the urgent need to develop and implement renewable energy technologies. CSP and TES systems hold immense promise for delivering dispatchable and clean energy. However, their widespread adoption remains limited by factors such as relatively high capital and operational costs, system inefficiencies, and material limitations. Enhancing the performance of CSP and TES systems—particularly through the optimization or enhancement of heat transfer—can significantly improve their thermal and exergetic efficiencies. This, in turn, enhances system reliability and reduces the levelized cost of energy (LCOE), making these technologies more competitive with both conventional and

other renewable energy sources. Therefore, optimization and performance enhancement are essential for achieving the economic viability and long-term sustainability of solar thermal systems.

This section reviews the current challenges and limitations of CSP and TES technologies, highlighting recent advances and optimization strategies designed to enhance their performance and competitiveness.

1.5.1 Strategies for Improving Heat Extraction in CSP Receivers

To improve the efficiency of CSP technologies, numerous studies have explored various approaches, including the installation of inserts with different configurations inside the receiver to increase the heat transfer surface area and/or promote turbulence [54–56]; the use of alternative heat transfer fluids [57–59]; the application of nanofluids to enhance the thermal properties of HTFs [60, 61]; and the development of advanced coatings aimed at improving optical efficiency [62–64]. Furthermore, a number of studies have focused on receivers that are fully or partially filled with porous media to enhance heat transfer performance. For example, Wang et al. [65] examined the thermohydraulic performance of PTC receiver tubes partially and fully filled with high-porosity metal foams. They analyzed the effects of foam placement (top or bottom of the receiver) in the partially filled cases, geometric parameters, and porosity. In their optimal configuration, the Nusselt number increased by a factor of 5–10 compared to a smooth tube, although this was accompanied by a 10–20-fold increase in the friction factor.

Mwesigye et al. [66] evaluated the performance of a PTC receiver equipped with perforated-plate inserts, focusing on different plate diameters, orientation angles, and spacing, while maintaining a constant porosity of 0.65. Within the studied range of Reynolds numbers, temperatures, and geometric parameters, they reported a Nusselt number improvement exceeding 130%, accompanied by an increase in the friction factor of up to 95 times relative to a smooth receiver.

Liam et al. [67] investigated a novel tubular solar receiver for heating compressed air, incorporating a stainless steel shell filled with a porous medium. The study examined the influence of key design parameters—including the number of inlet pipes, as well as the porosity, length, and thermal conductivity of the porous medium—on the maximum receiver temperature and pressure drop. The optimal configuration

reduced the maximum receiver surface temperature by 75 K and the maximum porous medium temperature by 200 K compared to the reference case, while slightly increasing the outlet air temperature by 13 K. They also reported a significant increase in pressure drop for porosities below 0.6.

In an experimental study, Jamal-Abad et al. [68] studied a PTC receiver filled with copper metal foam. Although the incorporation of the porous medium reduced the overall heat loss coefficient by 45% and enhanced the thermal efficiency, it also resulted in a significant increase in the friction factor.

Heyhat and Zahi Khattar [69] investigated the effect of porous media (copper foam) placement in the receiver tube of a PTC on its thermal efficiency. The results showed that central placement increased thermal efficiency but caused higher pressure drops, whereas peripheral (annular) placement provided a better performance index by balancing efficiency and flow resistance. A higher pore density (20 PPI) further improved efficiency by about 2% compared to 10 PPI. Overall, incorporating porous foam increased thermal efficiency by 13–95% compared to a smooth receiver tube.

Savoldi et al. [70] conducted both numerical and experimental studies on the use of Raschig Rings as a porous medium in a planar solar receiver employing air as the heat transfer fluid. Their findings indicated that the tested configuration yielded a heat transfer enhancement by a factor of approximately 5 and achieved a Thermal Enhancement Factor (TEF) in the range of 2–2.5, in comparison to the receiver without Raschig Rings. Further investigating Raschig Rings as a porous medium, Ebadi et al. [71, 72] carried out experimental and numerical studies on tubular receivers. They observed that their unstructured porous inserts contributed to an increase in thermal efficiency. However, the inserts also led to the formation of dead zones where the flow became stagnant. The unstructured porous media affect the flow field at the macroscopic level by producing non-uniform velocity distributions with regions of significantly reduced flow velocities [73].

While unstructured porous inserts can substantially enhance thermal performance in receiver tubes, they also result in increased pressure drops, necessitating considerably higher pumping power. To address this issue, Tian et al. [74, 75] compared conventional unstructured porous media with structured lattice inserts. In their combined experimental and theoretical study, the adopted copper textile structures achieved thermal performance comparable to that of stochastic metal

foams (aluminum and copper-based) but required significantly lower pumping power. Moreover, the textile-based structures exhibited thermal efficiencies up to three times higher than those of copper foams with comparable mass.

In an experimental study, Ho et al. [76] investigated the use of structured porous lattices on the air side of a compact heat exchanger. Compared to conventional fin-tube heat exchangers, their novel design demonstrated a significantly higher heat transfer rate for the same pumping power.

According to the review by Sajjad et al. [77], lattice structures have emerged as a promising medium for enhancing the thermo-hydraulic performance of heat transfer systems, offering both improved heat transfer rates and reduced pressure drops. They have been successfully implemented in devices such as heat sinks, heat exchangers, and heat pipes, where their high surface area and thermal conductivity contribute to superior thermal performance. Compared to foams, lattices provide easier flow passages, resulting in significantly lower pressure drops and reduced pumping power, while maintaining competitive heat transfer capabilities. Furthermore, lattice-based thermal systems are typically lighter and possess greater mechanical strength. Compared to stochastic porous media, when heat dissipation and mass flow rate are fixed constraints, lattices enable the design of more compact and efficient heat exchangers [78].

Despite these promising outcomes, structured porous media used as inserts in solar receivers have received limited attention in the literature, highlighting the need for further research in this area.

The rapid advancement of additive manufacturing has enabled the fabrication of complex structured porous inserts with enhanced functional properties. Among these, triply periodic minimal surfaces (TPMS) have attracted significant research interest due to their promising thermal and hydraulic characteristics. Theoretically, TPMS are defined as zero-mean-curvature surfaces that repeat periodically in three principal directions [79]. TPMS can offer several advantages for solar receivers, making them promising candidates for enhancing the efficiency and durability of CSP systems:

- **Versatility in design, reduced material usage, and superior mechanical strength:** Additive manufacturing enables precise customization of TPMS geometries to meet specific thermal and mechanical requirements in CSP

applications [80]. These structures achieve high strength and thermal performance with less material; therefore, when incorporating porous media, TPMS can result in lighter and more cost-effective solar receivers. Their robust geometry [81] withstands high thermal stresses and harsh operating conditions, thereby extending service life and reducing maintenance needs.

- **High surface-area-to-volume ratio:** TPMS offer a large surface-area-to-volume ratio [82], which enhances heat transfer by enabling efficient absorption and uniform distribution of solar energy, thereby improving thermal performance.
- **Optimized fluid dynamics and improved heat transfer:** Owing to their continuous, non-intersecting surfaces, TPMS geometries promote streamlined fluid flow, reducing pressure drops and eliminating dead zones [83], which enhances convective heat transfer while maintaining a low pressure drop [84]. Furthermore, TPMS enable more uniform heat distribution, minimizing hotspots and reducing thermal losses [85].

By leveraging these advantages, TPMS can substantially enhance the thermal efficiency, mechanical reliability, and overall performance of solar receivers, making them promising components for next-generation CSP systems.

Khalil et al. [86] compared the performance of two lattice structures based on specific TPMS topologies—Diamond and Gyroid—with three other lattice-based heat sink designs, concluding that the Diamond configuration exhibited superior thermal efficiency.

Modrek et al. [87] investigated the thermal performance of TPMS-based heat sinks, including effective thermal conductivity. Using topology optimization, they developed heat sinks and proposed two mapping strategies to transform porous cellular structures into Gyroid-based designs, subsequently analyzing and comparing heat transport behavior.

Yan et al. [88] experimentally evaluated the thermohydraulic performance of several TPMS lattices—Gyroid, Diamond, and Primitive—and their two-by-two combinations (Gyroid/Diamond, Diamond/Primitive, and Gyroid/Primitive). To assess overall performance, considering both pressure drop and heat transfer, they used the area goodness factor, defined as the ratio of the Colburn factor to the friction factor, across a range of air flow Reynolds numbers (400–1200). Their results

indicated that the Gyroid lattice achieved the highest ratio due to its low pressure drop, whereas the Diamond lattice attained the highest heat transfer coefficient. In another study, Modrek et al. [89] conducted a multi-objective optimization of four TPMS topologies—Gyroid, Diamond, Primitive, and I-WP—highlighting the strong potential of the Diamond structure for improving both thermal and mechanical performance in passive heat sinks.

Gajetti et al. [90] investigated heat sinks based on Gyroid and SplitP lattices for a one-side heating case study, with a very high heat flux. Both TPMS structures demonstrated a highly efficient heat removal effect with low hotspot temperature, especially if lattice unit cell size of the order of few millimetres were considered. Only recently the potential of TPMS lattices in CSP applications is raising interest: some very recent studies has addressed their adoption as volumetric solar receivers [91, 92]; however, their use as possible inserts in line focus applications has never being considered so far.

1.5.2 Strategies for Improving the Specific Power in LHTES Systems

A key drawback of PCMs—especially organic types—is their inherently low thermal conductivity, which leads to prolonged charging and discharging periods and, consequently, low specific power. To overcome this limitation, numerous studies have explored incorporating highly conductive nanoparticles into PCMs to improve their effective thermal conductivity.

Sahan et al. [93] examined paraffin–nanomagnetite (Fe_3O_4) composites with mass fractions of 10% and 20%, reporting thermal conductivity enhancements of 48% and 60%, respectively.

Bahiraei et al. [94] developed three paraffin-based nanocomposites containing carbon nanofibers, graphene nanoplatelets, and graphite nanopowder, with mass fractions between 2.5% and 10%. Their combined experimental and numerical analyses demonstrated that, although nanoparticle addition substantially increases the composite's thermal conductivity, it can also hinder natural convection during melting. This introduces a trade-off between enhanced thermal conductivity and the suppression of natural convection. Furthermore, repeated melting–solidification cycles can disturb

the uniform distribution of nanoparticles, while agglomeration and sedimentation over time may further degrade the composite's thermal performance [95].

Another widely adopted approach to improve the effective thermal conductivity of LHTES systems is the incorporation of metal matrices and porous structures. In this regard, Morciano et al. [40] developed a prototype LHTES unit featuring a 3D Cartesian metal lattice produced via additive manufacturing. The design specifically targeted the reduction of charging and discharging durations. Their innovative system achieved remarkable specific power values of 714 W/kg and 1310 W/kg for charging and discharging, respectively.

Ribezzo et al. [96] experimentally investigated a shell-and-tube LHTES prototype filled with copper wool. They examined the influence of varying fibre thicknesses and fibre placement around the LHTES tubes. Their findings showed up to a 16% decrease in melting time and substantial improvements in mean power output—53% during charging and 205% during discharging.

Ahmed et al. [97] experimentally investigated the performance of paraffin/copper foam and paraffin/iron–nickel foam composites. Both composites improved the thermal performance of paraffin, with the paraffin/copper foam composite exhibiting a more uniform temperature distribution and approximately 21% shorter charging time compared to the paraffin/iron–nickel foam composite. However, metal foams present certain drawbacks: fully impregnating all pores with PCM is difficult, and unfilled pores can act as thermal insulators. Moreover, these structures tend to restrict and suppress convective heat transfer [98].

Another approach to improving the thermal performance of PCMs is encapsulation. Encapsulated PCMs are classified by particle size into macro-, micro-, and nano-scale categories. Capsule size plays a crucial role in thermal behavior, with smaller capsules offering a higher surface-area-to-volume ratio, thereby enhancing heat transfer efficiency [99]. However, despite this advantage, PCM microencapsulation entails complex and costly manufacturing processes [100].

Rezaeishaker et al. [101] numerically investigated a novel fountain-shaped macrocapsule for latent heat storage. The proposed design outperformed conventional enclosures, reducing charging time by up to 43% compared to their previously optimized pear-shaped model.

Another commonly employed approach in the literature to mitigate the low thermal conductivity of PCMs is the incorporation of fins. Fins are widely used because they do not cause long-term degradation of the PCM or introduce safety concerns. As a result, the design and optimization of heat conduction channels with integrated fin structures have attracted considerable attention [102].

Zaib et al. [103] numerically investigated the effects of parameters such as fin number, length, and thickness on the total phase-change duration. Their optimized design achieved a 92% reduction in melting time.

Using a two-dimensional model, Zhang et al. [104] examined the impact of varying fin lengths and tilt angles on the melting behavior of PCMs. The heat transfer performance of fins is strongly influenced by their size, distribution, and geometry, rendering their design a complex task.

Due to the many interrelated variables, fins have been extensively studied [105]. However, research on finned structures is often characterized by complex physical phenomena and limited design flexibility, making it challenging to establish clear, fundamental design guidelines [106].

Topology optimization is a computational design methodology that determines structural layouts optimized for performance within specified design constraints. Unlike traditional approaches, it is not restricted by an initial topology, enabling superior performance compared to manually designed layouts based on engineering intuition and experience [107]. Originally introduced in structural mechanics to solve configuration problems, topology optimization was pioneered by Bendsøe and Kikuchi [108], whose work laid its foundation. The emergence of Additive Manufacturing, which allows the fabrication of the non-intuitive geometries generated by topology optimization, has further accelerated its adoption in the heat transfer community. This approach has been widely applied in the design of heat sinks [109–111] and is increasingly being explored for LHTES systems.

Using a density-based approach, Pizzolato et al. [106] applied topology optimization to a cylindrical LHTES system to maximize performance for three distinct objective functions. Their findings revealed design features and trends that would be difficult to identify using alternative design methods. In a subsequent study, Pizzolato et al. [112] incorporated the effects of natural convection in the liquid PCM into both the design process and performance assessment of a topology-optimized

LHTES unit. They observed that designs optimized for melting and those optimized for solidification displayed notably different characteristics.

Ait Laasri et al. [113] conducted topology optimization of a cylindrical LHTES unit, evaluating two distinct fin configurations: one with radial fin development and the other with axial fin development. Their results showed that the radial fin arrangement outperformed the axial design, reducing discharge time by up to 86.3 % compared to a finless shell-and-tube configuration.

Zhang et al. [102] applied topology optimization to a shell-and-tube LHTES system and determined an optimal fin volume ratio of 20 %, providing a balance between heat transfer performance and storage capacity. In a subsequent experimental study, they demonstrated that, compared to conventional longitudinal fins, the topology-optimized fins reduced PCM charging and discharging times by 46.8% and 47.1%, respectively. Zhang et al. [114] further investigated the influence of various optimization parameters on the design and performance of fins in a shell-and-tube LHTES system, offering a theoretical foundation for the application of topology optimization to fin distribution in such systems.

He et al. [105] implemented topology optimization on a cylindrical LHTES unit and experimentally compared three configurations: optimized fins, conventional fins, and no fins. Their results showed that the optimized design achieved approximately 68% and 25% higher heat transfer efficiency compared to the finless and conventional-fin configurations, respectively.

The literature demonstrates that topology optimization can significantly reduce charging and discharging times, underscoring its effectiveness.

1.5.3 Thesis Overview

In this thesis, two heat transfer enhancement techniques are investigated. The performance of CSP receivers is improved using TPMS lattices, while the discharge dynamics of a LHTES device are enhanced through topology optimization.

The methodology associated with the topology optimization approach, as well as the mathematical formulation of TPMS lattices, is presented in Chapter 2. The fin geometries obtained from the topology optimization and the performance of the corresponding LHTES device are discussed in Chapter 3. Chapter 4 presents the

numerical and experimental investigations of CSP receivers equipped with TPMS lattices. This chapter is divided into three parts: first, the numerical study of a segment of a line-focus receiver equipped with four different TPMS lattices is presented; second, the experimental and numerical analyses of a planar receiver are discussed. Finally, the last chapter (Chapter 5) summarizes the main conclusions and outlines perspectives for future research.

Chapter 2

Methodology

This chapter presents the methodology of the heat transfer enhancement techniques investigated in this monograph. It begins with topology optimization, which is employed to enhance the power capacity of a LHTES system, and is followed by an introduction to TPMS lattices used in CSP receivers.

2.1 Part 1: Topology Optimization Approach

Topology optimization determines how material should be distributed within a prescribed design domain to minimize or maximize a given objective function. Originally developed for structural design applications, the method has since been extended to a wide range of disciplines, including thermofluids, acoustics, and other physics-based optimization problems.

In contrast to other structural optimization approaches, such as sizing and shape optimization, topology optimization offers complete design freedom. In this approach, the design evolves freely within a predefined design domain. The initial design domain does not need to be close to optimal; it only serves to accommodate the applied loads, boundary conditions, and design constraints. The topology optimization algorithm subsequently creates or removes holes within the domain and modifies boundary shapes and structural element sizes according to the specified objective functions and constraints. This high degree of design freedom often leads to non-intuitive topologies, shapes, and configurations, highlighting the supe-

rior exploratory capability of topology optimization compared to sizing and shape optimization.

The following section of this chapter introduces the fundamental concepts of topology optimization and establishes a common foundation for all design studies presented in this thesis.

2.1.1 Introduction to Optimization

An optimization problem is generally defined by three key components: the design variables, the objective function, and a set of constraints. The mathematical formulation of a general optimization problem can be stated as follows [115]:

$$\begin{aligned} \underset{\theta}{\text{Minimize}} \quad & f(\Theta) \\ \text{Subject to} \quad & G_j(\Theta) - g_i \leq 0, \qquad j = 1,\ldots,M \\ & \theta_i^L \leq \theta_i \leq \theta_i^U, \qquad i = 1,\ldots,N \end{aligned} \tag{2.1}$$

Where $f(\Theta)$ is the objective function, $G_j(\Theta) - g_i \leq 0,\ j = 1,\ldots,M$ are the constraints and $\theta_i^L \leq \theta_i \leq \theta_i^U,\ i = 1,\ldots,N$ define the bounds of the design variables (θ_i). In this formulation, $\boldsymbol{\theta}$ denotes the vector of design variables ($\boldsymbol{\theta} = \{\theta_1, \theta_2, \ldots, \theta_N\}$), and the admissible design space Θ is defined by these bounds and constraints, representing the allowable range of values for the design variables, such that $\boldsymbol{\theta} \in \Theta$.

The aim is to identify the values of the design variables that minimize or maximize the objective function while satisfying the specified constraints.

Optimization algorithms can be broadly classified into two main categories: gradient-based methods and non-gradient (derivative-free) methods. Each category is suited to different types of optimization problems and exhibits distinct characteristics.

The key feature of non-gradient solvers is that they do not require the computation of derivatives of the objective function with respect to the control variables. In fact, the objective function does not need to be differentiable at all. Because derivative-free solvers do not rely on local, pointwise information to guide the search for improved control variable updates, they instead depend on evaluating the objective function at multiple locations in the design space. Although this sampling-based strategy is more computationally demanding than following a single optimization path, it is

generally more robust [116]. The common non-gradient optimization algorithms are Nelder-Mead [117], BOBYQA [118], COBYLA [119] and EGO [120].

A gradient-based solver advances through the control variable space by iteratively updating the design in directions determined by the local gradient of the objective function. Each new iterate is computed using derivative information evaluated at previously visited points. Therefore, a gradient-based solver requires the complete set of first-order derivatives of the objective function with respect to the discrete control variable degrees of freedom. The gradient can be computed using different approaches. In general, the Adjoint method is the most efficient, followed by the Forward method. The purely Numeric method is the most computationally expensive, as it relies on repeated solutions of the full multiphysics problem. Although the Adjoint method is essential for problems with a large number of control variables (such as topology optimization), it is not applicable in all cases and can be less efficient than the Numeric method for transient problems with only a few controls [116]. The most commonly used gradient-based optimization algorithms include SNOPT [121], IPOPT [122], and MMA [123]. Among these, MMA (and its extension, GCMMA) is particularly well suited for problems involving a large number of control variables, such as topology optimization.

Optimization problems can be classified into different types, including sizing, shape and topology optimization.

In sizing optimization, a typical structural dimension is adjusted—for example, the thickness distribution of a beam or a plate. Accordingly, the design variables in such studies are sizing variables that define the cross-sectional dimensions. Here, the original structure from which the optimization evolves is assumed to be known a priori and the shape of the structure remains unchanged after the optimization.

Shape optimization involves deforming an existing geometry to improve its performance. In this approach, the optimization determines the configuration of the boundary, resulting in optimized layouts that remain topologically equivalent to the initial design. Consequently, the design variables are shape variables that characterize the variation of the existing boundaries.

Originally developed for mechanical design problems, topology optimization addresses the fundamental engineering problem of determining the optimal material distribution within a prescribed design domain to achieve the best structural performance. Therefore, the design variables are topology variables that define

the generalized material distribution, thereby allowing topological changes in the structure [115]. The concept has since been extended to a wide range of physical disciplines, including fluid dynamics, heat transfer, acoustics, electromagnetics, optics, and their combinations. The method relies on iterative cycles of analysis and design updates, typically guided by gradient-based computations [124].

Topology Optimization

Several advances in homogenization theory and numerical optimization methods laid the foundation for the seminal work on numerical topology optimization by Bendsøe and Kikuchi [108]. Since the introduction of the original "homogenization approach", the concept has evolved in multiple directions, including: (a) the density method (Bendsøe [125]; Zhou and Rozvany [126]; Mlejnek [127]), (b) the level-set method (Allaire et al. [128, 129]; Wang et al. [130]), (c) the topological derivative method (Sokołowski and Zochowski [131]), (d) the phase-field method (Bourdin and Chambolle [132]), and (e) evolutionary approaches (Xie and Steven [133]), among others. In general, density-based and evolutionary approaches rely on simple element- or node-based design variables, whereas the level-set method employs shape derivatives to generate the optimal topology [124]. Density-based approaches are relatively easy to implement and produce smooth, differentiable optimization problems that can be efficiently solved using well-established gradient-based methods such as the Method of Moving Asymptotes (MMA) [123]. Consistent with the literature, density–based approaches—particularly the Solid Isotropic Material with Penalization (SIMP) method—are among the most widely employed techniques in topology optimization.

A generic topology optimization problem (see Equation (2.2)) is defined as finding the material distribution that minimizes (or maximizes) a given objective function f, subject to a volume constraint $G_0 \leq 0$ and, if applicable, additional constraints $G_i \leq 0$ for $i = 1, \ldots, M$. The material distribution is represented by the design variable θ, which at any point in the design domain Ω can take the value 0 (void) or 1 (solid material). This optimization problem can be formulated as follows:

$$
\begin{aligned}
\underset{\boldsymbol{\theta}}{\text{Minimize}} \quad & f(\boldsymbol{u}(\boldsymbol{\theta}),\boldsymbol{\theta}) = \int_{\Omega} (F(\boldsymbol{u}(\boldsymbol{\theta}),\boldsymbol{\theta}))dV \\
\text{Subject to} \quad & \boldsymbol{R}(\boldsymbol{u}(\boldsymbol{\theta}),\boldsymbol{\theta}) = 0 \\
& G_0 = \int_{\Omega} \boldsymbol{\theta} dV - V_0 \leq 0 \\
& G_i(\boldsymbol{u}(\boldsymbol{\theta}),\boldsymbol{\theta}) \leq 0 \qquad i = 1,\ldots,M \\
& \theta(\boldsymbol{x}) = 0 \text{ or } 1. \qquad \forall \boldsymbol{x} \in \Omega
\end{aligned}
\tag{2.2}
$$

The vector $\boldsymbol{u}$ represents the degrees of freedom of the physical problem which are are the independent unknowns used to discretize the governing equations in a finite element analysis. In structural mechanics, these degrees of freedom are typically displacements, whereas in conductive heat transfer problems, $\boldsymbol{u}$ represents the discretized temperature field and collects the nodal temperature degrees of freedom resulting from the finite element approximation of the governing heat conduction equations. In Equation 2.2, $\boldsymbol{R}$ denotes the residual vector of the discretized governing equations, while V_0 represents the prescribed upper bound on the allowable material volume.

2.1.2 The Density Method

In the density-based concept, the two material phases are typically represented in a binary 0–1 fashion, often referred to as a black-and-white description, switching between solid material and void (or between two distinct material phases). However, this class of design problems is inherently ill-posed, as it often results in oscillatory, non-convergent solution sequences and has difficulties in efficiently handling multiple non-trivial constraints [124, 134].

Bendsøe and Kikuchi [108] proposed a method based on composites of a simple, predefined form, which allows the structure to be described by a density function taking values in the interval [0,1], rather than being restricted to the binary values 0 and 1. This approach relaxes the discrete optimization problem into a continuous one. In this framework, the material density function is constructed by considering a composite with an infinite number of infinitesimally small, periodically distributed holes. This reformulation converts the otherwise complex topology optimization

problem into a sizing problem. The homogenization method then makes it possible to compute the effective (macroscopic) properties of the composite, thereby enabling the determination of the optimal material distribution within the design domain.

Shortly after the homogenization approach to topology optimization was introduced, Bendsøe [125], followed by Zhou and Rozvany [126] and Mlejnek [127], proposed the SIMP , also known as the power-law approach. Initially, SIMP was introduced as a simplified and somewhat artificial means of reducing the complexity of the homogenization method and improving convergence toward 0–1 solutions. In this approach, the material distribution is represented by a continuous design variable, resembling a density of material, $0 \leq \theta \leq 1$, where 0 corresponds to void and 1 to solid material. The variable θ defines the normalized density across the design domain Ω, and serves as the optimization variable used to interpolate the material properties. The physical justification for this approach was later provided by Bendsøe and Sigmund [135].

The continuous topology optimization problem can be written as [124]:

$$\begin{aligned}
\underset{\boldsymbol{\theta}}{\text{Minimize}} \quad & f(\mathbf{u}(\boldsymbol{\theta}),\boldsymbol{\theta}) = \sum_j \int_{\Omega_j} (F(\mathbf{u}(\theta_j),\theta_j))dV \\
\text{Subject to} \quad & \boldsymbol{R}(\mathbf{u}(\boldsymbol{\theta}),\boldsymbol{\theta}) = 0 \\
& G_0 = \sum_j \int_{\Omega_j} \theta_j dV - V_0 \leq 0 \\
& G_i(\mathbf{u}(\boldsymbol{\theta}),\boldsymbol{\theta}) \leq 0 \qquad i = 1,\ldots,M \\
& 0 \leq \theta_j \leq 1 \qquad\quad j = 1,\ldots,N
\end{aligned} \tag{2.3}$$

2.1.3 Method of Moving Asymptotes and its extension

Topology optimization belongs to the class of optimization problems that involve a very large number of design variables, often reaching thousands—or millions—in practical applications. In such high-dimensional settings, non-gradient optimization methods become computationally prohibitive and therefore unsuitable [136]. As a result, topology optimization is almost exclusively solved using gradient-based methods, which can efficiently handle the large design space.

MMA is particularly well-suited for problems involving a large number of design variables, such as topology optimization [137, 116], and has become one of the most widely adopted algorithms within the topology optimization community.

The main idea of the MMA is to solve a sequence of simpler approximate sub-problems instead of the original nonlinear problem. In this approach, MMA addresses problems in the form of Equation (2.4) through an iterative scheme.

$$\begin{aligned} \underset{\boldsymbol{\theta}}{\text{Minimize}} \quad & G_0(\boldsymbol{\theta}) \\ \text{Subject to} \quad & G_i(\boldsymbol{\theta}) \leq 0 \qquad i = 1,\ldots,M \\ & \boldsymbol{\theta} \in \Theta = \left\{ \mathbb{R}^n \;\middle|\; \theta_{\min} \leq \theta_i \leq \theta_{\max}, \quad i = 1,\ldots,n \right\} \end{aligned} \tag{2.4}$$

At each iteration, the current point $\theta^{(k)}$ is taken as the reference. An approximating subproblem is then constructed by replacing the original functions $G_i(\theta)$, $(i = 0,\ldots,m)$ with convex and separable approximations $\tilde{G}_i^{(k)}(\theta)$. These approximations are primarily based on sensitivity information at the current point, but they also depend on iteration-specific parameters $U_j^{(k)}$ and $L_j^{(k)}$, referred to as "moving asymptotes" which are updated using information from previous iterations. The subproblem is solved to obtain a unique optimal solution, which defines the next iteration point $\theta^{(k+1)}$. This process is then repeated until convergence.

At iteration k, the MMA subproblem is formulated as [138]:

$$\begin{aligned} \underset{\boldsymbol{\theta}}{\text{Minimize}} \quad & \tilde{G}_0^{(k)} \\ \text{Subject to} \quad & \tilde{G}_i^{(k)} \leq 0 \qquad\qquad i = 1,\ldots,m \\ & \alpha_j^{(k)} \leq \theta_j \leq \beta_j^{(k)} \qquad j = 1,\ldots,n \end{aligned} \tag{2.5}$$

In this subproblem, the approximation functions are chosen as

$$\tilde{G}_i^{(k)}(\boldsymbol{\theta}) = \sum_{j=1}^{n} \left(\frac{p_{ij}^{(k)}}{U_j^{(k)} - \theta_j} + \frac{q_{ij}^{(k)}}{\theta_j - L_j^{(k)}} \right) + r_j^{(k)}, \qquad i = 0,1,\ldots,m \tag{2.6}$$

where

$$p_{ij}^{(k)} = \left(U_j^{(k)} - \theta_j^{(k)}\right)^2 \left(1.001 \left(\frac{\partial G_i}{\partial \theta_j}(\boldsymbol{\theta}^{(k)})\right)^+ + 0.001 \left(\frac{\partial G_i}{\partial \theta_j}(\boldsymbol{\theta}^{(k)})\right)^- + \frac{10^{-5}}{x_j^{\max} - x_j^{\min}}\right), \quad (2.7)$$

$$q_{ij}^{(k)} = \left(\theta_j^{(k)} - L_j^{(k)}\right)^2 \left(0.001 \left(\frac{\partial G_i}{\partial \theta_j}(\boldsymbol{\theta}^{(k)})\right)^+ + 1.001 \left(\frac{\partial G_i}{\partial \theta_j}(\boldsymbol{\theta}^{(k)})\right)^- + \frac{10^{-5}}{x_j^{\max} - x_j^{\min}}\right), \quad (2.8)$$

$$r_i^{(k)} = G_i\left(\boldsymbol{\theta}^{(k)}\right) - \sum_{j=1}^{n} \left(\frac{p_{ij}^{(k)}}{U_j^{(k)} - \theta_j^{(k)}} + \frac{q_{ij}^{(k)}}{\theta_j^{(k)} - L_j^{(k)}}\right). \quad (2.9)$$

In equations (4.8) and (2.8), $\left(\frac{\partial G_i}{\partial \theta_j}(\Theta^{(k)})\right)^+$ denotes the maximum of $\frac{\partial G_i}{\partial \theta_j}(\Theta^{(k)})$ and 0, while $\left(\frac{\partial G_i}{\partial \theta_j}(\Theta^{(k)})\right)^-$ denotes the maximum of $-\frac{\partial G_i}{\partial \theta_j}(\Theta^{(k)})$ and 0.

The lower and upper move limits—$\alpha^{(k)}$ and $\beta^{(k)}$, respectively—in Equation (2.5), prevent division by zero when solving the subproblem and must be chosen such that $L_j^{(k)} < \alpha_j^{(k)} < s_j^{(k)} < \beta_j^{(k)} < U_j^{(k)}$ [123]. A commonly adopted choice is [138]:

$$\begin{aligned} \alpha_j^{(k)} &= max\left(\theta_{min},\, L_j^{(k)} + 0.1(\theta_j^{(k)} - L_j^{(k)}),\, \theta_j^{(k)} - \Delta\theta(\theta_{max} - \theta_{min})\right) \\ \beta_j^{(k)} &= min\left(\theta_{max},\, U_j^{(k)} - 0.1(U_j^{(k)} - \theta_j^{(k)}),\, \theta_j^{(k)} + \Delta\theta(\theta_{max} - \theta_{min})\right), \end{aligned} \quad (2.10)$$

where $\Delta\theta$ denotes a user-defined relative step size.

U_i and L_i are positive parameters that define the range within which the approximation of G remains valid for the optimization problem. These parameters act as vertical asymptotes for the approximation of G, which gives the algorithm its name. For each iteration k, the local bounds $U_i^{(k)}$ and L_i^k are defined such that $\tilde{G}^{(k)} \to \infty$ as $\theta_i \to U_i^{(k)}$ for increasing functions, and as $\theta_i \to L_i^{(k)}$ for decreasing functions (see Figure 2.1). The values of $U_i^{(k)}$ and $L_i^{(k)}$ are specific to each design variable and are dynamically updated throughout the optimization process.

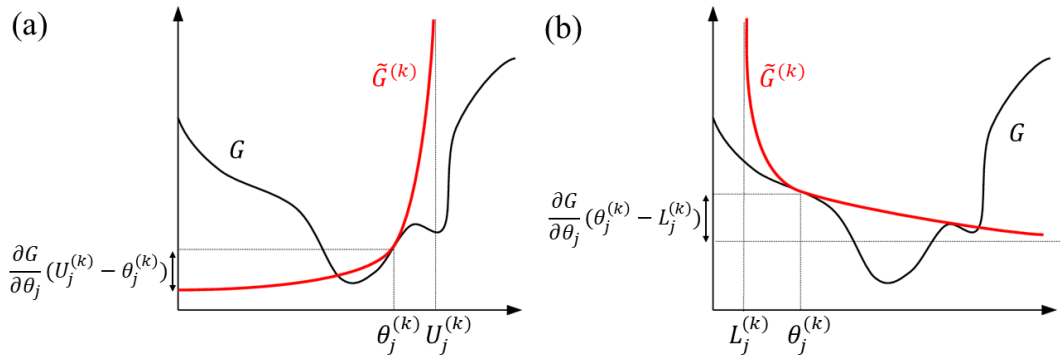


Fig. 2.1 Schematic illustration of a generic MMA approximation for (a) positive and (b) negative gradients, adapted and modified from [139].

The upper and lower asymptotes for the first two iterations ($k = 1$ and $k = 2$) are calculated as follows:

$$\begin{aligned} L_j^{(k)} &= \theta_j^{(k)} - 0.5\left(\theta_j^{max} - \theta_j^{min}\right), \\ U_j^{(k)} &= \theta_j^{(k)} + 0.5\left(\theta_j^{max} - \theta_j^{min}\right) \end{aligned} \tag{2.11}$$

and for $k \geq 3$:

$$\begin{aligned} L_j^{(k)} &= \theta_j^{(k)} - \gamma_j^{(k)}\left(\theta_j^{(k-1)} - L_j^{(k-1)}\right), \\ U_j^{(k)} &= \theta_j^{(k)} + \gamma_j^{(k)}\left(U_j^{(k-1)} - \theta_j^{(k-1)}\right), \end{aligned} \tag{2.12}$$

where

$$\gamma_j^{(k)} = \begin{cases} 0.7 & \text{if} \quad \left(\theta_j^{(k)} - \theta_j^{(k-1)}\right)\left(\theta_j^{(k-1)} - \theta_j^{(k-2)}\right) < 0, \\ 1.2 & \text{if} \quad \left(\theta_j^{(k)} - \theta_j^{(k-1)}\right)\left(\theta_j^{(k-1)} - \theta_j^{(k-2)}\right) > 0, \\ 1 & \text{if} \quad \left(\theta_j^{(k)} - \theta_j^{(k-1)}\right)\left(\theta_j^{(k-1)} - \theta_j^{(k-2)}\right) = 0. \end{cases} \tag{2.13}$$

as long as this yields values that satisfy

$$\begin{aligned} L_j^{(k)} &\leq \theta_j^{(k)} - 0.01\left(\theta_j^{max} - \theta_j^{min}\right), \\ L_j^{(k)} &\geq \theta_j^{(k)} - 10\left(\theta_j^{max} - \theta_j^{mi)}\right), \\ U_j^{(k)} &\geq \theta_j^{(k)} + 0.01\left(\theta_j^{max} - \theta_j^{min}\right), \\ U_j^{(k)} &\leq \theta_j^{(k)} + 10\left(\theta_j^{max} - \theta_j^{min}\right). \end{aligned} \tag{2.14}$$

If any of these bounds is violated, the corresponding $L_j^{(k)}$ or $U_j^{(k)}$ is assigned to the right-hand side of the violated inequality. A schematic illustration of a generic MMA approximation for a function G at point $\theta_j^{(k)}$ could be seen in Figure 2.1.

A central feature of the MMA algorithm is its use of separable and convex approximations. Separable approximations ensure that the necessary optimality conditions of the subproblems do not couple the design variables, while convexity allows the subproblems to be efficiently solved using dual or primal–dual methods. At each iteration, the parameters U_i and L_i associated with each function are updated based on the history of previous iterations, guiding the approximations to remain valid and improving convergence toward the optimal solution.

Although the MMA is widely recognized for its effectiveness in solving optimization problems, it has a key limitation: its convergence is not guaranteed, which can occasionally lead to unsatisfactory results in practice [140]. To address this, Svanberg [138] further extended MMA method to a globally convergent version termed as GCMMA. GCMMA incorporates inner iterations, making the approximations of the objective and constraint functions more conservative to ensure global convergence to a Karush-Kuhn-Tucker point [141].

Globally Convergent Version of MMA

GCMMA, when applied to problems of the form Equation (2.4), involves both outer and inner iterations, denoted by the indices k and ν, respectively. Each outer iteration may include zero, one, or multiple inner iterations. The double index (k,ν) refers to the ν-th inner iteration within the k-th outer iteration.

At each outer iteration, the functions $G_i(\boldsymbol{\theta})$ are replaced by convex approximations, resulting in a subproblem $\tilde{G}_i^{(k,0)}(\boldsymbol{\theta})$. The optimal solution of this subproblem is denoted $\hat{\boldsymbol{\theta}}^{(k,0)}$. If $\tilde{G}_i^{(k,0)}(\hat{\boldsymbol{\theta}}^{(k,0)}) \geq G_i(\hat{\boldsymbol{\theta}}^{(k,0)})$, for all $i = 0,1,\ldots,n$, then the next iteration point is set as $\boldsymbol{\theta}^{(k+1)} = \hat{\boldsymbol{\theta}}^{(k,0)}$ and the outer iteration is completed without any inner iterations. If this condition is not satisfied, an inner iteration is performed. This involves generating a new subproblem at $\boldsymbol{\theta}^{(k)}$ with updated approximating functions $\tilde{G}_i^{(k,1)}(\boldsymbol{\theta})$, which are more conservative than $\tilde{G}_i^{(k,0)}(\boldsymbol{\theta})$ for the indices where the inequality was violated. Formally, $\tilde{G}_i^{(k,1)}(\boldsymbol{\theta}) > \tilde{G}_i^{(k,0)}(\boldsymbol{\theta})$, for all $\boldsymbol{\theta} \in \boldsymbol{\Theta}^{(k)}$, except for $\boldsymbol{\theta} = \boldsymbol{\theta}^{(k)}$, where $\tilde{G}_i^{(k,1)}(\boldsymbol{\theta}^{(k)}) = \tilde{G}_i^{(k,0)}(\boldsymbol{\theta}^{(k)})$. The optimal solution of this subproblem is denoted $\hat{\boldsymbol{\theta}}^{(k,1)}$. If $\tilde{G}_i^{(k,1)}(\hat{\boldsymbol{\theta}}^{(k,1)}) \geq G_i(\hat{\boldsymbol{\theta}}^{(k,1)})$, for all $i =$

$0,1,\ldots,n$, then the next iteration point is $\boldsymbol{\theta}^{(k+1)} = \hat{\boldsymbol{\theta}}^{(k,1)}$ completing the outer iteration with one inner iteration. If the condition is still not met, additional inner iterations are performed in the same manner until $\tilde{G}_i^{(k,v)}(\hat{\boldsymbol{\theta}}^{(k,v)}) \geq G_i(\hat{\boldsymbol{\theta}}^{(k,v)})$, for all $i = 0,1,\ldots,n$, which is guaranteed to occur after a finite (usually small) number of inner iterations. The next iteration point is then set as $\boldsymbol{\theta}^{(k+1)} = \hat{\boldsymbol{\theta}}^{(k,v)}$ and the outer iteration is completed with v inner iterations [138].

It is important to note that in each inner iteration there is no need to recalculate the sensitivities, since $\boldsymbol{\theta}^{(k)}$ remains unchanged. The gradients of the original functions G_i are therefore computed only once per outer iteration.

The GCMMA subproblem for $k \in \{1,2,3,\ldots\}$ and $v \in \{0,1,2,\ldots\}$ takes the form:

$$\begin{aligned} \underset{\boldsymbol{\theta}}{\text{Minimize}} \quad & \tilde{G}_0^{(k,v)} \\ \text{Subject to} \quad & \tilde{G}_0^{(k,v)} \leq 0 \qquad\qquad i = 1,\ldots,m \\ & \alpha_j^{(k)} \leq \theta_j \leq \beta_j^{(k)} \qquad j = 1,\ldots,n \end{aligned} \tag{2.15}$$

The approximating function for this subproblem is chosen as:

$$\tilde{G}^{(k,v)}(\boldsymbol{\theta}) = \sum_{j=1}^{n} \left(\frac{p_{ij}^{(k,v)}}{U_j^{(k)} - \theta_j} + \frac{q_{ij}^{(k,v)}}{\theta_j - L_j^{(k)}} \right) + r_i^{(k,v)}, \qquad i = 0,1,\ldots,m \tag{2.16}$$

where

$$p_{ij}^{(k,v)} = \left(U_j^{(k)} - \theta_j^{(k)}\right)^2 \left(1.001 \left(\frac{\partial G_i}{\partial \theta_j}(\boldsymbol{\theta}^{(k)}) \right)^+ + 0.001 \left(\frac{\partial G_i}{\partial \theta_j}(\boldsymbol{\theta}^{(k)}) \right)^- + \frac{\rho_i^{(k,v)}}{x_j^{\max} - x_j^{\min}} \right), \tag{2.17}$$

$$q_{ij}^{(k,v)} = \left(\theta_j^{(k)} - L_j^{(k)}\right)^2 \left(0.001 \left(\frac{\partial G_i}{\partial \theta_j}(\boldsymbol{\theta}^{(k)}) \right)^+ + 1.001 \left(\frac{\partial G_i}{\partial \theta_j}(\boldsymbol{\theta}^{(k)}) \right)^- + \frac{\rho_i^{(k,v)}}{x_j^{\max} - x_j^{\min}} \right), \tag{2.18}$$

$$r_i^{(k,\nu)} = G_i\left(\boldsymbol{\theta}^{(k)}\right) - \sum_{j=1}^{n}\left(\frac{p_{ij}^{(k,\nu)}}{U_j^{(k)} - \theta_j^{(k)}} + \frac{q_{ij}^{(k,\nu)}}{\theta_j^{(k)} - L_j^{(k)}}\right). \tag{2.19}$$

$\tilde{G}^{(k,\nu+1)}(\boldsymbol{\theta})$ is considered a more conservative approximation than $\tilde{G}^{(k,\nu)}(\boldsymbol{\theta})$ whenever $\rho_i^{(k,\nu+1)} > \rho_i^{(k,\nu)}$.

In outer iterations, the bounds $\alpha_j^{(k)}$ and $\beta_j^{(k)}$, as well as the asymptotes $L_j^{(k)}$ and $U_j^{(k)}$, are updated as in the original MMA, with the Equations (2.10)-(2.14) remaining valid. The parameters $\rho_i^{(k,\nu)}$ appearing Equations (2.17) and (2.18) are strictly positive and are updated according to the procedure described below.

Within an outer iteration k, the inner iterations differ only in the values of these parameters. At the start of each outer iteration, when $\nu = 0$, the following default values are assigned:

$$\rho_i^{(k,0)} = \frac{0.1}{n}\sum_{j=1}^{n}\left|\frac{\partial G_i}{\partial \theta_j}\left(\boldsymbol{\theta}^{(k)}\right)\right|\left(\theta_j^{max} - \theta_j^{min}\right), \qquad \text{for } i = 0,\ 1,\ \ldots,\ m \tag{2.20}$$

If any of the right-hand sides in Equation (2.20) is less than 10^{-6}, the corresponding $\rho_i^{(k,0)}$ is assigned the value 10^{-6}. $\rho_i^{(k,\nu)}$ is further updated as in:

$$\rho_i^{(k,\nu+1)} = \begin{cases} min\left\{1.1(\rho_i^{(k,\nu)} + \delta_i^{(k,\nu)}),\ 10\rho_i^{(k,\nu)}\right\} & \text{if } \delta_i^{(k,\nu)} > 0 \\ \rho_i^{(k,\nu)} & \text{if } \delta_i^{(k,\nu)} \leq 0. \end{cases} \tag{2.21}$$

$\delta_i^{(k,\nu)}$ is calculated as:

$$\delta_i^{(k,\nu)} = \frac{G_i\left(\hat{\boldsymbol{\theta}}^{(k,\nu)}\right) - \tilde{G}_i^{(k,\nu)}\left(\hat{\boldsymbol{\theta}}^{(k,\nu)}\right)}{d^{(k)}\left(\hat{\boldsymbol{\theta}}^{(k,\nu)}\right)}, \tag{2.22}$$

where

$$d^{(k)}(\boldsymbol{\theta}) = \sum_{j=1}^{n}\frac{\left(U_j^{(k)} - L_j^{(k)}\right)\left(\theta_j - \theta_j^{(k)}\right)^2}{\left(U_j^{(k)} - \theta_j\right)\left(\theta_j - L_j^{(k)}\right)\left(\theta_j^{max} - \theta_j^{min}\right)}. \tag{2.23}$$

Since the parameters $\rho_i^{(k,\nu)}$ are strictly positive, the functions $\tilde{G}_i^{(k,\nu)}$ are strictly convex. This implies that the GCMMA subproblem always has a unique optimal solution.

As seen in this section, a gradient-based optimization approach requires the computation of derivatives of both the objective function and the constraints with respect to the design variables. Topology optimization belongs to a class of optimization problems characterized by a large number of design variables and relatively few constraints. For such problems, the adjoint method is generally the most efficient approach for performing sensitivity analysis [106, 112, 116].

2.1.4 Adjoint Sensitivity Analysis

Sensitivity analysis involves evaluating the influence of one or more system parameters, θ_j, on one or several variables, G_i, which characterize the behavior of the system. Sensitivity analysis can be categorized into numerical and analytical methods. Central differencing is one of the most widely used numerical approaches which approximates the gradient $\mathrm{d}G_i/\mathrm{d}\theta_j$ as follows:

$$\frac{\mathrm{d}G_i}{\mathrm{d}\theta_j} \approx \frac{G_i(\theta_j+\varepsilon_{\theta_j}) - G_i(\theta_j-\varepsilon_{\theta_j})}{2\varepsilon_{\theta_j}}, \tag{2.24}$$

where ε_{θ_j} is a specified perturbation parameter. Central finite differencing is computationally intensive and its accuracy depends on the choice of ε_{θ_j}. In contrast, analytical approaches may be more tedious to develop than numerical methods, yet they are generally more accurate and often more computationally efficient [142].

The sensitivity of the vector of objective and constraint functions, $\boldsymbol{G}(\boldsymbol{u}(\boldsymbol{\theta}),\boldsymbol{\theta})$, with respect to design variables vector, $\boldsymbol{\theta}$, can be written as:

$$\frac{\mathrm{d}\boldsymbol{G}}{\mathrm{d}\boldsymbol{\theta}} = \frac{\partial \boldsymbol{G}}{\partial \boldsymbol{\theta}} + \left(\frac{\partial \boldsymbol{G}}{\partial \boldsymbol{u}}\right)^{\mathrm{T}} \frac{\mathrm{d}\boldsymbol{u}}{\mathrm{d}\boldsymbol{\theta}}. \tag{2.25}$$

The term $\mathrm{d}\boldsymbol{u}/\mathrm{d}\boldsymbol{\theta}$ can be calculated by differentiating the discretized form of the governing equations $\boldsymbol{R}(\boldsymbol{u},\boldsymbol{\theta}) = 0$.

$$\frac{\mathrm{d}\boldsymbol{R}}{\mathrm{d}\boldsymbol{\theta}} = 0 \Rightarrow \frac{\partial \boldsymbol{R}}{\partial \boldsymbol{\theta}} + \boldsymbol{J}\frac{\mathrm{d}\boldsymbol{u}}{\mathrm{d}\boldsymbol{\theta}}, \qquad \boldsymbol{J} = \frac{\partial \boldsymbol{R}}{\partial \boldsymbol{u}} \tag{2.26}$$

where $\boldsymbol{J}$ represents the Jacobian of the discretized governing equations. From Equations (2.25) and (2.26):

$$\frac{\mathrm{d}\boldsymbol{G}}{\mathrm{d}\boldsymbol{\theta}} = \frac{\partial \boldsymbol{G}}{\partial \boldsymbol{\theta}} - \left(\frac{\partial \boldsymbol{G}}{\partial \boldsymbol{u}}\right)^{\mathrm{T}} J^{-1} \frac{\partial \boldsymbol{R}}{\partial \boldsymbol{\theta}}, \tag{2.27}$$

which can be reformulated using transposition properties as:

$$\frac{\mathrm{d}\boldsymbol{G}}{\mathrm{d}\boldsymbol{\theta}} = \frac{\partial \boldsymbol{G}}{\partial \boldsymbol{\theta}} - \left(\underbrace{J^{-T}\left(\frac{\partial \boldsymbol{G}}{\partial \boldsymbol{u}}\right)}_{\text{Adjoint problem}}\right)^{\mathrm{T}} \frac{\partial \boldsymbol{R}}{\partial \boldsymbol{\theta}}. \tag{2.28}$$

The expression in brackets is referred to as the adjoint problem. To simplify the computations, the adjoint equation is introduced as [142]:

$$\left(\frac{\partial \boldsymbol{R}}{\partial \boldsymbol{u}}\right)^{\mathrm{T}} \boldsymbol{\lambda} = \frac{\partial \boldsymbol{G}}{\partial \boldsymbol{u}}, \tag{2.29}$$

where $\boldsymbol{\lambda}$ represents the vector of adjoint variables, or Lagrange multipliers. Accordingly, Equation (2.28) can now be rewritten as:

$$\frac{\mathrm{d}\boldsymbol{G}}{\mathrm{d}\boldsymbol{\theta}} = \frac{\partial \boldsymbol{G}}{\partial \boldsymbol{\theta}} - \boldsymbol{\lambda}^{\mathrm{T}} \frac{\partial \boldsymbol{R}}{\partial \boldsymbol{\theta}}. \tag{2.30}$$

Equation (2.29) does not depend on $\boldsymbol{\theta}$ making it is independent of the dimension of the optimization problem. It must be solved once for each optimization criterion, i.e., $G_i(\boldsymbol{\theta})$ for $i = 1, 2, \ldots, m$. Since in topology optimization problems the number of design variables is typically much larger than the number of criteria, the adjoint method is the preferred approach for sensitivity analysis. Furthermore, note that Equation (2.29) is linear, making the sensitivity analysis generally less computationally expensive than a forward analysis of nonlinear problems.

2.1.5 Material Interpolation: SIMP

As discussed in Section 2.1.2, solving the topology optimization problem is considerably more straightforward and stable when the material distribution is represented by a continuous design variable. This continuous $[0, 1]$ density representation requires a

differentiable relation between material properties and density, which ensures that both the physical response and the design sensitivities can be accurately computed. This density function is then the design variable [137]. It is required that the optimization results in a final design consisting almost entirely of regions with either material (1, or black) or no material (0, or white). This means that intermediate (grey) values of the artificial density function should be penalized to promote a black-and-white design. It should be noted that for an optimization case consisting of two materials, such as increasing the effective conductivity in a thermal battery with PCM, 1 is assigned to the highly conductive material (HCM), i.e., aluminum, while 0 is assigned to the PCM, which has a very low thermal conductivity.

The SIMP approach, introduced by Bendsøe [125], is arguably the most popular material interpolation model in the topology optimization community [143] (i.e. it is seven times computationally cheaper than the level-set method [144]). The interpolated thermal conductivity then becomes:

$$k(\rho_\theta) = k_{PCM} + (k_{HCM} - k_{PCM})\,\rho_\theta^p \tag{2.31}$$

In this formulation the density, ρ_θ, is the design variable. It could be interpreted as the normalized density of the HCM as its volume is evaluated from $\int_\Omega \rho_\theta \, d\Omega$. In Equation (2.31), p is the material penalization exponent, which defines the steepness of the penalization. A value of $p > 1$ renders the intermediate densities unfavorable, since the associated thermal conductivity becomes small compared to the cost (volume) of the material. In other words, choosing p greater than 1 makes intermediate densities in the optimal design "uneconomical". Hence, penalization is achieved without the need for an explicit penalization scheme. The interpolation of conductivity alone does not introduce penalization; this effect is achieved only in the presence of a (linear) volume constraint of the form [139]:

$$\int_\Omega \rho(\theta)\, d\Omega \leq V_0, \qquad 0 \leq \rho(\theta) \leq 1 \tag{2.32}$$

where V_0 denotes the maximum prescribed volume of HCM.

It has been shown that if p is sufficiently large, a globally optimal solution of 0–1 type exists, provided that the volume constraint is compatible with such a

design [145]. In practice, to obtain true 0–1 designs, a value of $p \geq 3$ is typically required [137].

2.1.6 Regularization: Filtering and Projection

Topology optimization problems are prone to numerical instabilities, most notably mesh dependence and checkerboard patterns [146]. Mesh dependence occurs when the optimized design changes significantly with the refinement of the computational grid, leading to results that are not reliable. Checkerboard patterns, on the other hand, are non-physical layouts with alternating solid and void elements that artificially enhance performance metrics—such as effective conductivity in our case—but cannot be realized in practice.

The mesh-dependence problem is illustrated with a generic example in Figure 2.2. The top and right boundaries (Γ_c) are in contact with a heat sink, while Γ_h is at a high temperature (see Figure 2.2a). With the objective of minimizing the temperature along Γ_h and a maximum allowable volume fraction of 30%, the topology optimization is performed using three different mesh resolutions. The mesh is refined from Figure 2.2a to d, revealing the evolution of the optimized geometry. As the grid becomes finer, the design develops more branched features, and a gap begins to appear at the base of the trunk (see the bottom-left corner in Figures 2.2c and d). Ideally, mesh refinement should provide a more accurate finite element representation of the same optimal structure and a clearer description of its boundaries, rather than producing a more detailed yet qualitatively different design.

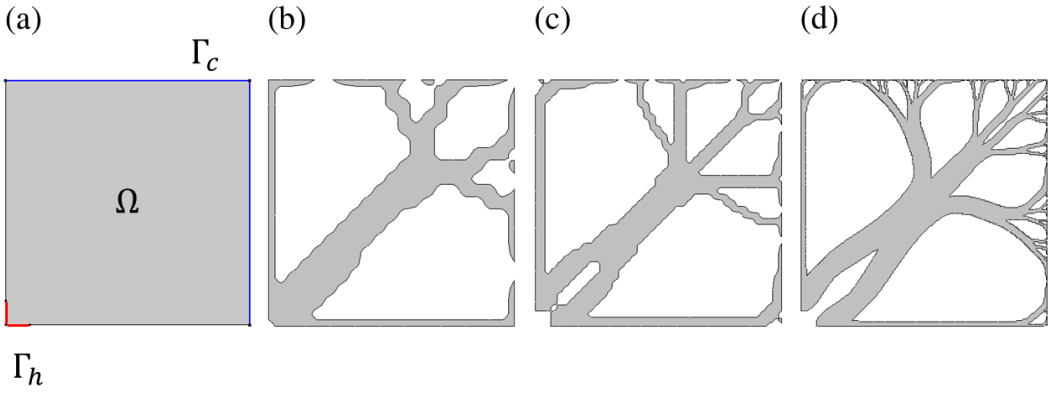


Fig. 2.2 A generic example of mesh dependence with (a) 20×20, (b) 40×40, and (c) 200×200 elements.

The checkerboard problem refers to regions in the "optimal topology" consisting of alternating solid and void elements. These patterns arise from poor numerical modeling of the performance metrics (e.g., stiffness in structural mechanics or effective conductivity in LHTES) [147, 148]. The formation of checkerboards is a typical example of non-convergence in the finite element method. Díaz and Sigmund [147] demonstrated that checkerboard configurations exhibit artificially high stiffness (in structural mechanics) compared to uniformly distributed materials. Building on this, Jog and Haber [148] developed a theoretical framework based on a linearized incremental formulation and proposed a patch test to identify spurious thickness modes arising from non-uniqueness in the discretized system. Together, these studies highlight the importance of selecting stable finite elements and confirm that checkerboard patterns can occur in both the homogenization and SIMP approaches [146].

The same problem shown in Figure 2.2 was studied using a first-order finite element discretization to illustrate the numerical instabilities that result in a checkerboard-like pattern. The corresponding optimized geometry is presented in Figure 2.3.

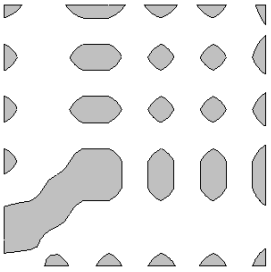


Fig. 2.3 An example of the numerical instability: formation of checkerboard patterns.

A considerable amount of research has focused on preventing checkerboard patterns and mesh dependence. Sigmund and Petersson [146] and Sigmund [149] reviewed numerous studies that introduced different regularization schemes to mitigate numerical instabilities. Checkerboard artifacts can be removed through smoothing techniques or suppressed by employing higher-order finite elements [147, 148], nonconforming finite elements [150], or by introducing additional constraints [151]. A common approach to mitigating mesh dependence is to restrict the design space so that a solution exists for the original continuum problem. For instance, Ambrosio and Buttazzo [152] proposed, and Haber et al. [153] first implemented numerically, a restriction based on limiting the total perimeter of the structure. Although this global

constraint leads to mesh-independent solutions, it does not eliminate local thinning. Alternatively, the design space can be restricted by imposing a minimum length scale on structural members in the final topology. This ensures both mesh-independent and checkerboard-free solutions, as local features smaller than the prescribed length scale are automatically excluded. In density-based topology optimization, restriction methods are essential for ensuring mesh independence and obtaining manufacturable designs. Restriction methods in density-based topology optimization can generally be classified into three main categories [149]:

1. Filtering methods, including sensitivity filters [146] and density filters [154];
2. Constraint-based methods such as perimeter control [155], global gradient control [156], local gradient control [157], regularized penalty methods [158], and integral filtering [159];
3. Alternative approaches such as wavelet parameterizations [160], phase-field formulations [132], and level-set methods [129].

Among these, filtering methods in the first category are the most widely adopted, primarily due to their simplicity of implementation and computational efficiency [149].

Filtering: Helmholtz Filter

The filtered value of a design variable at a given cell is computed as a weighted average of the surrounding cells. In this approach, the cell density—and consequently the performance metrics (e.g., stiffness in structural mechanics or effective conductivity in LHTES)—depend on the density distribution within a prescribed neighborhood. Density filtering was first introduced in Ref. [154], and its ability to guarantee the existence of a solution was later established in Ref. [161].

Filtering is implemented through a convolution between the density field and a filter function:

$$\rho_f(\boldsymbol{x}) = (F \times \rho)(\boldsymbol{x}) = \int_{\mathbf{B}_R} F(\boldsymbol{x}-\boldsymbol{y})\rho(\boldsymbol{y})d\boldsymbol{y} \tag{2.33}$$

Here, $\mathbf{B}_R$ denotes a neighborhood defined as a sphere in 3D (or a circle in 2D) centered at $\boldsymbol{x}$ with radius R. The filter function $F(\cdot)$ must be non-negative within the

support domain $\mathbf{B}_R$ and normalized such that its integral equals one:

$$\int_{\mathbf{B}_R} F(\boldsymbol{x}) d\boldsymbol{x} = 1 \tag{2.34}$$

However, instead of employing the explicit convolution integral in Equation (2.33), the density filter may be implicitly defined through the solution of a Helmholtz-type partial differential equation [162]:

$$r_f^2 \nabla^2 \rho_f + \rho_f = \rho. \tag{2.35}$$

The parameter r_f in Equation (2.35) is a length scale that plays a role analogous to R in the original filter. Homogeneous Neumann boundary conditions, $\partial \rho_f / \partial \boldsymbol{n} = 0$, are applied along the boundary of the design domain. The solution of Equation (2.35) can be represented in the form of the averaging integral in Equation (2.33), where the filter function is replaced by the Green's function [163] associated with the boundary value problem defined by Equation (2.35). For $r_f \geq 0$, the Green's function satisfies $G(\cdot) \geq 0$ and decays monotonically with increasing distance $\|\boldsymbol{x} - \zeta\|$. The following properties hold:

$$G(\boldsymbol{x}, \zeta) \geq 0, \qquad x \in \Omega_\zeta, \zeta \in \Omega_\zeta \tag{2.36}$$

$$\int_{\Omega_\zeta} G(\boldsymbol{x}, \zeta) d\zeta = 1. \tag{2.37}$$

Consequently, the filter defined by Equation (2.35) preserves the material volume, meaning that the volume remains unchanged before and after the filtering process. Green's functions decrease monotonically with increasing distance from the source point. As the filter length parameter tends to zero ($r_f \to 0$), the ratio $x/r_f \to \infty$, causing the Green's function to converge to the Dirac delta function, and the filtered field consequently approaches the unfiltered field. The Helmholtz filter not only addresses mesh dependence and the formation of checkerboard patterns but also imposes a minimum length scale on the final optimized geometry [162, 164].

Similar to other standard density filters, the Helmholtz filter does not inherently produce purely black-and-white designs. To achieve crisp black-and-white results, a simple projection step can be applied to the filtered design, as suggested in Refs. [165, 149].

Projection

Filters inherently introduce gray transition regions between solid and void, which can hinder accurate modeling of the underlying physics in certain applications, as the boundaries are not sharply defined [166]. To address this issue, projection techniques have been introduced that map the filtered designs into a binary 0–1 space. Such approaches have been proposed in the literature by Guest et al. [165], Sigmund[149], Xu et al. [167], Kawamoto et al. [164], and Wang et al. [166].

Wang et al. [166] adopted the parametrized projection function proposed by Xu et al. [167], which generalizes the dilation and erosion projections introduced by Guest et al. [165] and Sigmund [149], respectively. The original formulation of the projection was expressed in a piecewise exponential form, but Xu et al. [167] also demonstrated that an equivalent and computationally more efficient expression can be written using a hyperbolic tangent function:

$$\rho = \frac{\tanh\left(\beta\left(\rho_f - \eta_\beta\right)\right) + \tanh\left(\beta\eta_\beta\right)}{\tanh\left(\beta\left(1 - \eta_\beta\right)\right) + \tanh\left(\beta\eta_\beta\right)}. \tag{2.38}$$

This approach maps filtered densities ρ_f into nearly binary values through a smooth projection function, controlled by a threshold parameter η_β and a steepness parameter β. Intermediate values of η_β (e.g., $\eta_\beta \approx 0.5$) provide smoother convergence and enable nearly discrete designs to be achieved even at moderate values of β [167, 164].

To gain a better understanding of the overall procedure, Figure 2.4 demonstrates the algorithm used in the topology optimization problem.

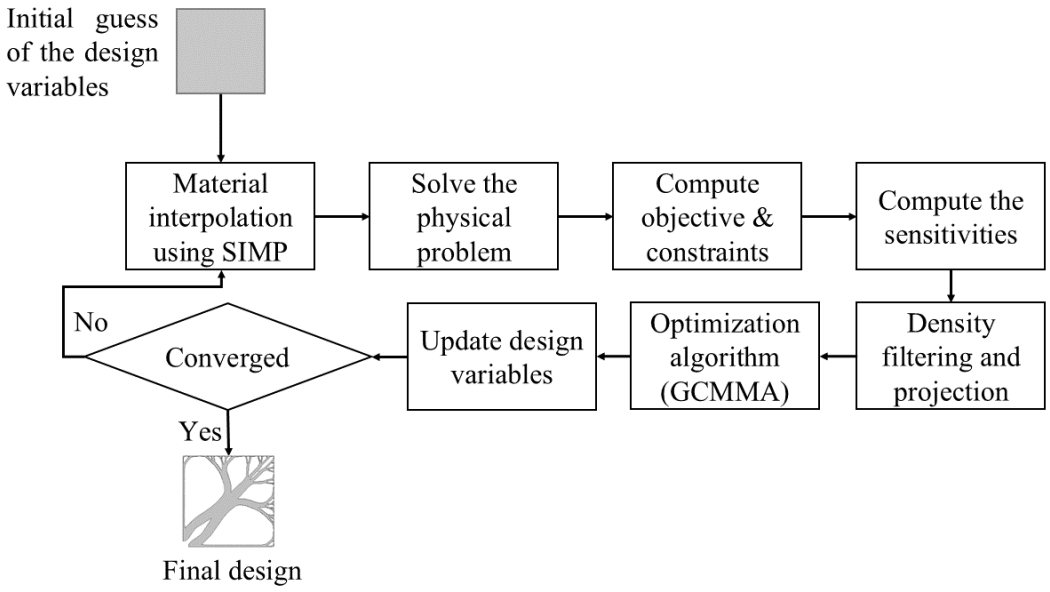


Fig. 2.4 Algorithm for the topology optimization problem.

2.2 Part 2: TPMS Lattices

Porous structures—such as metal foams and packed beds—provide a large surface area within a relatively small volume. In conjugate heat transfer applications, porous materials can significantly enhance heat transfer rates, albeit at the cost of increased pressure drop. In flows through stochastic porous media, stagnant regions or so-called dead zones may form, leading to local flow blockage. Recent advances in additive manufacturing have enabled the fabrication of structured (ordered) porous materials that can achieve heat transfer rates comparable to those of stochastic media, while exhibiting substantially lower pressure losses and minimal flow blockage. Among structured porous media, TPMS lattices have attracted considerable attention due to their promising thermal and mechanical properties, as well as their favorable hydraulic performance in fluid flow applications.

Mathematically, a minimal surface can be represented using level-set equations composed of trigonometric functions in the form of $\phi(X,Y,Z) = 0$ [168]. A TPMS unit cell can be generated from these zero-thickness iso-surfaces using an offset parameter, $\phi(X,Y,Z) = \psi$, which shifts the zero level of the implicit function and therefore controls how much of the unit cell is classified as solid versus void. TPMS

structures are then generated by periodically repeating the unit cell along the three principal directions [169].

Thereby, a TPMS unit cell can be designed using two main approaches. In the first approach, one of the two volumes separated by the minimal surface is designated as the solid domain, while the other represents the void. This is achieved by defining the solid region as the volume where $\phi(x,y,z) > \psi$ or $\phi(x,y,z) < \psi$, forming a solid-TPMS [170]. The second method involves offsetting the minimal surface in both the normal and opposite directions, such that the solid domain is defined by a pair of parallel surfaces satisfying $-\psi \leq \phi(x,y,z) \leq \psi$ [170]. The region enclosed between these two surfaces is considered the solid domain and results in a thickened, shell- or sheet-based lattice derived from the minimal surface. This arrangement is referred to as a sheet-TPMS [171]. Sheet-TPMS lattices have demonstrated enhanced mechanical properties compared to solid-TPMS lattices at the same relative density. In addition, sheet-TPMS structures offer a higher surface-area-to-volume ratio than their solid counterparts when evaluated at an identical unit-cell size [172]. All TPMS lattices investigated in this study belong to the sheet type.

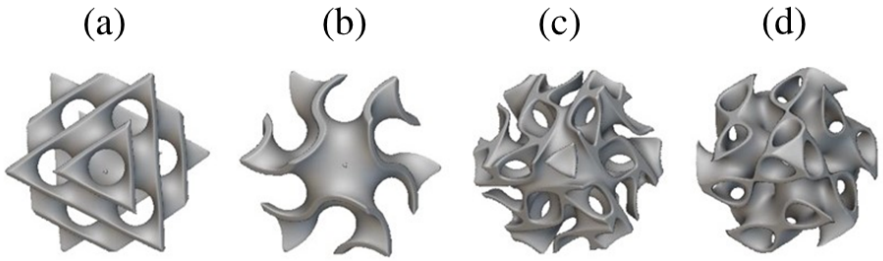


Fig. 2.5 Studied TPMS lattices (a) Diamond (b) Gyroid (c) Lidinoid (d) SplitP.

In this study, four different TPMS structures—namely Diamond, Gyroid, Lidinoid and SplitP (Figure 2.5)—were investigated. The level-set equations for the TPMS lattices under study are presented in Table 2.1 [173]. In this table, $X = 2a\pi x$, $Y = 2b\pi y$, and $Z = 2c\pi z$, where a, b, and c are constants related to the unit cell size in the x, y, and z directions, respectively. For example, for a unit-cell size of 10mm, $a = b = c = 10$ mm.

Table 2.1 Level-set equations of the analysed TPMS structures. Derived from Ref. [174].

Structure name	**Characteristic function**
Diamond	$\sin(X)\cdot\sin(Y)\cdot\sin(Z)+\sin(X)\cdot\cos(Y)\cdot\cos(Z)+\cos(X)\cdot\sin(Y)\cdot\cos(Z)+\cos(X)\cdot\cos(Y)\cdot\sin(Z)=\psi$
Gyroid	$\sin(X)\cdot\cos(Y)+\sin(Y)\cdot\cos(Z)+\sin(Z)\cdot\cos(X)=\psi$
Lidinoid	$\sin(2X)\cdot\cos(Y)\cdot\sin(Z)+\sin(2Y)\cdot\cos(Z)\cdot\sin(X)+\sin(2Z)\cdot\cos(X)\cdot\sin(Y)-\cos(2X)\cdot\cos(2Y)\cdot\cos(2Z)-\cos(2Z)\cdot\cos(2X)+0.3=\psi$
SplitP	$1.1\cdot(\sin(2X)\cdot\sin(Z)\cdot\cos(Y)+\sin(2Y)\cdot\sin(X)\cdot\cos(Z)+\sin(2Z)\cdot\sin(Y)\cdot\cos(X))-0.2\cdot(\cos(2X)\cdot\cos(2Y)+\cos(2Y)\cdot\cos(2Z)+\cos(2Z)\cdot\cos(2X))-0.4\cdot(\cos(2X)+\cos(2Y)+\cos(2Z))=\psi$

Chapter 3

Topology Optimization of a LHTES System

To investigate the potential of topology optimization in a realistic, high-performance context, the approach was applied to a compact LHTES device previously developed and experimentally validated. The device employs a 3D Cartesian aluminum lattice infiltrated with paraffin wax, achieving remarkably high specific power densities while preserving a high PCM volume fraction. Owing to its experimentally proven high performance and manufacturability via additive manufacturing, this system represents a meaningful benchmark for assessing topology optimization beyond proof-of-concept geometries. Despite its strong performance, the reference design still exhibits a key limitation: further improvements through conventional parametric optimization are therefore restricted by the fixed topology and by the trade-off between increased aluminum fraction and consequently reduced latent heat capacity. In this context, topology optimization offers a systematic framework to redistribute the existing conductive material—without increasing its volume—in order to further enhance temperature uniformity and accelerate discharge.

3.1 Physical Model

In a recent study, an LHTES mock-up was developed and fabricated using laser powder bed fusion (L-PBF) with AlSi10Mg aluminum alloy powder and subsequently infiltrated with paraffin wax (RT70HC, Rubitherm) [40]. The design incorporated a

cubic metal lattice within the PCM region to overcome its low thermal conductivity. This lattice promoted a more uniform temperature distribution in the PCM while simultaneously reducing melting and solidification times. In addition, the lattice was designed to serve as a heat exchanger between the HTF and the LHTES system.

The metal structure had a cubic form (80 mm × 80 mm × 80 mm) and incorporated an internal 3D Cartesian lattice composed of repeated hollow cubic elements with 6 mm sides (Figure 3.2a). The HTF flowed through an inner duct (34 mm inner, 46 mm outer side) and across external fins (3 mm thick, 9 mm long) integrated into the device. The entire assembly was enclosed in a wooden casing to guide the HTF over the external fins, and a layer of mineral wool was added to enhance thermal insulation from the environment (see Figure 3.2). The aluminum structure had a mass of approximately 630 g. Current study focuses on applying topology optimization to the described LHTES device.

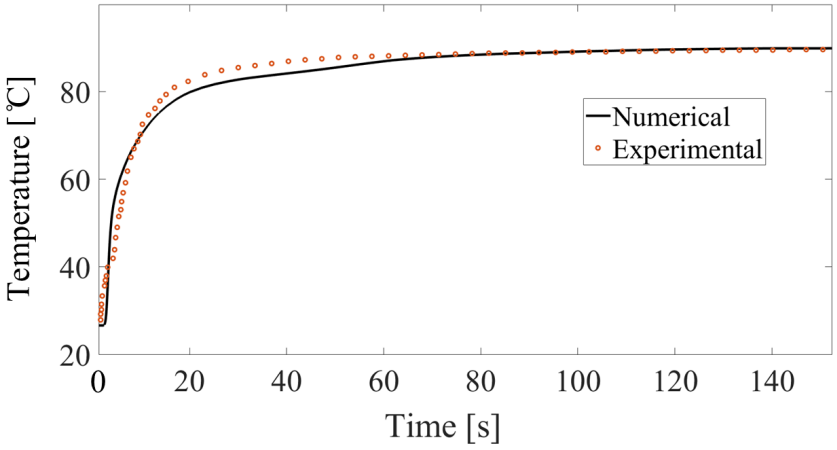


Fig. 3.1 Comparison of the outlet temperature of the HTF with experimental data from Morciano et al. [40].

To validate the numerical model, the simulation results were compared with the experimental data reported by Morciano et al. [40]. To this end, the outlet temperature of the HTF was compared with the experimental data during the charging phase. The melting phase was chosen because it is the critical stage, as it is strongly influenced by convective heat transfer within the phase-change material. However, for the sake of simplification, this study considers only conductive heat transfer and neglects convection in the liquid phase. Figure 3.1 demonstrates very good

agreement between the results, suggesting that this simplification is acceptable under the studied conditions.

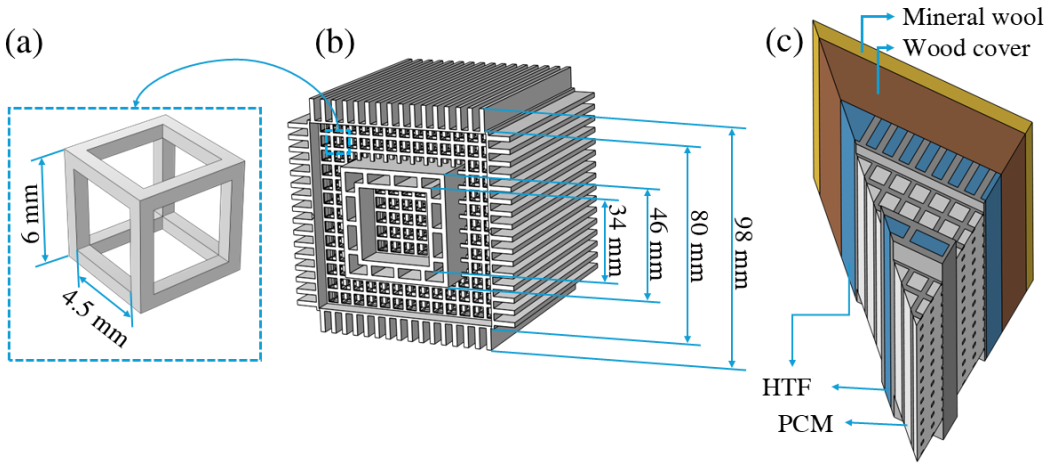


Fig. 3.2 Design of the LHTES mock-up (from Morciano et al. [40]): (a) Unit cell of the Cartesian lattice, (b) 3D CAD model of the device, and (c) 3D computational model illustrating the simulation domains. To reduce computational cost, geometric symmetries were exploited, and only one-eighth of the device was simulated.

The optimization study is primarily focused on the solidification process, as the average heat transfer rate during solidification is significantly lower than during melting [175]. The main objective is therefore to design optimized fins—to replace the internal cubic lattice— that promote even more uniform temperature distribution and, consequently, further reduce the discharging time.

Since topology optimization is computationally expensive, a series of simplifications were applied to the model. For simplicity, and without loss of generality, convective heat losses as well as the wooden casing and mineral wool insulation were neglected. In LHTES systems, solidification is predominantly governed by heat conduction [106]; hence, neglecting natural convection inside the PCM is a reasonable assumption, as also demonstrated in Figure 3.1. A purely conductive heat transfer model was therefore considered. The HTF flow was not explicitly simulated; instead, a Dirichlet boundary condition was applied to the surfaces of the flow channels. During discharging, the channel surfaces were set to a boundary temperature of $T_b = 20\ ^\circ\text{C}$, while the initial temperature of the LHTES was $T_0 = 90\ ^\circ\text{C}$. Conversely, during charging, $T_b = 90\ ^\circ\text{C}$ and $T_0 = 20\ ^\circ\text{C}$.

Topology optimization problems in three dimensions usually require significantly more computational resources than their 2D counterparts. When extending optimization algorithms from 2D to 3D, both the computational time and memory consumption increase rapidly, making efficiency a critical issue. [176]. Therefore, this study is based on a 2D topology optimization.

To enable a credible comparison, the same simplifying assumptions and boundary conditions were applied to the reference model proposed by Morciano et al. [40] (see Figure 3.3e). The boundaries assigned with T_b are highlighted in blue in Figures 3.3d and e.

The topology optimization process starts with an initial 2D design guess (Figure 3.3a), on which the boundary conditions are applied. A volume fraction constraint was imposed during optimization to ensure that the final topology contained the same amounts of HCM and PCM as the reference design.

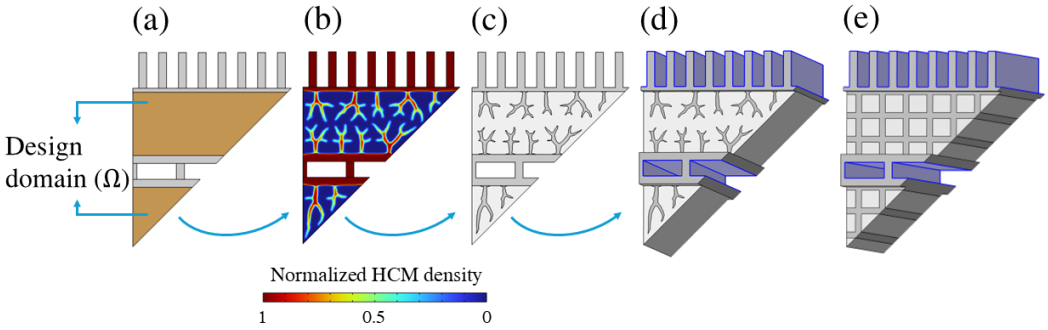


Fig. 3.3 Evolution of the topology optimization design: (a) Initial guess of the design, (b) Filtered density of the material, ρ_f, (c) Final 2D geometry, and (d) Extruded 3D geometry including simulation domains. The simplified reference geometry is shown in (e). To reduce computational cost, geometric symmetries were exploited, and only one-eighth of the device was simulated.

To ensure a fair comparison, the optimized geometry must be evaluated in three dimensions, as the reference LHTES system is based on a 3D Cartesian lattice that cannot be adequately represented in 2D. Therefore, the fin geometry obtained from the 2D topology optimization is extruded to construct the 3D model used to assess the LHTES device (Figure 3.3d). It is worth noting that, in an initial 3D topology optimization study, fins may develop along all three principal directions. Such behavior can lead to designs with improved thermal performance due to the increased fin surface area.

3.2 Topology Optimization Procedure

The topology optimization in this study was performed using the COMSOL Multiphysics (version 6.3) Optimization Module. Given the large number of design variables, a gradient-based optimization algorithm, GCMMA, was employed. As discussed in Chapter 2, to update the design variables during the optimization process, gradient-based methods require the sensitivities of the objective function with respect to the design variables. The adjoint method is particularly well-suited for this purpose, providing an efficient way to compute sensitivities when the number of design variables is large.

The optimization parameters in this study were determined using a continuation scheme and are consistent with values reported in the literature [114]. The parameters employed are: material penalization exponent $p = 3$, projection steepness $\beta = 8$, projection threshold $\eta_\beta = 0.5$, and filter radius $r_f = 0.5\,\text{mm}$.

3.2.1 Objective Function and Constraints

The inherently low thermal conductivity of paraffin wax hinders efficient heat dispersion across the PCM domain, leading to a highly non-uniform temperature distribution. This non-uniformity adversely affects the charging and discharging dynamics, resulting in excessively long full charge and discharge periods. Moreover, in practical applications, several additional issues arise from uneven temperature distributions within the PCM. For instance, achieving a state of full charge or full discharge becomes difficult. During the charging phase, the temperature of the PCM rises sharply in regions close to the heated boundary, while PCM located farther away often remains in the solid state. The overheated PCM near the boundaries is susceptible to thermal degradation [177], and there is a risk that the system may not reach a fully charged state within the allotted charging time. In other words, some PCM regions may not undergo phase change [178] during the charging time window. Similarly, during discharging, a state of full discharge may not be reached. The inherently low specific power of LHTES systems makes them unattractive for practical applications, and PCM degradation further reduces their specific power and operational lifespan.

A more uniform temperature distribution across the PCM domain is indicative of efficient heat dispersion. This not only significantly improves the charging and

discharging rates but also reduces the likelihood of PCM degradation, thereby enhancing system reliability and extending service life. Therefore, with the objective of achieving a more uniform temperature distribution, the topology optimization problem is formulated as shown in Equation 3.1. The topology optimization is conducted in two dimensions, as a full three-dimensional analysis would be significantly more computationally expensive.

$$\begin{aligned} \underset{\rho}{\text{Minimize}} \quad & f(T(\rho),\rho) = \int_{\Omega} (T - \bar{T}_{\Omega})^2 dA \\ \text{Subject to} \quad & R(T(\rho),\rho) = 0 \\ & \int_{\Omega} \rho dA - V_{frac} \int_{\Omega} dA \leq 0 \\ & 0 \leq \rho \leq 1 \end{aligned} \tag{3.1}$$

Here, $\bar{T}_{\Omega}$ denotes the surface-averaged temperature in the design domain, R represents the residual of the discretized governing equations, and $V_{frac} = 0.153$ is the volume fraction of HCM inside the reference LHTES prototype. With this volume fraction, it is ensured that when the optimized fins are extruded to 3D, the resulting LHTES system contains equal amounts of HCM (and PCM) to the reference case. The volume constraint is also crucial to prevent the trivial solution in which the entire design domain Ω is filled with HCM. The design domain is shown in Figure 3.3a.

3.3 Finite Element Model

The conductive heat transfer in the LHTES device is computed in three dimensions using the finite element software COMSOL Multiphysics (version 6.3). To reduce computational cost, the geometric symmetries of the system are exploited, allowing only one-eighth of the full device to be simulated (see Figures 3.3d and e).

The energy equation is solved for both the aluminum and PCM domains:

$$\rho c_p \frac{\partial T}{\partial t} - k\nabla^2 T = 0, \tag{3.2}$$

where ρ is the density, c_p is the specific heat capacity, k is the thermal conductivity, and T is the temperature. The phase change of paraffin wax RT70HC is modeled

using the apparent specific heat capacity method, in which the latent heat is incorporated as a temperature-dependent enhancement of the specific heat. This approach introduces peaks at the phase-change temperatures (67 °C and 70 °C), represented by Gaussian functions whose integrals match the total latent heat. Two possible explanations may account for the appearance of the two peaks in the solidification. First, the sample may contain two distinct populations that solidify at different temperatures. Alternatively, the peaks may arise from two different phase-change mechanisms occurring in a single-component material, namely a solid–solid followed by a liquid–solid phase-change [179].

The apparent specific heat c_p^a was fitted to experimental data provided by the PCM manufacturer (see [40]):

$$\begin{aligned} c_p^a &= c_0 + p_1 G(T, T_1^{pc}, \sigma_1) + p_2 G(T, T_2^{pc}, \sigma_2) \\ G(T, \bar{T}, \sigma) &= \frac{1}{\sigma\sqrt{2\pi}} \exp - \frac{(T-\bar{T})^2}{2\sigma^2}, \end{aligned} \tag{3.3}$$

where c_0, p_1, p_2, σ_1, and σ_2 are material-dependent parameters obtained from the best fit to the experimental data. The characteristic phase-change temperatures are $T_1^{pc} = 67\,^\circ\mathrm{C}$ (340.15 K) and $T_2^{pc} = 70\,^\circ\mathrm{C}$ (343.15 K). G is a Gaussian function of T, centered at $\bar{T}$ with a standard deviation of σ. It should be noted that c_0, the specific heat of the PCM, is assumed constant for both the solid and liquid phases. The fitting curves and their corresponding parameters are shown in Figure 3.4 and Table 3.1, respectively.

Additionally, the density transition from solid ($880\,\mathrm{kg/m^3}$) to liquid ($770\,\mathrm{kg/m^3}$) was modeled using a smooth step function centered around the phase-change temperature, ensuring a continuous variation across the transition range. The thermal conductivity of paraffin wax was assumed to be $0.2\,\mathrm{W/(m\cdot K)}$ for both the solid and liquid phases.

The thermophysical properties of the aluminum alloy AlSi10Mg were considered constant throughout this study, with $c_{p,Al} = 0.92\,\mathrm{kJ/(kg\cdot K)}$, $k_{Al} = 140\,\mathrm{W/(m\cdot K)}$, and $\rho_{Al} = 2400\,\mathrm{kg/m^3}$.

The liquid fraction of the PCM is defined using a piecewise function, which depends on the phase-change temperature and the temperature range of the transition

zone (ΔT_{pc}):

$$\begin{aligned} \varepsilon &= 0 && T \leq T_{pc} - \frac{\Delta T_{pc}}{2} \\ \varepsilon &= \frac{T - \left(T_{pc} - \frac{\Delta T_{pc}}{2}\right)}{\Delta T_{pc}} && T_{pc} - \frac{\Delta T_{pc}}{2} < T < T_{pc} + \frac{\Delta T_{pc}}{2} \\ \varepsilon &= 1 && T_{pc} + \frac{\Delta T_{pc}}{2} \leq T \end{aligned} \tag{3.4}$$

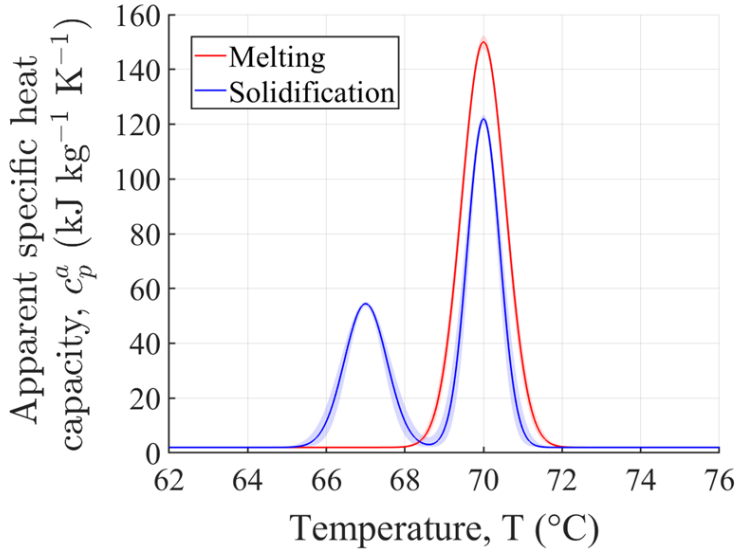


Fig. 3.4 Apparent specific heat capacity of the investigated PCM, with shaded regions indicating the uncertainty in the fitted curves based on the data provided in Table 3.1 (derived from [40]).

The thermal performance of the device was assessed by examining the energy dynamics during the charging and discharging processes, with particular emphasis on the total thermal energy (E) and the latent heat component (L). The total energy accounts for the combined sensible and latent heat stored or released within both the PCM and aluminum domains, whereas the latent heat corresponds solely to the energy associated with the PCM phase change. The total thermal energy is calculated as:

$$E = \int_{V_{PCM}} \int_{T_0}^{T} \rho_{PCM}(T) c_p^a(T) dT\, dV + \int_{V_{Al}} \int_{T_0}^{T} \rho_{Al} c_{p,Al} dT\, dV, \tag{3.5}$$

where T_0 represents the initial temperature at the start of the charging or discharging process. Similarly, the latent heat L stored or released by the PCM during the phase change was calculated as follows:

$$L = \int_{V_{PCM}} \int_{T_0}^{T} \rho_{PCM}(T)(c_p^a(T) - c_0) dT\, dV, \tag{3.6}$$

Table 3.1 Material-dependent coefficients of Equation 3.3 for the apparent specific heat capacity (c_p^a) of paraffin RT70HC during Melting and solidification. Adapted from Ref. [40].

Parameter	**Melting**	**Solidification**
c_0 (kJ/(kg·K))	2	2
p_1 (kJ/(kg·K))	0	71 ± 13
σ_1 $(-)$	–	0.54 ± 0.09
p_2 (kJ/(kg·K))	207.8 ± 14.5	124.5 ± 19.7
σ_2 $(-)$	0.560 ± 0.03	0.414 ± 0.06

3.4 Grid Study

A grid independence study was performed to verify that the spatial discretization did not significantly affect the results of the transient simulations in COMSOL Multiphysics. Because of the time-dependent nature of the problem, it was crucial to ensure that the predicted temporal evolution of the thermal field was consistent across different mesh densities. The fine structure of the optimized fins required small computational elements both within the fins and in the surrounding PCM. Four computational meshes of increasing resolution—labeled Mesh 1 (coarsest) through Mesh 4 (finest)—were tested. All simulations employed identical physics settings, boundary conditions, and solver configurations. An adaptive time-stepping algorithm with a fixed relative tolerance was used to control the temporal discretization error consistently across all meshes. To evaluate the impact of mesh resolution, the temporal evolution of the PCM liquid volume fraction was monitored, with comparisons made at $t = 10\,\mathrm{s}$. The results indicated negligible differences between Mesh 3 and Mesh 4; therefore, Mesh 3 was chosen for subsequent calculations. Details of the

grid study are presented in Table 3.2 and Figure 3.5, while Figure 3.6 shows a cross-sectional view of the selected computational grid.

Table 3.2 Details of the grid study.

	Average Cell Size (m)	**Number of Elements ($\times 10^6$)**	**Liquid Volume Fraction of the PCM (ε)**
Mesh 1	1.489×10^{-8}	2.302	0.4953
Mesh 2	1.117×10^{-8}	3.070	0.4961
Mesh 3	8.421×10^{-9}	4.071	0.4967
Mesh 4	5.202×10^{-9}	6.591	0.4967

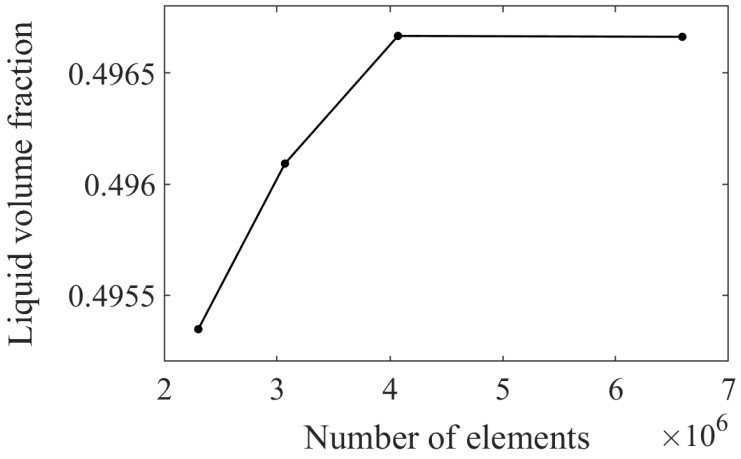


Fig. 3.5 Liquid volume fraction for different grids at t = 10 s.

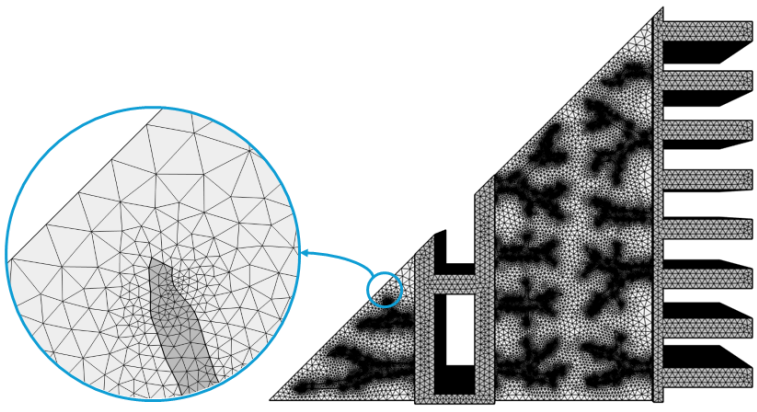


Fig. 3.6 A view of the chosen computational grid.

3.5 Results

The evolution of the optimized geometry is illustrated in Figures 3.3a–c. The fins develop into a branched structure that extends throughout the PCM domain, thereby promoting a more uniform temperature distribution.

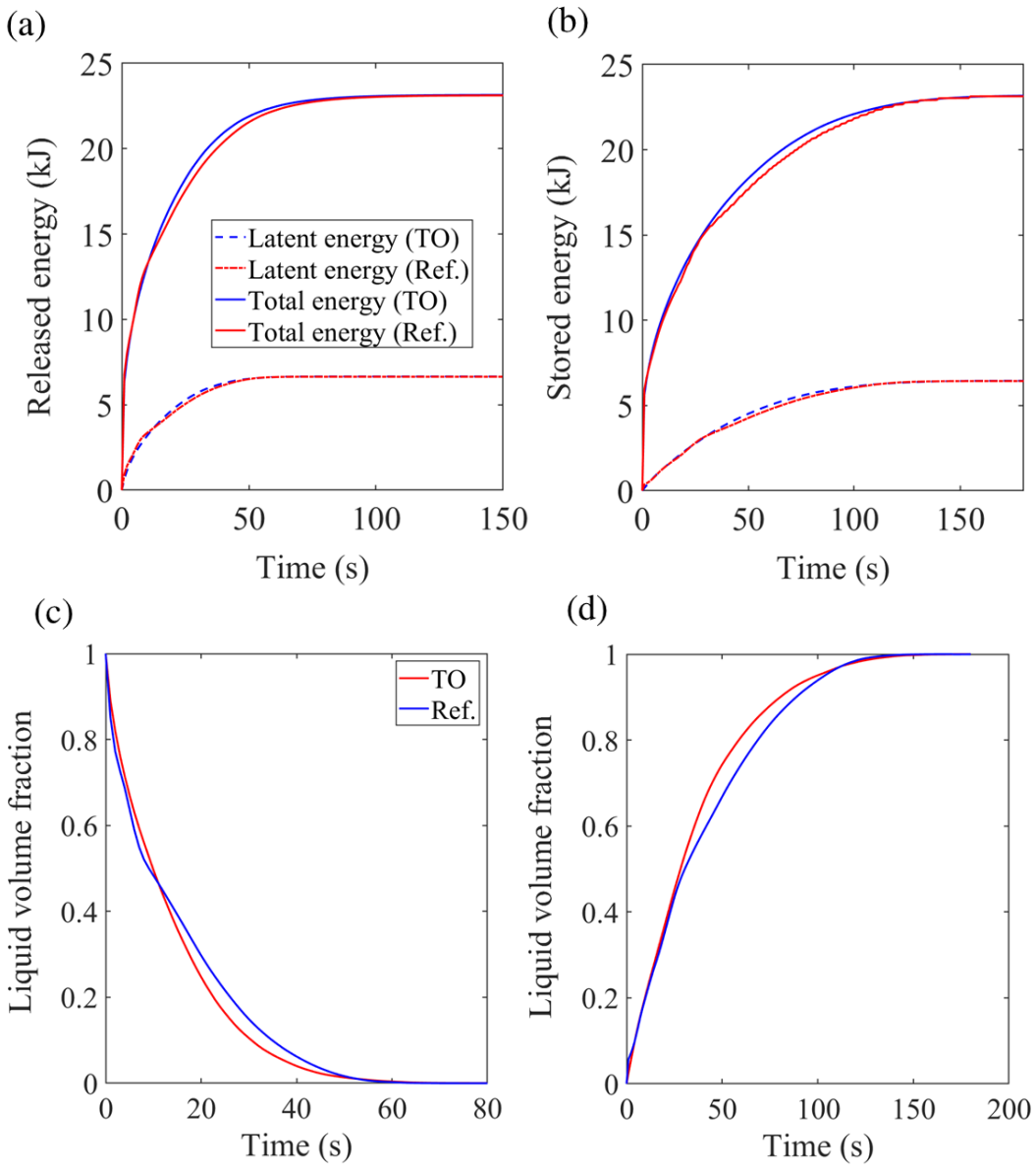


Fig. 3.7 Performance comparison between the simplified reference model and the topology-optimized (TO) model: (a) Thermal energy released, (b) Thermal energy stored and liquid volume fraction of the PCM during (c) discharging and (d) charging.

Simplified models of both the reference and topology-optimized LHTES systems were assessed under identical thermal conditions. Figures 3.7a and b present the released and stored energy for the simplified reference model and the topology-optimized model, respectively. At intermediate stages of both charging and discharging, the optimized model shows superior performance, with greater absorption and release of both total and latent energy.

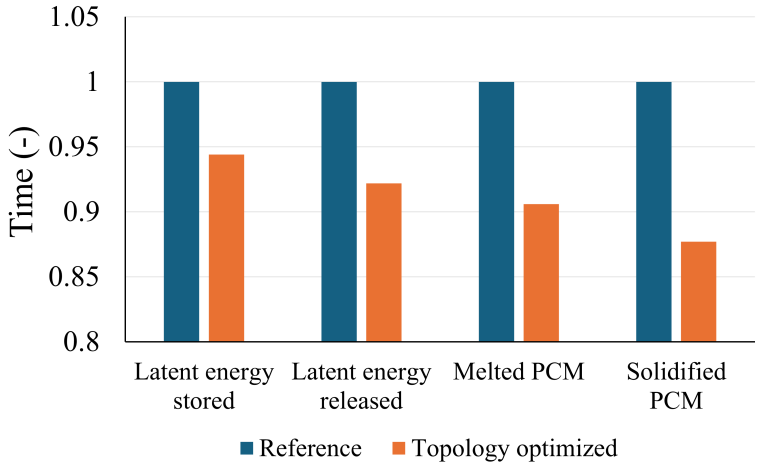


Fig. 3.8 Time to store or release 90% of the latent energy and achieve 90% melting or solidification of the PCM. The vertical axis is normalized by the corresponding t_{90} value of the reference case.

A key metric for evaluating the performance of LHTES devices is the time required to store or release 90% of the available latent heat, denoted as t_{90}. Lower values of t_{90} indicate a faster thermal response. Compared to the reference model, the optimized device achieved improvements of 5.6% and 7.6% in t_{90} for charging and discharging, respectively. An additional noteworthy result is shown in Figure 3.7c, which demonstrates a significant enhancement in PCM solidification during discharging: 90% of the PCM solidifies in 30.6 s in the optimized device, compared to 34.9 s in the reference case, corresponding to a 12.3% improvement. During charging (Figure 3.7d), the improvement in PCM melting is slightly lower, at 9.4%. For clarity, Figure 3.8 summarizes the t_{90} values as well as the times required for 90% of the PCM to melt or solidify during both charging and discharging.

The liquid volume fraction in the mushy zone is calculated using a linear approximation (see Equation 3.4), while the latent heat is modeled with a Gaussian function. This explains the discrepancy between the time required to solidify (or melt) 90% of

the PCM and the time needed to release (or absorb) 90% of the available latent heat in Figure 3.8.

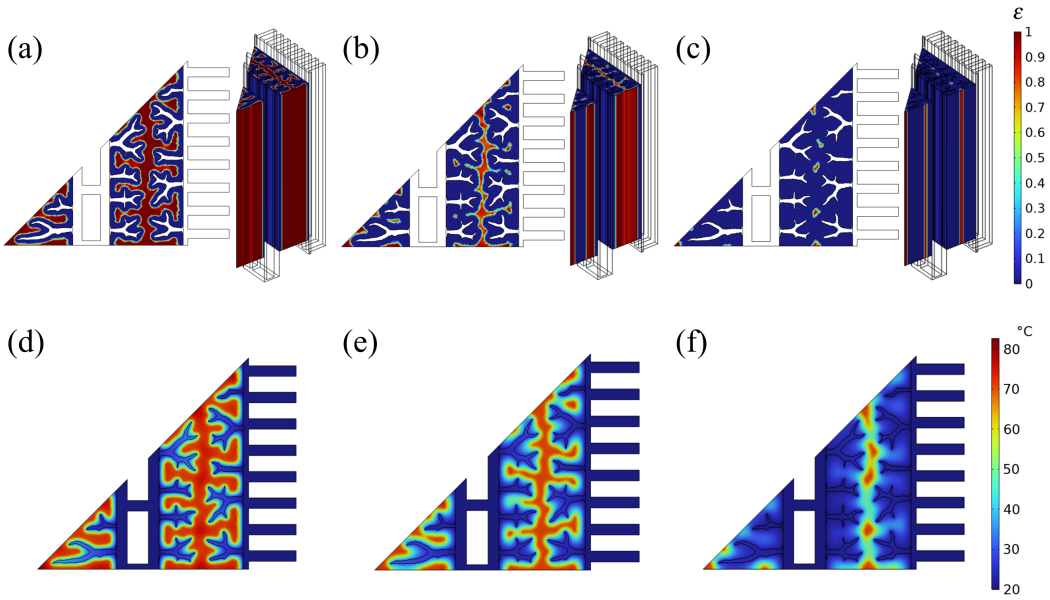


Fig. 3.9 Liquid volume fraction of the PCM during solidification at (a) t = 15 s, (b) t = 30 s, and (c) t = 52 s; Temperature maps during solidification at (d) t = 15 s, (e) t = 30 s, and (f) t = 52 s.

Figures 3.9a–c display the liquid volume fraction (ε) distribution during the discharging process in the optimized LHTES design at $t = 15\,\text{s}$, $t = 30\,\text{s}$, and $t = 52\,\text{s}$, respectively, corresponding to 65%, 90%, and 99% solidification of the PCM. Each panel combines a cross-sectional view (left) with a 3D view (right), providing complementary perspectives of the solidification process. Solidification initiates near the branches and the walls (Figure 3.9a) and then gradually propagates throughout the PCM domain. At $t = 30\,\text{s}$ (Figure 3.9b), some small pockets and a thin strip in the outer PCM region remain in the liquid phase. At this point, around 90% of the PCM has solidified, while several regions remain in the mushy zone. By $t = 52\,\text{s}$ (Figure 3.9c), the PCM has nearly completely solidified (99%), with only a few narrow, isolated liquid channels remaining in regions where heat extraction is least efficient. This behavior highlights the effectiveness of the optimized geometry in accelerating solidification and promoting spatial uniformity by enhancing thermal pathways and minimizing residual liquid pockets.

The temperature distributions at the same time instants ($t = 15,\ 30$ and $52\,\text{s}$) are shown in Figures 3.9d–f, beneath their corresponding liquid fraction distribution

illustrations. It is readily apparent that, at each time instant, the liquid fraction follows the same pattern as the temperature distribution. At $t = 15\,\text{s}$ (Figure 3.9d), temperature gradients indicate efficient heat conduction away from the branches, initiating solidification in nearby regions. By $t = 30\,\text{s}$ (Figure 3.9e), high-temperature zones have largely diminished, particularly near the branches. However, localized hotspots persist in thermally isolated regions farther from the branches, corresponding to residual liquid PCM (see Figure 3.9c). These hotspots are associated with slower cooling and delayed phase change.

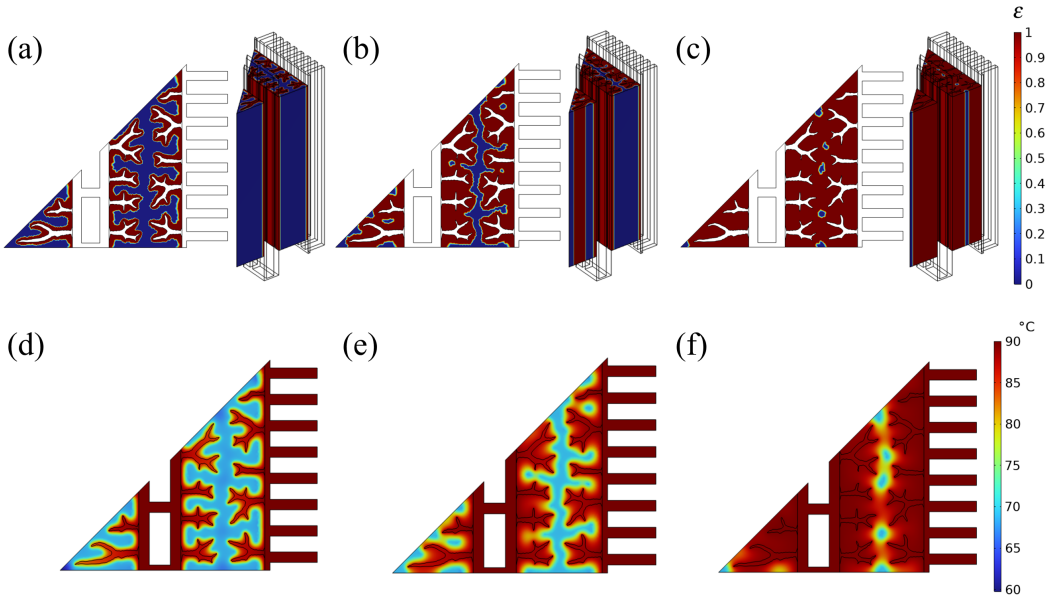


Fig. 3.10 Liquid volume fraction of the PCM during melting at (a) t = 40 s, (b) t = 80 s, and (c) t = 130 s; Temperature maps during solidification at (d) t = 40 s, (e) t = 80 s, and (f) t = 130 s.

Figures 3.10a–c represent the volume fraction (ε) distribution while Figures 3.10d–f demonstrate the temperature distribution during the charging process in the optimized LHTES design at $t = 40\,\text{s}$, $t = 80\,\text{s}$, and $t = 130\,\text{s}$, respectively, corresponding to 65%, 90%, and 99% solidification of the PCM. A very close similarity in is observed to Figure 3.9. For example the same isolated PCM pockets are observed at 99% of melting in Figure 3.10c as in 99% of solidification in Figure 3.9c.

To obtain a better understanding of temperature uniformity and to enable comparison with the reference geometry, the Thermal Uniformity Index (TUI), defined in Equation 3.7, is presented in Figures 3.11a and b for the discharging and charging

processes, respectively. A lower TUI value indicates a more uniform temperature distribution.

$$\begin{aligned} \mathrm{TUI} &= \frac{\int_V |T - \bar{T}|\, dV}{\int_V dV}, \\ \bar{T} &= \frac{\int_V T\, dV}{\int_V dV}. \end{aligned} \tag{3.7}$$

At the beginning of both charging and discharging processes, a pronounced increase in the TUI is observed for both geometries. This behavior is expected, as the imposed thermal boundary conditions generate large initial temperature differences within the PCM domain. As heat transfer progresses, the presence of highly conductive aluminum structures in both configurations promotes temperature homogenization, leading to a rapid decline in the TUI. For most of the transient process, the topology-optimized geometry exhibits lower TUI values than the reference case, indicating improved thermal uniformity. Nevertheless, a brief time interval is observed during which the reference geometry shows a slightly lower TUI. Under the constraint of a fixed aluminum volume fraction, the topology optimization distributes conductive material preferentially along dominant heat transfer pathways rather than uniformly throughout the entire PCM domain. Consequently, the optimized configuration does not include conductive fins within the central strip of the outer PCM region. During intermediate stages of charging or discharging, this region becomes thermally delayed relative to the rest of the domain, remaining warmer during discharge and cooler during charge. While the majority of the PCM volume rapidly approaches the average temperature, this isolated region contributes a local deviation, which temporarily increases the TUI. Once heat diffusion and phase change progress within this region, the local temperature difference diminishes and the contribution of this region to the TUI rapidly decreases. As a result, the optimized design regains its advantage and maintains lower TUI values until the end of the charging or discharging process. The observed transient increase in TUI therefore reflects a localized and temporary effect arising from the volume fraction constraint of HCM, rather than a deterioration of the overall thermal performance of the optimized geometry.

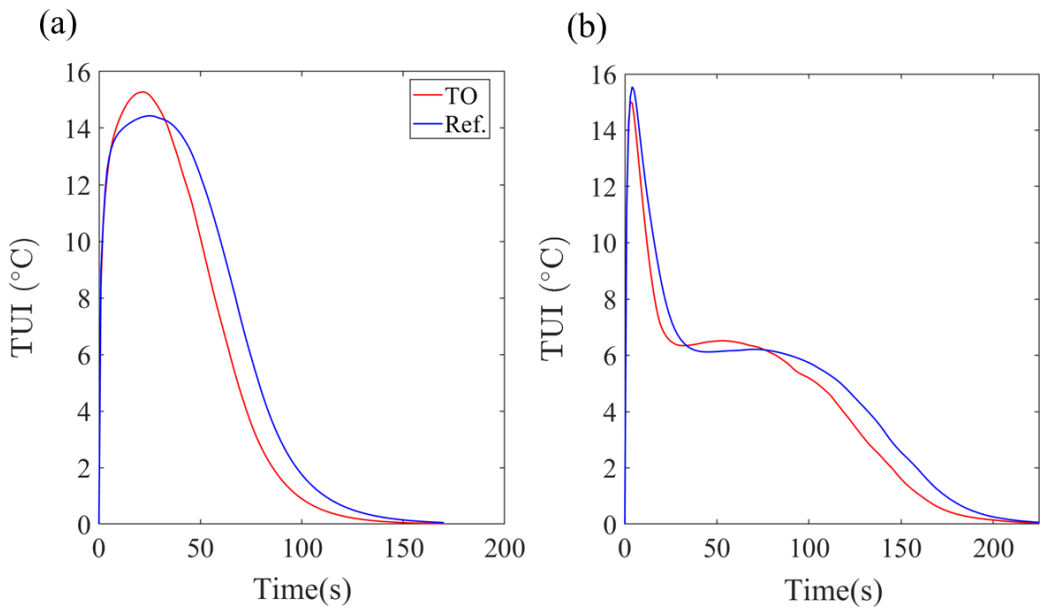


Fig. 3.11 Thermal Uniformity Index for (a) discharging and (b) charging processes.

The total energy (E) and latent energy (L) exchanged during the charging and discharging processes, calculated from Equations (3.5) and (3.6), are shown in Figure 3.12. Nearly 30% of the total stored and released energy is associated with latent heat, underscoring the critical role of phase-change materials in energy storage. The aluminum matrix contributes about 22% through sensible heat, while the PCM itself accounts for nearly 50% of the sensible heat. This demonstrates that, even outside its phase-change interval, the PCM significantly contributes to the system's thermal inertia. Such an energy distribution illustrates the benefit of combining latent and sensible heat storage, enabling substantial energy capacity without the need for excessively high HTF temperatures. Although raising the HTF temperature would increase the sensible heat contribution and total stored energy, it would also amplify thermal losses during storage, potentially reducing the system's overall efficiency. Finally, the nearly symmetric energy shares observed during charging and discharging confirm that the device operates in a balanced and reversible manner.

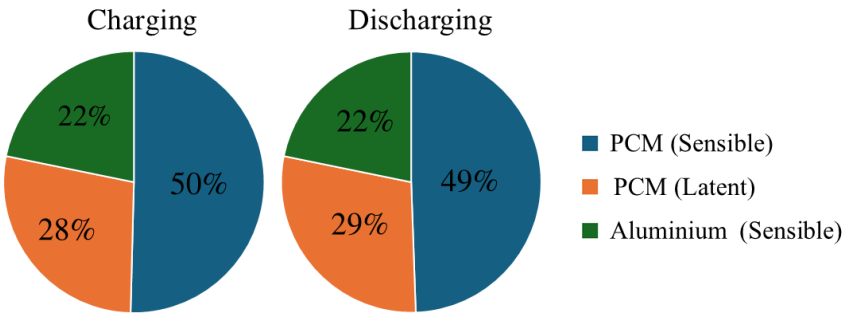


Fig. 3.12 Latent and sensible contributions during charging (left) and discharging (right) in the optimized device.

3.6 Conclusions

This chapter demonstrated the effectiveness of topology optimization in enhancing the thermal performance of LHTES devices even with a simplified 2D optimization approach. The optimized fin geometry, featuring branched structures extending throughout the PCM domain, promotes a more uniform temperature distribution and accelerates phase-change processes. Compared to the reference design, the topology-optimized system exhibited notable improvements in thermal response times, with reductions of 5.6% and 7.6% in the time required to store and release 90% of the latent heat, respectively. The optimized device also achieved faster phase-change dynamics, reaching 90% PCM solidification 12.3% earlier during discharge and 90% PCM melting 9.4% earlier during charge, relative to the reference case.

From the analysis of the TUI, the optimized fin geometry demonstrated an overall improved thermal uniformity compared to the reference case. A brief period of inferior performance was observed, which is attributed to the absence of fins in the central strip of the PCM domain, which leads to localized temperature non-uniformities.

Analysis of energy contributions revealed that latent heat accounts for nearly 30% of the total energy stored and released, highlighting the critical role of the PCM in thermal energy storage. Sensible heat stored in the aluminum matrix contributes about 22% of the total energy, while the PCM itself stores approximately 50% of the sensible heat outside its phase-change temperature range, demonstrating its significant contribution to the system's thermal inertia. This effective combination

of latent and sensible heat storage mechanisms enhances the energy density and allows the system to store substantial energy at relatively lower HTF temperatures, improving overall efficiency while minimizing thermal losses.

Overall, the topology-optimized LHTES design presents a promising approach to improving the thermal performance and efficiency of PCM-based energy storage systems. It enables faster charge–discharge cycles and more effective thermal management in practical applications. The development of more efficient LHTES devices can significantly promote their deployment in real-world applications, including solar thermal energy storage and industrial heat management, by providing faster thermal response, higher energy density, and more effective integration with renewable energy sources.

Chapter 4

Performance Enhancement in CSP Receivers

The use of structured porous media is an emerging approach to enhance heat removal in CSP applications. TPMS lattices, a type of structured porous media, not only provide a high surface-area-to-volume ratio but also feature smooth flow channels, which help maintain considerably lower pressure drops compared to stochastic porous media.

This chapter is divided into three main sections. The first section presents a numerical investigation of a small segment of a tubular receiver in a PTC equipped with four different TPMS lattices. The second section describes the experimental study conducted on planar receiver mock-ups incorporating two TPMS lattice configurations. Finally, the third section provides a numerical analysis of the planar receivers examined in the second part.

4.1 Line-focus Solar Receivers equipped with TPMS

4.1.1 Introduction

PTCs are among the most advanced and mature solar thermal technologies. They are efficient and lightweight structures with relatively low-cost construction, capable of achieving temperatures above 400°C [180]. Their high efficiency explains their use

in approximately 90% of current CSP commercial plants [181]. The growing demand for clean energy, combined with the widespread adoption of these collectors, has driven increased efforts to further enhance their performance. The rapid development of additive manufacturing technology has facilitated the production of complex structured porous inserts with enhanced performance characteristics. Among these, a class of structures known as TPMS has been gaining popularity due to their promising properties. In theory, a TPMS is defined as a zero-mean curvature surface that repeats periodically in the three principal directions [79]. Unlike conventional porous media, TPMS structures (among which the most common are Diamond, Gyroid, I-WP) feature continuous, non-intersecting surfaces, allowing the HTF to flow through smooth, curved channels without sharp edges. This prevents the formation of dead zones, where the flow is stagnant, and poorly mixed regions [83], while maintaining a low pressure drop [84].

Among the studied TPMS structures, the Diamond and Gyroid lattices have been the subject of numerous investigations, demonstrating superior performance compared to traditional heat removal solutions. However, to date, little attention has been given to the thermohydraulic performance of the Lidinoid and SplitP lattices.

The TPMS lattices were generated using the *nTop* 3D design software [182] and subsequently exported to the commercial CFD package *STAR-CCM+* [183]. These lattices were studied with square unit-cell sizes of 10 mm and 20 mm. Other design parameters in nTop included an average wall thickness of 1 mm and a midsurface offset of 0 mm. The length of the insert was 10 cm in both cases.

Considering the internal diameter of the absorber tube, the larger unit-cell size was selected so that two complete unit cells could fit across its vertical diameter, while five complete unit cells could be arranged in series along the tube. The average wall thickness of 1 mm is small yet sufficient for safe production using conventional additive manufacturing technologies.

Key parameters of the studied lattices—hydraulic diameter, porosity, and wetted surface area—are reported in Table 4.1. For the sake of convenience, in this monograph each lattice is referred to by the first letter of its TPMS structure followed by its unit-cell size; for example, S10 denotes the SplitP lattice with a unit-cell size of 10 mm.

4.1.2 Simulation Setup and Boundary Conditions

The simulations were conducted to investigate the thermohydraulic behavior of the cases under study and to estimate their entropy generation. To reduce computational cost, only a short section of the receiver (10 cm) equipped with different TPMS lattices was considered.

Table 4.1 Hydraulic diameter, porosity, and wetted area of studied TPMS lattices based on the unit cell size.

Structure	**10 mm**			**20 mm**		
	D_h (m)	ε (%)	A_{wet} (m^2)	D_h (m)	ε (%)	A_{wet} (m^2)
Diamond	3.79E-03	76.8	1.64E-01	7.81E-03	88.4	9.18E-02
Gyroid	4.79E-03	80.6	1.37E-01	9.45E-03	90.3	7.75E-02
Lidinoid	2.46E-03	71.3	2.35E-01	4.99E-03	82.6	1.34E-01
SplitP	2.81E-03	73.7	2.13E-01	6.02E-03	87.0	1.17E-01

The material of the absorber tube and the TPMS lattices was assumed to be copper. Pure copper and copper alloys can be fabricated using additive manufacturing techniques [184, 185]. In the present study, the maximum temperature reaches 572 K (see Section 4.1.5), which is well below the softening temperature of copper and many copper alloys. Therefore, it is assumed that the material maintains its mechanical integrity under the operating conditions considered. Although pure copper exhibits a sharp reduction in stress-rupture strength in the temperature range of 200–450°C [186], certain copper alloys can feature softening temperatures as high as 1000°C [187].

The internal diameter of the absorber tube was 5.08 cm with a wall thickness of 1 mm. Details of the geometry of the investigated absorber tube section are provided in Figure 4.1.

Syltherm-800 was employed as HTF, and a non-uniform concentrated heat flux was applied on the external surface of the absorber tube. The inlet temperature of the receiver section equipped with the TPMS insert was assumed to be 400, 450, 500, and 550 K. Syltherm-800 can operate at temperatures up to 400°C (676.15 K) [188],

which is significantly higher than the maximum temperatures encountered in the present study.

It was assumed that the glazing of the receiver experiences radiation heat loss to the ambient at a temperature of 295.6 K. In all cases, a fully developed velocity profile was imposed at the inlet. The boundary conditions are shown in Figure 4.1. The thermophysical properties of Syltherm-800 are assumed to be piecewise linear functions based on the data from Ref. [54] (see Table 4.2).

Table 4.2 Thermophysical properties of Syltherm-800 at different temperatures.

T (K)	k (W/(m·K))	ρ (kg/m^3)	μ (Pa·s)	c_p (J/(kg·K))
400	0.1149	840.3	0.00222	1791
450	0.1055	794.8	0.00133	1876
500	0.0961	747.2	0.00084	1962
550	0.0867	696.2	0.00056	2047
600	0.0773	640.0	0.00039	2133

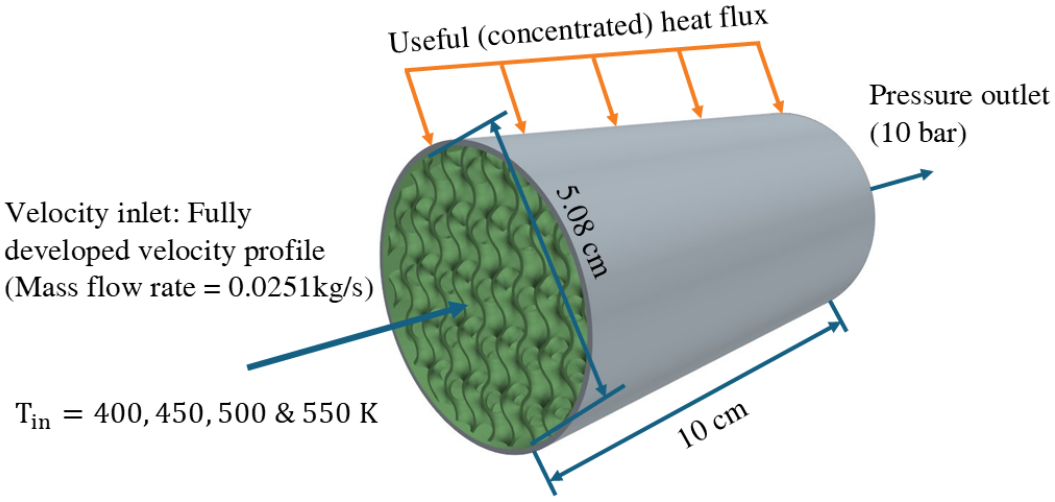


Fig. 4.1 Geometry and boundary conditions of the studied section of solar receivers equipped with a TPMS lattice.

The governing equations (continuity, momentum and energy) are presented in Equations (4.1)–(4.3) in index notation. In this notation, i and j represent the three spatial dimensions, and repeated indices imply summation over the three dimensions

according to the Einstein summation convention. These equations are solved using the finite volume method through a segregated approach.

$$\frac{\partial u_i}{\partial x_i} = 0, \quad i = 1,2,3 \tag{4.1}$$

$$u_j \frac{\partial u_i}{\partial x_j} = -\frac{1}{\rho}\frac{\partial p}{\partial x_i} + \nu \frac{\partial^2 u_i}{\partial x_j \partial x_j}, \quad i,j = 1,2,3 \tag{4.2}$$

$$\rho c_p u_j \frac{\partial T}{\partial x_j} = \frac{\partial}{\partial x_j}\left(k\frac{\partial T}{\partial x_j}\right) + \mu\left(\frac{\partial u_i}{\partial x_j} + \frac{\partial u_j}{\partial x_i}\right)\frac{\partial u_i}{\partial x_j}, \quad i,j = 1,2,3 \tag{4.3}$$

where μ and ν denote the dynamic and kinematic viscosities, respectively.

Since the cross-sectional area and the wetted perimeter of the TPMS lattices may vary along their length, the hydraulic diameter in these structures is defined based on the volume of the fluid, V_{fluid}, and the wetted area, A_{wet}, [189], as given by:

$$D_h = \frac{4V_{\text{fluid}}}{A_{\text{wet}}} = \frac{4\varepsilon V_{\text{total}}}{A_{\text{wet}}} = \frac{\varepsilon \pi D_{\text{internal}}^2 L}{A_{\text{wet}}}, \tag{4.4}$$

where the porosity is defined as the ratio of the void volume to the total volume, $\varepsilon = \frac{V_{\text{fluid}}}{V_{\text{total}}}$, in which the total volume is equal to $V_{\text{total}} = V_{\text{TPMS}} + V_{\text{fluid}}$. Here, A_{wet} denotes the wetted surface area, i.e., the area of the fluid-solid interface, obtained from the CAD model for each geometry.

The Reynolds number of the flow through TPMS inserts can be calculated as

$$\text{Re} = \frac{\rho U_p D_h}{\mu}, \tag{4.5}$$

where the average pore velocity in the insert, U_p, is obtained based on the superficial (or Darcian) velocity, U_s, from

$$U_p = \frac{U_s}{\varepsilon} = \frac{\dot{m}}{\rho \varepsilon A_{\text{receiver}}} = \frac{4\dot{m}}{\rho\, \varepsilon \pi D_{\text{internal}}^2}, \tag{4.6}$$

where $\dot{m}$ is the mass flow rate and A_{receiver} is the internal cross-sectional area of the receiver (without the TPMS lattice).

By substituting Equations (4.6) and (4.4) into Equation (4.5), we obtain a simplified form:

$$\mathrm{Re} = \frac{4\dot{m}L}{\mu A_{\mathrm{wet}}}, \tag{4.7}$$

where A_{wet} is the wetted area of the TPMS structure. The values of A_{wet} are listed in Table 4.1.

In the studied cases, the relatively low Reynolds numbers justify the assumption of a laminar flow regime. The Reynolds number (based on Eq. (4.7)) for the D20 lattice was approximately 195, while it was around 175, 102, and 101 for the G20, S20, and L20 lattices, respectively. For the D10, G10, S10, and L10 lattices, the maximum Reynolds numbers were even lower—about 110, 99, 80, and 58, respectively. According to the literature, Iyer et al. [189] considered Reynolds numbers up to 250 for the Gyroid lattice and around 300 for the SchwarzD lattice to be laminar. Passos [190] also reported that flows with Reynolds numbers below 300 are laminar. It should be mentioned that unlike the case of a long smooth pipe, the transition to turbulent flow in TPMS lattices is gradual, with no drastic changes in the friction factor [191]. Therefore, even if the flow were not completely laminar, using a laminar model would not have introduced significant errors. To verify this, the cases with the highest Reynolds numbers for each TPMS lattice were also simulated using the Lag EB κ-ε Reynolds-averaged Navier–Stokes (RANS) turbulent model, and the results for entropy generation were compared with those from the laminar model. The comparison indicated a negligible difference of 0.4%–1.5% for the studied TPMS lattices. In Section 4.3, it is demonstrated that the Lag EB κ–ε RANS model can accurately predict the thermophysical performance of the TPMS lattices, thereby justifying its selection.

The receiver was assumed to be coated with a cermet selective coating with temperature-dependent emissivity [192]. For the thermal modelling, the solar flux of a typical LS2 PTC was applied as a field function on the external surface of the receiver. The useful heat was then calculated using Eq. (4.8):

$$q_u = q_{\mathrm{abs}} - q_{\mathrm{loss}}, \tag{4.8}$$

where q_{abs} represents the heat rate absorbed by the receiver and can be estimated from Eq. (4.9), while q_{loss} is the total heat loss rate, which was modelled using

Equation (4.12).

$$q_{\text{abs}} = \alpha \times \text{DNI} \times \text{LCR} \times \eta_{\text{Opt}}. \tag{4.9}$$

The optical efficiency (η_{Opt}) was considered to be 80% [57], and the receiver absorptivity (α) was set to 0.95 [193]. The local concentration ratio (LCR) is defined as the ratio of the local heat flux (LHF) to the direct normal irradiance (DNI):

$$\text{LCR} = \frac{\text{LHF}}{\text{DNI}}. \tag{4.10}$$

To model the LCR, the seven-section polynomial curve fit proposed by Kaloudis et al. [192] was employed, as given in Eq. (4.11):

$$\text{LCR} = b_3\,\omega^3 + b_2\,\omega^2 + b_1\,\omega + b_0, \tag{4.11}$$

where ω is the circumferential angle of the receiver . The coefficients of Eq. (4.11) are listed in Table 4.3, and a schematic of the LCR distribution is shown in Fig. 4.2.

Table 4.3 Coefficients of the LCR curve fitting from Kaloudis et al. [192].

Section	ω° range	b_3	b_2	b_1	b_0
1	0–75	0.0	-1.07×10^{-4}	-8.10×10^{-4}	1.11
2	75–104	-2.54×10^{-3}	6.87×10^{-1}	-5.97×10	1.68×10^{3}
3	104–171.2	-6.60×10^{-5}	3.19×10^{-2}	-5.28	3.27×10^{2}
4	171.2–188.8	0.0	1.52×10^{-1}	-5.48×10	4.95×10^{3}
5	188.8–256	5.96×10^{-5}	-3.50×10^{-2}	6.97	-4.40×10^{2}
6	256–285	2.49×10^{-3}	-2.01	5.42×10^{2}	-4.84×10^{4}
7	285–360	0.0	-7.51×10^{5}	5.68×10^{-2}	-9.60

The thermal losses of the receiver (q_{loss}) occur primarily through radiation to the glass cover ($q_{\text{rad,g}}$), while convective losses are neglected due to the presence of the vacuum annulus [194]. Under steady-state conditions, these losses are equal to the heat dissipated from the glass cover to the ambient by radiation. Hence, the overall heat loss is attributed to radiative exchange with the glazing ($q_{\text{rad,g}}$) [195]. Furthermore, radiation absorption by the glass cover is considered negligible [196]. The heat loss used in Equation (4.8) is calculated as:

$$q_{\text{loss}} = q_{\text{rad,g}} = \frac{\sigma\left(T_{\text{abs}}^4 - T_g^4\right)}{\frac{1}{\varepsilon_{\text{abs}}} + \frac{1-\varepsilon_g}{\varepsilon_g}\left(\frac{D_{o,\text{abs}}}{D_{i,g}}\right)} \tag{4.12}$$

Here, $\frac{D_{o,\text{abs}}}{D_{i,g}} = 0.412$, and the glass cover is assumed to be at the ambient temperature ($T_g = 296.6$ K). In Equation (4.12), ε_g denotes the emissivity of the glass cover, assumed to be 0.88 [57], while ε_{abs} represents the emissivity of the absorber tube, defined as [195]:

$$\varepsilon_{\text{abs}} = 0.05599 + 1.039 \times 10^{-4} T_{\text{abs}} + 2.249 \times 10^{-7} T_{\text{abs}}^2 \tag{4.13}$$

The sky temperature (T_{sky}) can be estimated from the ambient temperature (T_{amb}) using the following correlation [197]:

$$T_{\text{sky}} = 0.0552\, T_{\text{amb}}^{1.5} \tag{4.14}$$

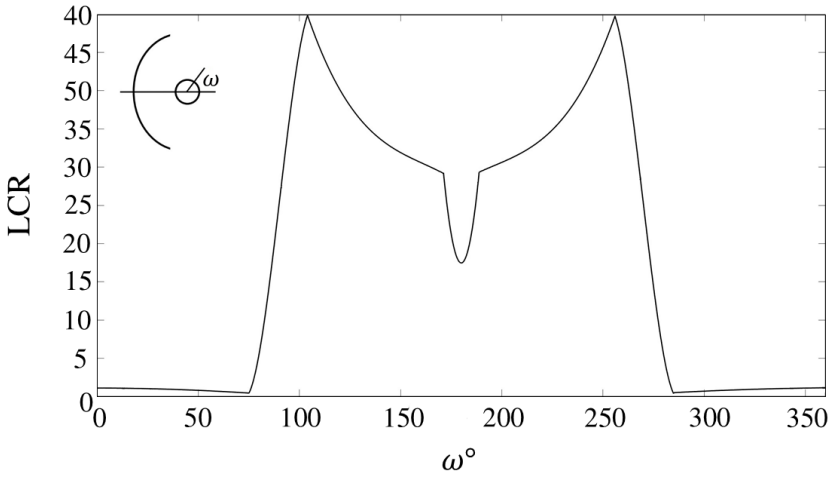


Fig. 4.2 LCR distribution along the LS2 receiver circumferential angles obtained from Equation (4.11).

4.1.3 Performance Assessment Methodology

When enhancing the heat convection coefficient by increasing the heat transfer surface area or promoting turbulence, an inevitable drawback arises: the pressure drop increases. Therefore, a suitable criterion is required to evaluate this trade-off. Unfortunately, conventional performance evaluation criteria such as the Thermal Enhancement Factor (TEF) cannot be applied to absorber tubes with TPMS lattices, since their hydraulic diameters are significantly smaller than that of the smooth

absorber tube (see Table 4.1). This substantial difference in characteristic length strongly affects the Nusselt number and friction factor calculations, rendering TEF an invalid measure of comparison.

To overcome this limitation, the performance of the receivers was instead evaluated in terms of entropy generation. Entropy generation inherently accounts for the combined effects of heat transfer enhancement and fluid friction induced by an augmentation technique, making it a suitable alternative for performance evaluation [198]. Bejan et al. [198] proposed the *augmentation entropy generation number*, $\dot{N}_S$, as a criterion to compare entropy generation in the "augmented" channel with that in a smooth (or "untouched") tube:

$$\dot{N}_S = \frac{\dot{S}_{\text{Augmented}}}{\dot{S}_{\text{Smooth tube}}}. \tag{4.15}$$

An augmentation technique is considered exergetically beneficial if $\dot{N}_S$ be less than unity. Moreover, smaller values of $\dot{N}_S$ indicate a greater exergy payoff associated with the implemented augmentation strategy.

Entropy generation inside the absorber tube is induced by heat transfer and viscous dissipation. For an isotropic Newtonian fluid, the local entropy generation rate is expressed as [199]:

$$\begin{aligned}\dot{S}_{\text{Viscous}} = \frac{\mu}{T}\Bigg[2\left(\left(\frac{\partial u}{\partial x}\right)^2+\left(\frac{\partial v}{\partial y}\right)^2+\left(\frac{\partial w}{\partial z}\right)^2\right)\\ +\left(\frac{\partial u}{\partial y}+\frac{\partial v}{\partial x}\right)^2+\left(\frac{\partial u}{\partial z}+\frac{\partial w}{\partial x}\right)^2+\left(\frac{\partial v}{\partial z}+\frac{\partial w}{\partial y}\right)^2\Bigg]\end{aligned} \tag{4.16}$$

$$\dot{S}_{\text{Heat}} = \frac{k}{T^2}\left[\left(\frac{\partial T}{\partial x}\right)^2+\left(\frac{\partial T}{\partial y}\right)^2+\left(\frac{\partial T}{\partial z}\right)^2\right], \tag{4.17}$$

where (u, v, w) are the velocity components, and k is the thermal conductivity. The overall entropy generation used in Equation (4.15) is obtained by summing Equations (4.16) and (4.17):

$$\dot{S}_{\text{gen}} = \dot{S}_{\text{Viscous}} + \dot{S}_{\text{Heat}}. \tag{4.18}$$

As mentioned in Section 4.1.2, to ensure the validity of the laminar flow assumption, the cases were also studied using a RANS turbulent model. These cases were

analyzed using the approach proposed by Kock and Herwig [200] for the computation of local entropy production in turbulent shear flows. Further details are provided in Appendix A.

The performance of the receivers was also evaluated in terms of thermal and exergetic efficiencies, in addition to $\dot{N}_S$. The thermal efficiency is calculated as

$$\eta_{\text{th}} = \frac{q_{\text{absorbed}}}{q_{\text{incident}}}, \tag{4.19}$$

where the absorbed heat, q_{absorbed}, is calculated from

$$q_{\text{absorbed}} = q_{\text{incident}} - q_{\text{loss}}. \tag{4.20}$$

The exergetic efficiency is defined as

$$\eta_{\text{Ex}} = \frac{Ex_{\text{absorbed}}}{Ex_{\text{incident}}}, \tag{4.21}$$

where the absorbed exergy, Ex_{absorbed}, and the incident exergy from concentrated solar power, Ex_{incident}, are calculated using the following correlations [201]:

$$Ex_{\text{absorbed}} = \dot{m} c_p \left[(T_{\text{outlet}} - T_{\text{inlet}}) - T_{\text{amb}} \ln\left(\frac{T_{\text{outlet}}}{T_{\text{inlet}}}\right) \right], \tag{4.22}$$

$$Ex_{\text{incident}} = q_{\text{incident}} \left[1 + \frac{1}{3}\left(\frac{T_{\text{amb}}}{T_{\text{sun}}}\right)^4 - \frac{4T_{\text{amb}}}{3T_{\text{sun}}} \right]. \tag{4.23}$$

The temperature of the sun, T_{sun}, was assigned a value of 5762 K.

4.1.4 Assessment of the Numerical Uncertainty

To assess the dependence of the results on the computational grid and to estimate the uncertainty or error in the simulation results due to mesh discretization, a grid sensitivity analysis was performed. According to the ASME V&V 20–2009 standard [202], numerical uncertainties were determined using a least-squares approach. The discretization error, defined as the deviation of the computed variable from the exact (extrapolated) value, is assumed to be related to the average cell size Δh by a

power law, as shown in Equation (4.24):

$$\Omega_i - \Omega_\infty \approx \gamma(\Delta h_i)^\zeta, \tag{4.24}$$

where the average cell size Δh is calculated as the cubic root of the ratio between the volume of the domain and the number of computational cells in the i-th mesh. By minimizing the least-squares function given in Equation (4.25), the extrapolated value Ω_∞, the computed order of convergence ζ, and the coefficient γ can be determined:

$$L(\Omega_\infty, \gamma, \zeta) = \sqrt{\sum_{i=1}^{4} \left[\Omega_i - \left(\Omega_\infty + \gamma(\Delta h_i)^\zeta\right)\right]^2}. \tag{4.25}$$

After determining the computed order of convergence, the grid convergence index (GCI) and the numerical uncertainty u_{num} can be obtained from Equations (4.26) and (4.27), respectively:

$$\text{GCI} = \frac{1.25\,\text{er}_{\text{rel}}^{21}}{r_{21}^{\zeta} - 1}, \tag{4.26}$$

$$u_{\text{num}} = \frac{\text{GCI}}{1.15}. \tag{4.27}$$

In Equation (4.26), $\text{er}_{\text{rel}}^{21}$ represents the relative error between the values computed with the finest and second-finest meshes, while r_{21}^{ζ} denotes the ratio of the computational cell counts between these two meshes. The coefficient of 1.15 is recommended by the *ASME V&V 20–2009* standard [202]. The error bars reported in the figures in Section 4.1.5 are based on these calculations.

To assess the accuracy of the results with respect to discretization error, four different grids were generated. Entropy generation was compared across these meshes, ranging from coarse to fine, until an asymptotic value was reached. Polyhedral cells were employed, and although the simulations were conducted using the laminar model, prism layers were included in the near-wall region to better capture temperature and velocity gradients, which are critical for entropy generation estimation. The comparison of studied grids for D20 are presented in Table 4.4. Figure 4.3 shows a cross-sectional view of the mesh, taken perpendicular to the tube axis at a distance of 6.15 cm from the beginning of the D20 insert.

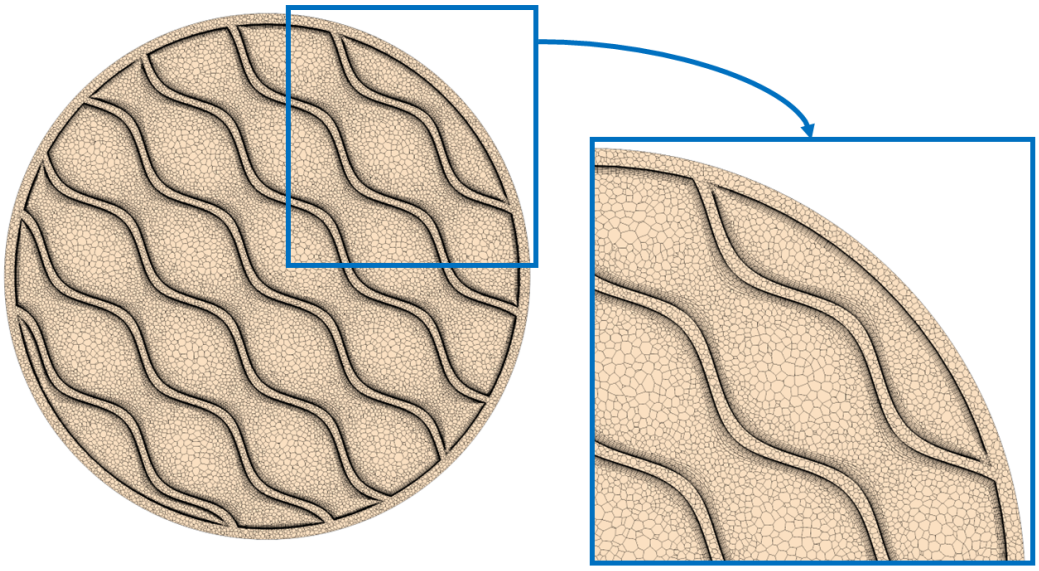


Fig. 4.3 A scene of the grid for D20 in a cross-section perpendicular to the axis of the receiver at 6.15 cm from the beginning of TPMS insert

Table 4.4 Comparison of different grids for D20

Grid Number	**Cell count (in the fluid domain)**	**Average cell size (mm)**	$\dot{S}/\dot{S}_{\text{Reference}}$
1	5.4×10^6	0.3218	0.9402
2	7.5×10^6	0.2880	0.9671
3	1.1×10^7	0.2527	0.9840
Base	1.6×10^7	0.2220	1.0000

Unfortunately, due to the limited availability of experimental data, a comprehensive validation study was not possible. However, the hydraulic performance of the model was compared with the experimental results of Piatti et al. [203]. The comparison, presented in Appendix B, shows that the model can accurately predict the pressure drop at lower Reynolds numbers.

4.1.5 Results

Temperature maps for the cases with an average inlet temperature of 400 K are shown in Figure 4.4 for a vertical cross-section at the outlet of the lattice. For each

lattice type, the top half corresponds to the unit-cell size of 20 mm, while the bottom half denotes the unit-cell size of 10 mm.

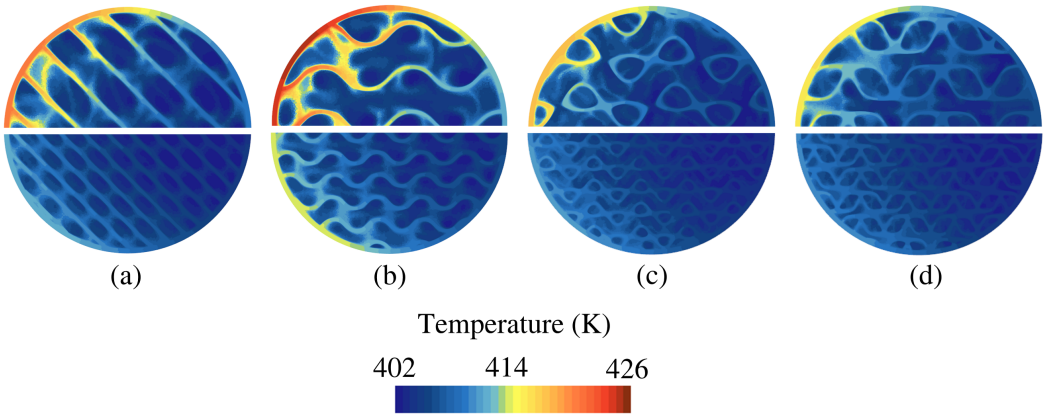


Fig. 4.4 Temperature maps for the average inlet temperature of 400 K, shown in a cross-section at the lattice outlet: (a) Diamond, (b) Gyroid, (c) SplitP, and (d) Lidinoid. For each lattice, the top half corresponds to the unit-cell size of 20 mm, while the bottom half corresponds to the unit-cell size of 10 mm.

The unit-cell size of 10 mm is observed to demonstrate a superior heat removal effect among all the lattices. For all lattices, the 10 mm unit-cell size results in a more uniform temperature distribution throughout both the fluid and solid domains. The receiver with the Gyroid lattice clearly shows higher temperatures in the solid domain. In contrast, the Lidinoid and SplitP lattices exhibit the lowest wall temperatures. Figure 4.5 illustrates the temperature distribution on the external surface of the receivers facing the reflector for the same inlet temperature. In each panel, the top half corresponds to a unit-cell size of 20 mm, while the bottom half corresponds to a unit-cell size of 10 mm. The more uniform and lower temperature distribution associated with the 10 mm unit-cell size is readily apparent. The higher temperatures observed in the Gyroid lattice further indicate its lower heat removal capability. For a clearer comparison of the hotspot temperatures on the external surface of the receivers, Figure 4.6 presents the maximum temperatures for inlet temperatures of 400 K and 550 K. For the smaller unit-cell size, the Lidinoid and SplitP lattices exhibit nearly identical maximum temperatures and similar hotspot areas (see Figures 4.5c and d). However, for the 20 mm unit-cell size, the SplitP lattice shows slightly higher hotspot temperatures. Overall, the Gyroid lattice exhibits the highest maximum temperature among the studied lattices.

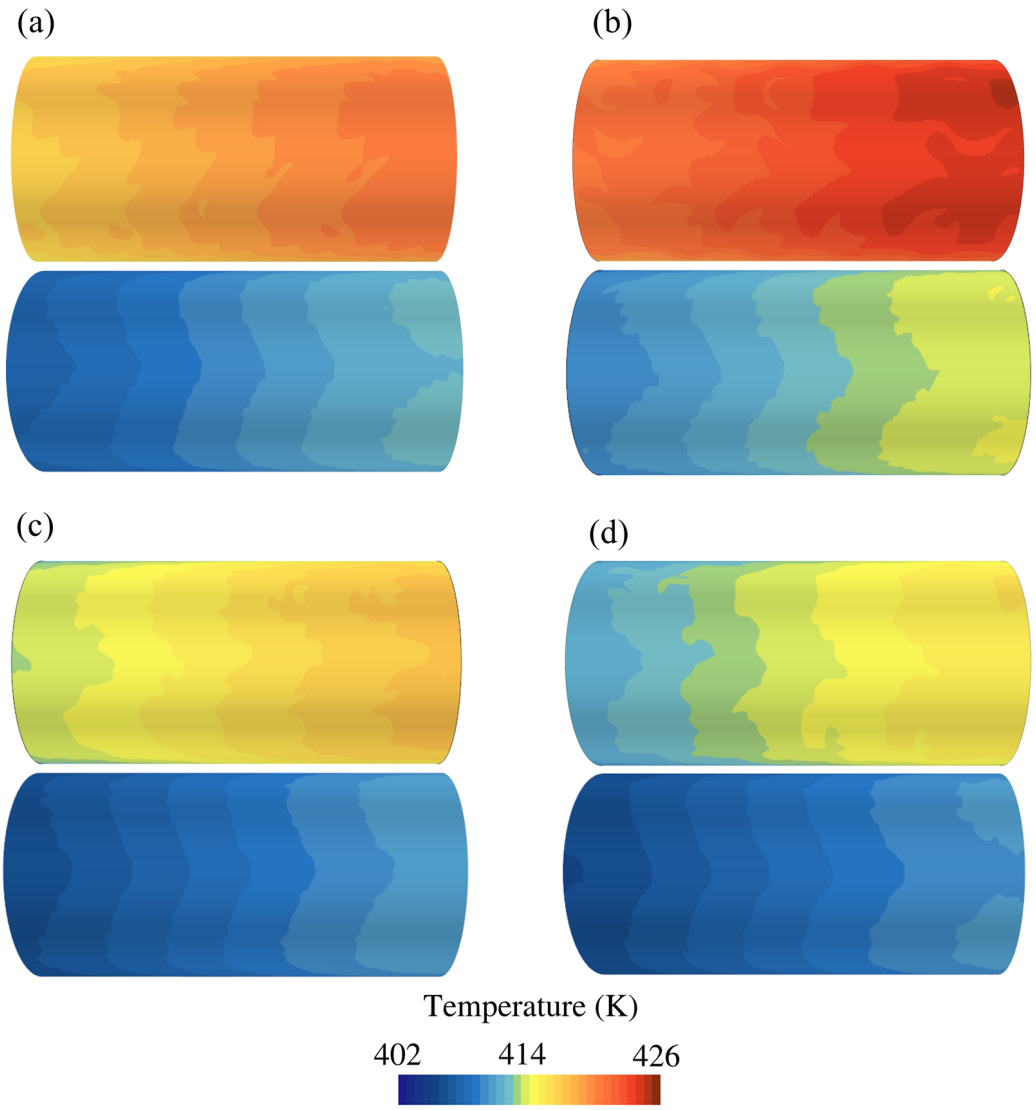


Fig. 4.5 Temperature distribution on the reflector-facing external surface of the receiver segments for an average inlet temperature of 400 K: (a) Diamond, (b) Gyroid, (c) SplitP, and (d) Lidinoid. For each lattice, the top half corresponds to a unit-cell size of 20 mm, while the bottom half corresponds to a unit-cell size of 10 mm.

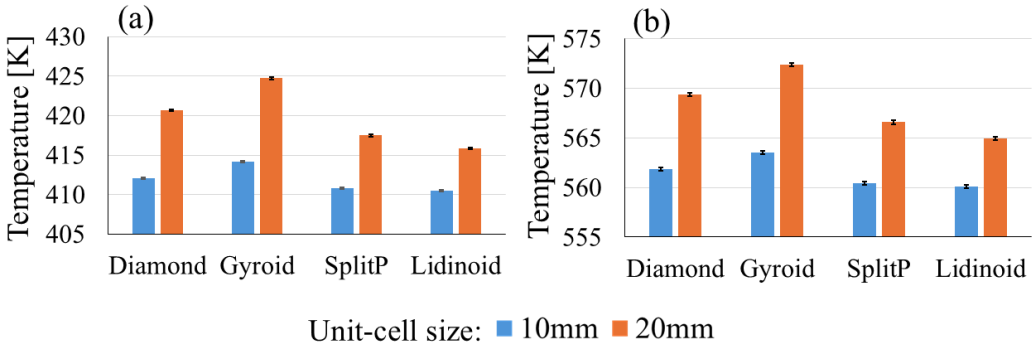


Fig. 4.6 Hotspot temperatures for the inlet temperatures of: (a) 400 K and (b) 550 K.

In Figure 4.7, the performance of the TPMS lattices is compared in terms of $\dot{N}_S$, thermal efficiency, and exergetic efficiency. With higher inlet temperatures, $\dot{N}_S$ decreases to a minimum value and then increases again (see Figures 4.7a and b). For all cases, this minimum occurs at inlet temperatures between 450 K and 500 K. For each TPMS lattice, the unit-cell size of 10 mm yields smaller values of $\dot{N}_S$ compared to the 20 mm case. S10 and L10 exhibit the lowest $\dot{N}_S$ with very similar values, whereas for the unit-cell size of 20 mm, the Lidinoid lattice results in the lowest $\dot{N}_S$. For the 20 mm case, although the viscous entropy generation of the SplitP lattice is slightly lower than that of the Lidinoid lattice, its higher heat-transfer-related entropy generation—which dominates in this case—ultimately leads to a higher $\dot{N}_S$. On the other hand, the Gyroid lattice yields the highest $\dot{N}_S$ for both unit-cell sizes.

Moreover, for all cases, higher inlet temperatures lead to a decrease in thermal efficiency (see Figures 4.7c and d). This is associated to the reduction in the heat transfer rate as the difference in the surface and HTF temperatures reduces. Despite this, in the worst case scenario, the thermal efficiency of the receivers is nearly 70 %. This indicates the significant heat removal performance of TPMS lattices to efficiently dissipate heat within the solid region even with smaller temperature gradients. Based on Figures 4.7c and d, the SplitP and Lidinoid lattices achieve the highest thermal efficiency, with approximately equal values. As observed in Figures 4.5c and d, the temperature distributions in these lattices are nearly identical for a unit-cell size of 10 mm. Even for the unit-cell size of 20 mm, the difference in heat loss between the two lattices is at most bellow 1%.

In Figures 4.7e and f, the SplitP and Lidinoid lattices exhibit the highest exergetic efficiencies, with almost identical values for the 10 mm unit-cell size, while for the

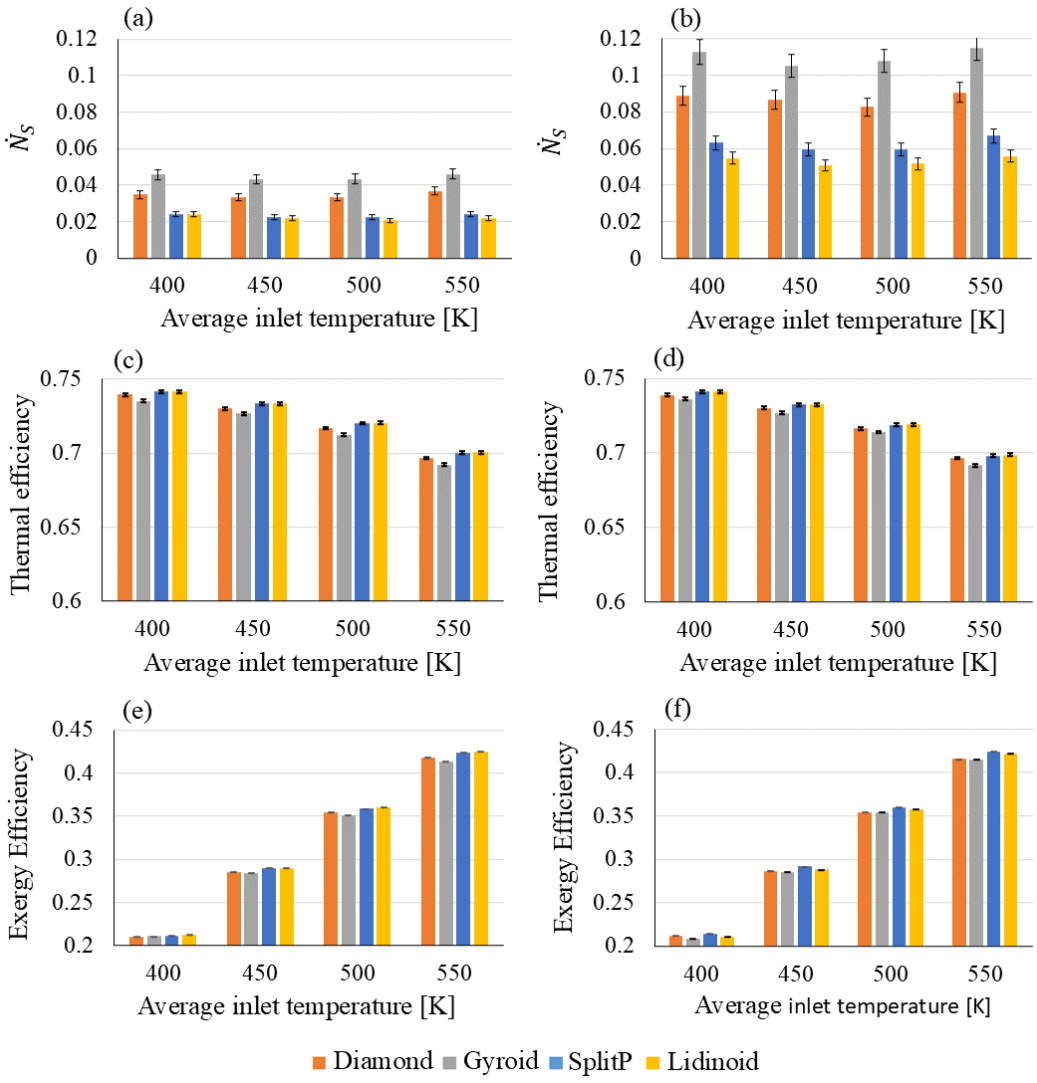


Fig. 4.7 Impact of different average inlet temperatures on the performance of the Diamond, Gyroid, SplitP, and Lidinoid lattices. The column on the left corresponds to a unit-cell size of 10 mm, while the column on the right corresponds to a unit-cell size of 20 mm. (a) and (b) $\dot{N}_S$; (c) and (d) thermal efficiency; (e) and (f) exergy efficiency.

20 mm unit-cell size, the exergetic efficiency of S20 is slightly higher than that of L20 for all inlet temperatures. It should be emphasized that exergetic efficiency accounts for various exergy destruction and loss mechanisms, such as destruction due to the temperature difference between the sun and the receiver, losses due to the optical properties of the receiver and glazing, etc. In contrast, the present study evaluates $\dot{N}_S$ with a focus on viscous dissipation and entropy generation associated with the temperature difference between the receiver containing the TPMS lattice and the HTF. Consequently, the observed behavior of $\dot{N}_S$ in Figure 4.7 does not fully coincide with that of the exergetic efficiency.

Finally, the SplitP lattice exhibits higher exergetic efficiency than the Diamond lattice, which is consistent with the experimental findings represented in Section 4.2, where S10 demonstrated superior exergetic performance compared to D10.

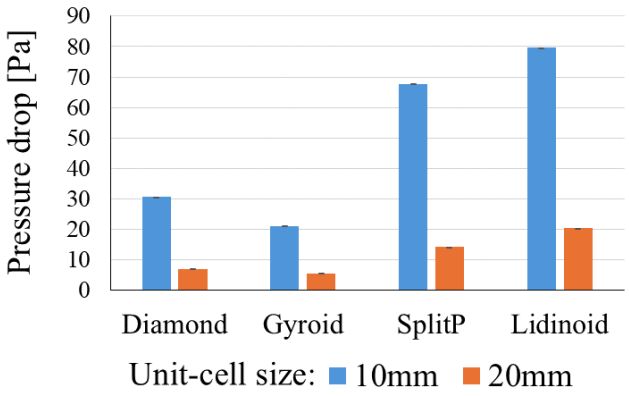


Fig. 4.8 Pressure drop in the studied cases with the inlet temperature of 400 K.

Since a complete receiver has a considerably long length, pumping power is of significant importance. Figure 4.8 demonstrates the hydraulic performance of the studied cases for an inlet temperature of 400 K. It is apparent that, for each lattice, a smaller unit-cell size results in higher pressure drops. The Gyroid lattice exhibits the lowest pressure drop, while the SplitP lattice shows the highest.

Based on the insights obtained in this section, two lattices were selected for further experimental investigation. Since the unit-cell size of 10 mm results in lower values of $\dot{N}_S$, it was chosen for further study. Among the best-performing lattices, SplitP exhibits approximately the same values of $\dot{N}$S, thermal efficiency, and exergetic efficiency, while having a lower pressure drop compared to the Lidinoid lattice. O66 n the other hand, the Diamond lattice is a well-known structure with very good performance and can serve as a benchmark. Consequently, the SplitP and

Diamond lattices with a unit-cell size of 10 mm were selected for further experimental studies.

4.2 Experimental Investigation of Point-focus Receivers with TPMS

To investigate the potential of TPMS lattices for enhancing heat transfer in high-temperature solar receivers, two planar receiver mock-ups—incorporating the selected TPMS lattices—were designed, fabricated, and tested to evaluate their thermal performance under varying mass flow rates and concentrated heat fluxes.

In addition to the numerical studies presented in Section 4, the literature also indicates that the Diamond lattice is a promising candidate for effective heat removal, which further motivated its selection for the first mock-up. The second lattice, SplitP, has only recently attracted attention [173], likely due to its more intricate topology.

The receiver mock-ups based on these lattices were fabricated using additive manufacturing and subsequently tested at the IMDEA Energy Institute using a high-flux solar simulator. Their performance was evaluated and compared based on several parameters, including backside surface temperature rise, outlet temperature, heat absorption, heat loss, and both thermal and exergetic efficiencies.

This study was conducted in collaboration with the MAHTEP research group, and the results were published in Ref. [204].

4.2.1 Samples and Test Campaign

Design and Manufacturing of the Mock-ups

The two planar CSP receivers incorporating the selected TPMS lattices were first designed using nTop [182] and SolidWorks software. They were then fabricated via additive manufacturing using the powder bed fusion method with Stainless Steel AISI 316L.

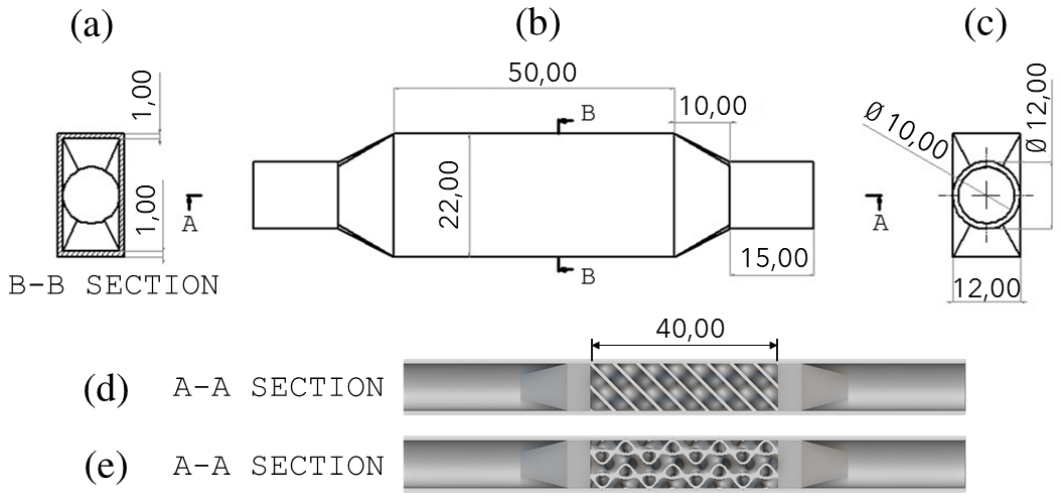


Fig. 4.9 Design plan of the samples (dimensions in millimeters) and 3D CAD longitudinal cross-sectional views of the receiver with (d) Diamond lattice and (e) SplitP lattice (derived from Ref. [204]).

Table 4.5 Values of the porosity, surface-to-volume ratio, and mass of the samples (derived from Ref. [204]).

	Diamond	**SplitP**
Porosity [%]	76.8	73.7
Surface-area-to-volume ratio [mm^{-1}]	1.06	1.43
Mass [g]	56.5	58.4

Both TPMS lattices used in this study were of sheet type, containing two parallel channels within each structure. They were designed with a unit-cell size of 10 mm and an average wall thickness of 1 mm. The design porosity, surface-to-volume ratio, and mass of the samples are reported in Table 4.5. It should be noted that the fabricated samples were not covered with any coating. A schematic of the receivers with dimensions is presented in Figures 4.9a–c, while two longitudinal sections along the mid-plane, illustrating the internal TPMS lattices, are shown in Figures 4.9d and e. Photographs of the manufactured samples, including a detailed view of the lattices, are provided in Figure 4.10. As evident from Figure 4.10, the samples exhibit a relatively high surface roughness, which increases pressure drop but is also expected to enhance heat transfer compared to smooth surfaces. This roughness, inherent to the 3D printing process, is difficult to eliminate.

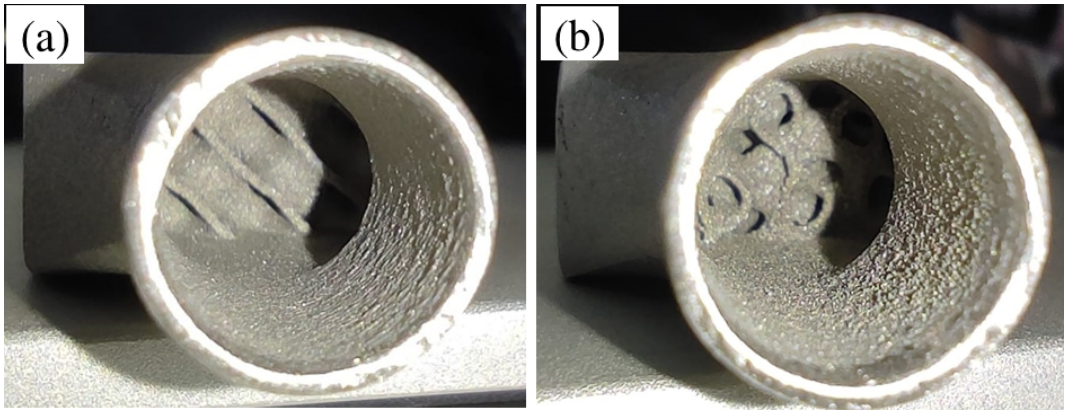


Fig. 4.10 Pictures of the manufactured samples with (a) Diamond lattice and (b) SplitP lattice (derived from Ref. [204]).

Experimental Setup

The two samples were tested in the KIRAN-42 high-flux solar simulator, which is equipped with seven Xenon short-arc lamps (doped tungsten electrodes) mounted with elliptical reflectors in a hexagonal arrangement (Figure 4.11a). The emission spectrum of KIRAN-42 closely resembles that of sunlight, and at full capacity (all seven lamps operating), it delivers a total radiation power of 14 kW with a peak heat flux of 3.6 MW/m^2 at the focal plane [205]. A fully automated XYZ positioning table with an accuracy of 1 mm accommodates the testbed. The testbed is exposed to the Xenon lamps through a large-aperture window equipped with a blind shutter (Figure 4.11b), while another large window, perpendicular to the heat flux direction, provides access from the control room for observation and monitoring. Since the tested heat flux range did not exceed 350 kW/m^2, only the central lamp in the hexagonal arrangement was used during the campaign. To investigate the thermal behavior of the planar solar receivers with TPMS lattices, the open-loop circuit illustrated in Figure 4.12 was employed. Synthetic air (79% N_2, 21% O_2), supplied from a compressed gas cylinder, was regulated to an inlet pressure of approximately 10 bar. Inlet and outlet temperatures, along with absolute pressures, were measured upstream and downstream of the samples. Because the pressure drop across the samples was negligible (below the uncertainty of the pressure gauge), hydraulic data are not reported. To control the ambient temperature of the test room, the heated air was cooled in a secondary loop using a heat exchanger connected to a chiller, before being exhausted. The backside and bottom-side temperatures of the

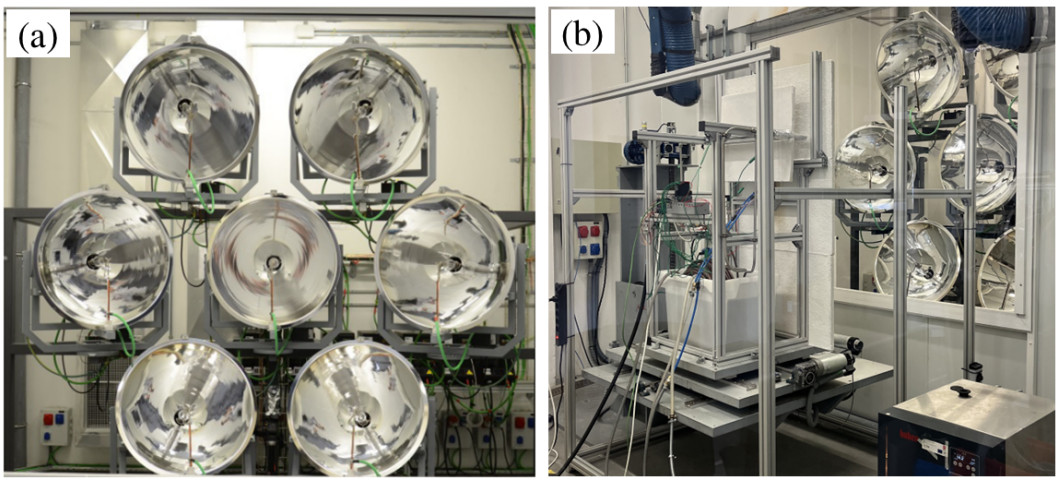


Fig. 4.11 (a) Hexagonal arrangement of Xenon lamps (derived from Ref. [206]) (b) The test table (derived from Ref. [204]).

samples were monitored with four thermocouples. Their locations are shown in Figure 4.12a. A clamp mechanism (Figure 4.12b) ensured good contact between the bottom-side thermocouples and the sample edge. Sensor placement was chosen to capture temperature variations influenced by the fluid path. Two thermocouples were positioned on the back surface: TC_1, located near the fluid inlet where the air heating rate is highest, and TC_3, located near the outlet where the solid–fluid temperature gradient decreases. Two additional thermocouples (TC_2 and TC_4) were installed along the bottom edge.

It is important to note that the temperature comparison between the two samples relies solely on TC_3, as its location was identical on the two mock-ups with high precision. However, the temperature readings from the bottom-side thermocouples (TC_2 and TC_4) could not be used for comparison between the mock-ups because their locations differed from the intended ones. Since they were in good contact with the samples due to the clamp mechanism, their readings—based on their actual locations—were used for validation purposes in Section 4.3.

The instrumentation used in this study includes:

- K-type thermocouples (TC Direct) with an accuracy of ± 0.5 °C and a limit exceeding 1000 °C. Eight sensors were used in total: four on the sample, two at the inlet and outlet, one for the ambient temperature, and one for the exhaust air.

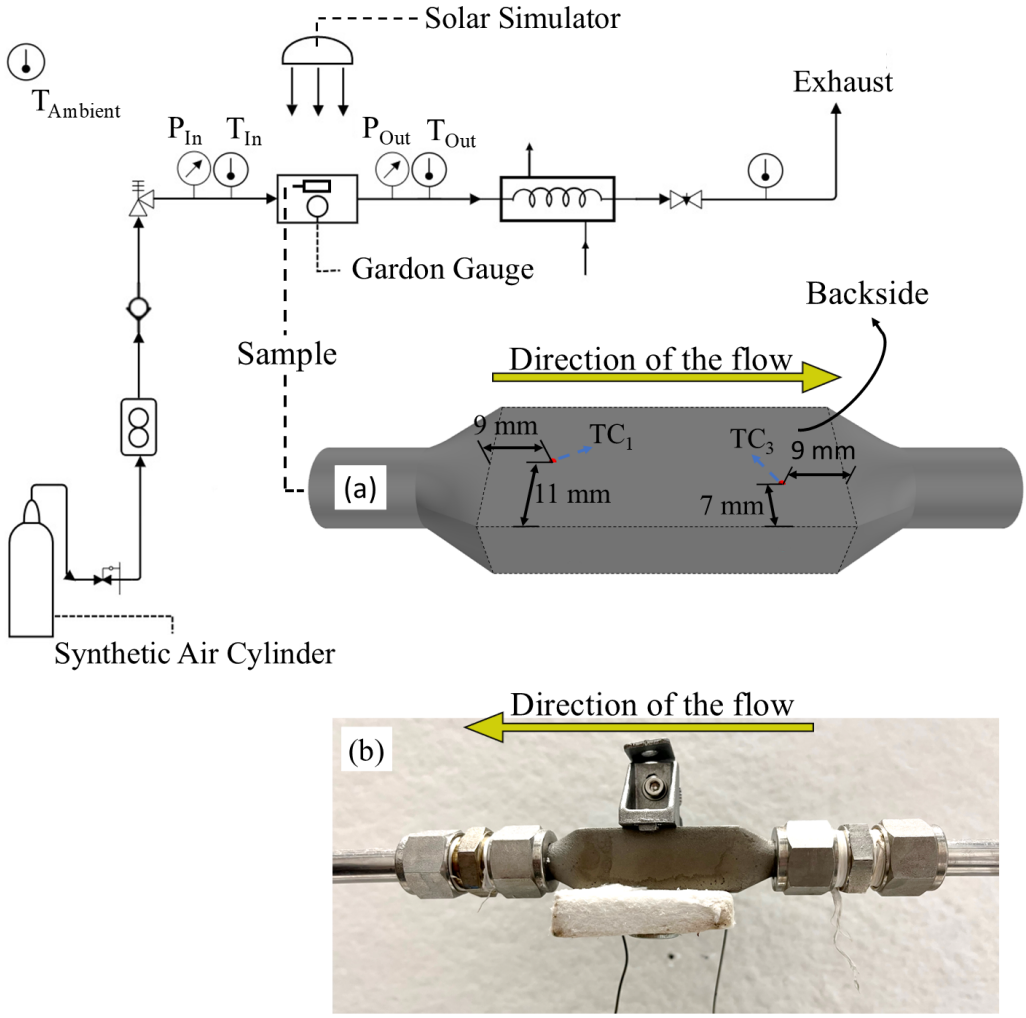


Fig. 4.12 Sketch of the experimental test setup showing (a) the locations of TC_1 and TC_3 on the samples and (b) the front side of the mounted sample (derived from Ref. [204] with modifications).

- An EL-FLOW F–1170K-MBD-44-V mass flow meter (Bronkhorst), with an accuracy of $\pm 0.1\%$ full scale and $\pm 0.5\%$ of reading, with a maximum capacity of 2 g/s at 20 bar and 20 °C.
- A Thermogage circular-foil heat flux transducer (Gardon gauge, TG1000-1 model, Vatell), with a range of 0–160 W/cm^2 and emissivity of 0.95. While the nominal accuracy is $\pm 3\%$, the operator at IMDEA Energy Institute recommended a tolerance of $\pm 10\%$.
- Two pressure transmitters (TC Direct), with a range of 0–16 bar, accuracy of $\pm 0.5\%$ full scale, and output of 0–10 V. Since the pressure drop across the sample was below the measurement uncertainty, these data were not further analyzed.

All the data from the sensors were recorded simultaneously at a frequency of 2 s.

4.2.2 Experimental Procedure

The experimental campaign was conducted from November 7 to November 17, 2023, at the IMDEA Energy Institute in Madrid, with the aim of evaluating the thermal behavior of the two TPMS lattices under varying heat fluxes and mass flow rates. The tests were performed within the framework of the international access program of the SFERA-III project, funded by the European Union. Prior to the experimental work, preliminary simulations were carried out using the commercial CFD software *STAR-CCM+* [183]. These simulations were employed to define the operating conditions of the experiments and to ensure that hotspot temperatures remained below the softening temperature of stainless steel.

The solar simulator's focal plane exhibits a Gaussian heat flux distribution from the Xenon lamp, as illustrated in Figure 4.13. Therefore, to expose the absorbing surface to different heat flux levels, the samples were placed at various vertical positions on the flux map to achieve the corresponding average values. This vertical positions were measured at the first day of the campaign by using a Gardon gauge sensor positioned at the location of the sample on the Lambertian target. After placing the target on the focal plane of the concentrator, the testbed was vertically adjusted to record the coordinates corresponding to the target heat fluxes. This

procedure, recommended by personnel at the IMDEA Energy Institute, is detailed in Ref. [207].

In each session, the mass flow rate was kept constant while different heat fluxes were investigated. This approach was necessary because changing the mass flow rate required access to the test room, which was not possible while the solar simulator was operating. Each session began with adjusting the mass flow rate, after which the valve of the air cylinder was closed to avoid unnecessary air consumption. The Xenon lamp, positioned at the center of the hexagonal arrangement shown in Figure 4.11a, was then switched on and operated for 10 minutes to allow the heat flux to stabilize. To prevent overheating of the lamp, a blower was used throughout the tests. During this phase, precautions were taken to protect the sample: the test table was set vertically so that the concentrated radiation was directed onto the Lambertian target rather than the sample. Once the preliminary adjustments were completed, the cylinder valve was reopened and the table was positioned vertically to achieve the desired heat flux.

In each experiment, the system was allowed to reach a quasi-steady state, and data were recorded for about 10 minutes once this condition was reached, before starting a new test. The tests on the Diamond lattice were completed prior to the installation of the SplitP sample. Test names were assigned using the first letter of the TPMS lattice, followed by the heat flux level and mass flow rate. For example, D100-20 refers to a test performed on the Diamond sample with a heat flux of 100 kW/m^2 and a mass flow rate of 2 g/s. Table 4.6 summarizes all conducted tests, listing the test names along with their corresponding mass flow rates and heat flux levels.

4.2.3 Data Analysis

Theoretically, the heat flux distribution in the solar simulator is rotationally symmetric, reaching its maximum at the center [208]. On the first testing day, following the procedure described in Section 4.2.2, vertical positions on the focal plane corresponding to specific heat flux levels were recorded. Since the heat flux varies across the receiver surface, a correlation was established between these recorded vertical positions and their corresponding heat flux values. The Gaussian heat flux distribution was modeled using ten measured coordinates and their corresponding

Table 4.6 Tests information containing the test names and their corresponding mass flow rate and heat flux level (derived from Ref. [204]).

Diamond			SplitP		
Mass flow rate (g/s)	**Heat flux level (kW/m^2)**	**Test name**	**Mass flow rate (g/s)**	**Heat flux level (kW/m^2)**	**Test name**
0.5	100	D100-05	0.5	100	S100-05
	125	D125-05		125	S125-05
	150	D150-05		150	S150-05
	200	D200-05		200	S200-05
1	100	D100-10	1	100	S100-10
	125	D125-10		125	S125-10
	150	D150-10		150	S150-10
	200	D200-10		200	S200-10
	250	D250-10		250	S250-10
	300	D300-10		300	S300-10
				325	S325-10
1.5	100	D100-15	1.5	100	S100-15
	125	D125-15		125	S125-15
	150	D150-15		150	S150-15
	200	D200-15		200	S200-15
	250	D250-15		250	S250-15
	300	D300-15		300	S300-15
	325	D325-15		325	S325-15
2	100	D100-20	2	100	S100-20
	125	D125-20		125	S125-20
	150	D150-20		150	S150-20
	200	D200-20		200	S200-20
	250	D250-20		250	S250-20
	300	D300-20		300	S300-20
	325	D325-20		325	S325-20

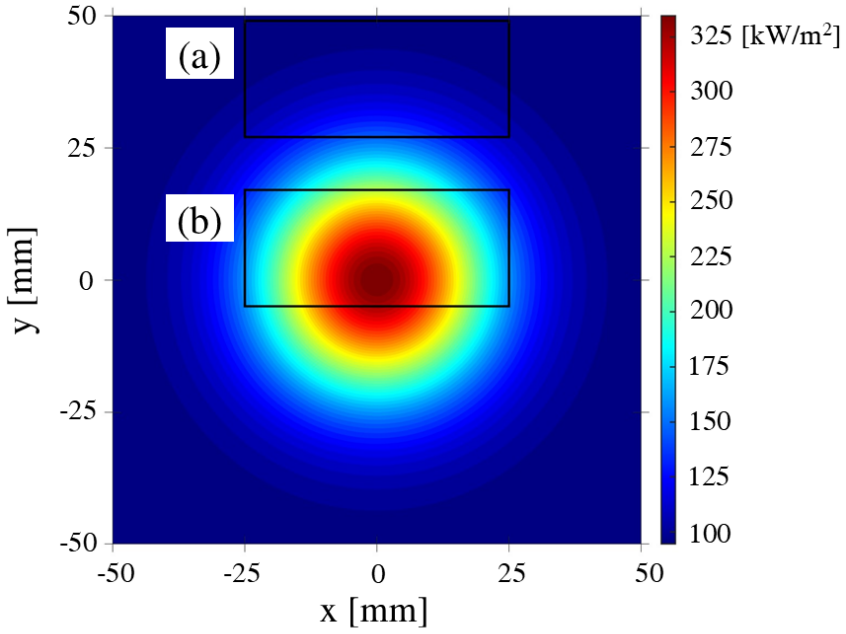


Fig. 4.13 Heat flux distribution based on Equation (4.28), and the location of the sample for a heat flux level of (a) 100 kW/m^2 and (b) 325 kW/m^2 (derived from Ref. [204]).

Table 4.7 Vertical locations of the studied heat flux levels and their corresponding incident heat (derived from Ref. [204]).

Normal heat flux level (kW/m^2)	**Vertical location of the test bed (mm)**	**Incident heat (kW)**
100	38	117.4 ± 11.7
125	33	129.4 ± 12.9
150	28	147.6 ± 14.8
200	20	189.9 ± 19.0
250	14	226.9 ± 22.7
300	9	254.2 ± 25.4
325	6	266.5 ± 26.7

heat flux values as

$$HF(x,y) = A + H\exp\left[-\frac{1}{2}\left(\left(\frac{x}{\sigma_x}\right)^2 + \left(\frac{y}{\sigma_y}\right)^2\right)\right], \tag{4.28}$$

where $A = 94.43$ kW/m^2, $H = 245.08$ kW/m^2, and $\sigma_x = \sigma_y = 15.575$ mm are the standard deviations in the x and y directions, determined by the best fit to the measured values.

Figure 4.13 shows the heat flux distribution predicted by Equation (4.28), highlighting the vertical positions of the sample for heat flux levels of 100 and 300 kW/m^2 in panels (a) and (b), respectively. The vertical positions of the studied heat flux levels and their associated incident heat (calculated using Equation (4.29)) are summarized in Table 4.7. The origin of the coordinate system is defined at the location of the maximum heat flux on the focal plane.

The total incident heat, q_{incident}, is obtained by integrating Equation (4.28) over the receiver surface:

$$q_{\text{incident}} = \iint \left[A + H\exp\left(-\frac{1}{2}\left(\frac{x^2}{\sigma_x^2} + \frac{y^2}{\sigma_y^2}\right)\right)\right] dx\,dy. \tag{4.29}$$

Not all the incident solar energy is absorbed and transferred to the working fluid. The amount of useful heat depends on the optical efficiency of the concentrator, the absorptivity of the receiver, and the heat losses to the ambient through radiation and convection. The useful heat is calculated under quasi-steady state conditions using Equation (4.30).

$$q_{\text{u}} = \dot{m} c_p \left(T_{\text{outlet}} - T_{\text{inlet}}\right) \tag{4.30}$$

The specific heat of synthetic air, c_p, is evaluated at $(T_{inlet} + T_{outlet})/2$. The heat loss is then obtained as the difference between the incident heat, q_{incident}, and the useful heat, q_u:

$$q_{\text{loss}} = q_{\text{incident}} - q_u. \tag{4.31}$$

The thermal efficiency is calculated using Equation (4.19), while the exergetic efficiency is obtained from Equations (4.21)–(4.23). The heat source temperature (Xenon lamp) is assumed to be equal to the temperature of the sun, $T_{\text{sun}} = 5762$ K.

Table 4.8 Experimental error sources and their relative uncertainty (derived from Ref. [204]).

Variable	**Uncertainty**	**Value**
Concentrated flux	$q_{incident}$	$\pm 10\%$
Air flow rate	$W_{\dot{m}}$	$\pm 1.5\%$
Temperature	$W_T, W_{T_{out}}, W_{T_{amb}}, W_{TC_1}, W_{TC_2}, W_{TC_3}, W_{TC_4}$	$\pm 1.5\ ^{\circ}\mathrm{C}$
useful heat	W_{q_u}	$\pm 1.9\%$
Heat loss	$W_{q_{loss}}$	$\pm 22\%$
Thermal efficiency	$W_{\eta_{th}}$	$\pm 10.2\%$
Exergy efficiency	$W_{\eta_{ex}}$	$\pm 11\%$

4.2.4 Analysis of Experimental Uncertainty

Each measuring instrument operates within a specified range and has an associated uncertainty. When calculating parameters derived from measured quantities, it is common practice to treat the instrumentation uncertainty as an independent variable. For example, the dependent function R is related to the independent variables $\omega_1, \omega_2, \omega_3, \ldots, \omega_n$ as:

$$R = R(\omega_1, \omega_2, \omega_3, \ldots, \omega_n). \tag{4.32}$$

According to Holman [209], the uncertainty of a dependent variable R, denoted W_R, is given by

$$W_R = \sqrt{\left(\frac{\partial R}{\partial \omega_1} W_1\right)^2 + \left(\frac{\partial R}{\partial \omega_2} W_2\right)^2 + \cdots + \left(\frac{\partial R}{\partial \omega_n} W_n\right)^2}, \tag{4.33}$$

where $W_1, W_2, \ldots, W_n$ are the uncertainties of the independent variables $\omega_1, \omega_2, \ldots, \omega_n$.

The uncertainties of useful heat, thermal efficiency, and exergetic efficiency are calculated as follows:

$$W_{q_u} = \left[\left(\frac{\partial q_u}{\partial \dot{m}} W_{\dot{m}}\right)^2 + \left(\frac{\partial q_u}{\partial T_{\text{out}}} W_{T_{\text{out}}}\right)^2 + \left(\frac{\partial q_u}{\partial T_{\text{in}}} W_{T_{\text{in}}}\right)^2\right]^{1/2}, \tag{4.34}$$

$$W_{\eta_{\text{th}}} = \left[\left(\frac{\partial \eta_{\text{th}}}{\partial q_{\text{incident}}} W_{q_{\text{incident}}} \right)^2 + \left(\frac{\partial \eta_{\text{th}}}{\partial \dot{m}} W_{\dot{m}} \right)^2 + \left(\frac{\partial \eta_{\text{th}}}{\partial T_{\text{in}}} W_{T_{\text{in}}} \right)^2 + \left(\frac{\partial \eta_{\text{th}}}{\partial T_{\text{out}}} W_{T_{\text{out}}} \right)^2 \right]^{1/2}, \tag{4.35}$$

$$W_{\eta_{\text{ex}}} = \left[\left(\frac{\partial \eta_{\text{ex}}}{\partial Ex_{\text{incident}}} W_{Ex_{\text{incident}}} \right)^2 + \left(\frac{\partial \eta_{\text{ex}}}{\partial \dot{m}} W_{\dot{m}} \right)^2 + \left(\frac{\partial \eta_{\text{ex}}}{\partial T_{\text{in}}} W_{T_{\text{in}}} \right)^2 + \left(\frac{\partial \eta_{\text{ex}}}{\partial T_{\text{out}}} W_{T_{\text{out}}} \right)^2 + \left(\frac{\partial \eta_{\text{ex}}}{\partial T_{\text{amb}}} W_{T_{\text{amb}}} \right)^2 \right]^{1/2}, \tag{4.36}$$

$$W_{Ex_{\text{incident}}} = \left[\left(\frac{\partial Ex_{\text{incident}}}{\partial q_{\text{incident}}} W_{q_{\text{incident}}} \right)^2 + \left(\frac{\partial Ex_{\text{incident}}}{\partial T_{\text{amb}}} W_{T_{\text{amb}}} \right)^2 \right]^{1/2}. \tag{4.37}$$

All temperatures in these expressions were offset to their initial values; therefore, the difference between T_{in} and T_{out} before applying the heat flux was excluded from the calculations. Details of the experimental errors are provided in Table 4.8.

4.2.5 Results and Discussion

During postprocessing, the uncertainty associated with each independent variable was determined by summing the standard deviation of the extracted results with the uncertainty of the corresponding measurement instrument.

Table 4.9 presents the Reynolds numbers corresponding to each sample across the range of mass flow rates studied. The Reynolds number was calculated as described in Section 4.1.2. A review of the literature indicates that only a limited number of studies have addressed the transition to turbulent flow, highlighting the need for further investigation. However, as mentioned in Section 4.2, Iyer et al. [189] examined laminar flow through TPMS structures, considering Reynolds numbers up to approximately 300 as remaining within the laminar regime. Therefore for a mass flow rate of 0.5 g/s, the Reynolds number appears to lies within the transitional regime, whereas at 1 g/s, the flow can reasonably be considered fully turbulent.

Table 4.9 Reynolds number of the tests (derived from Ref. [204] with modification).

Mass flow rate (g/s)	Reynolds number	
	SplitP lattice	Diamond lattice
0.5	430	530
1	860	1000
1.5	1300	1560
2	1700	2100

Temperature Profile

An illustration of the measured results, including the transient period, for a test session with a mass flow rate of 0.5 g/s for the sample featuring the SplitP lattice is provided in Figure 4.14. It is worth noting that the sample with the Diamond lattice exhibits a similar behavior to that of the SplitP lattice; therefore, it is not shown in Figure 4.14. The quasi-steady-state results were recorded for approximately 10 min before proceeding to the next heat flux level. To mitigate potential issues arising from imperfect thermocouple calibration, each signal was offset to its initial value, ensuring a starting measurement of zero for each parameter. Since the ambient temperature remained nearly constant (in the range of 19–22 °C), it is not shown in Figure 4.14; however, its value was recorded for each test using the same offset method. Figure 4.14 also illustrates the transient cooling phase, characterized by a rapid spike in temperature readings. The time required for the temperature measured by TC_3 to decrease from 130 °C to 98% of the ambient temperature was 14% longer for the Diamond sample. This indicates a faster transient response in the SplitP sample, likely due to its higher effective thermal diffusivity. According to simple dimensional analysis of the transient heat diffusion equation, the transient timescale scales inversely with thermal diffusivity. While an exact calculation of the thermal diffusivity would require additional information about the mean temperature of the samples, assuming a higher effective thermal diffusivity for the SplitP sample is reasonable, given its smaller porosity and higher mass compared to the Diamond sample (see Table 4.5). In their insightful investigation of the thermal conductivity of TPMS lattice structures, Catchpole-Smith et al. [210] concluded that the thermal conductivity is primarily determined by the solid volume fraction, defined as the ratio of solid material volume to void volume ($V_{\text{Solid}}/V_{\text{Fluid}}$). In other words, the

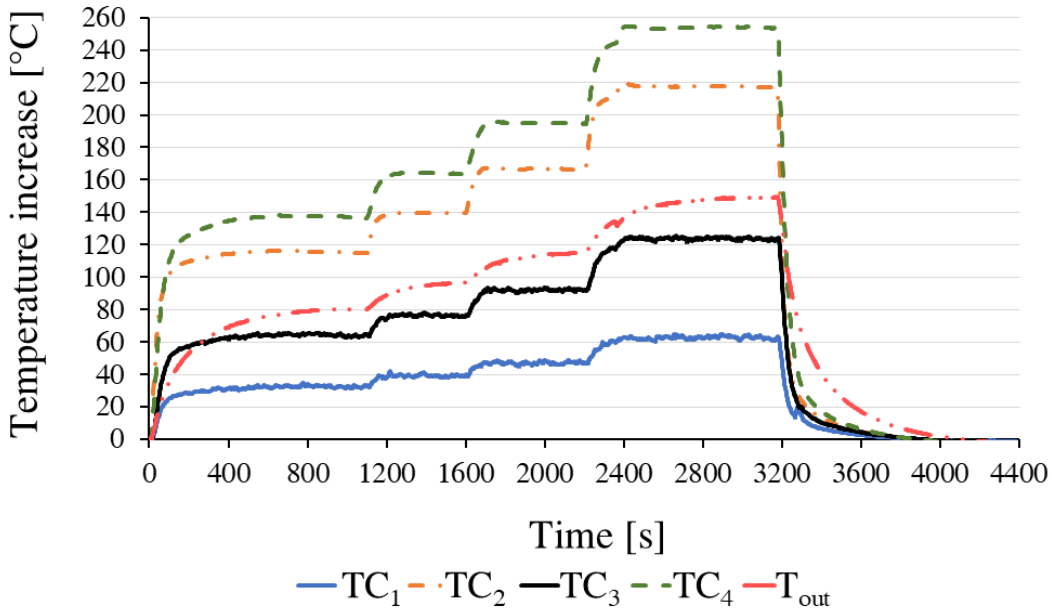


Fig. 4.14 An example of a test session with the mass flow rate of 0.5 g/s for sample with SplitP lattice. The temperature increase is referred to room temperature (derived from Ref. [204]).

effective conductivity of the lattice is inversely related to the porosity,

$$\varepsilon = \frac{V_{\text{Fluid}}}{V_{\text{Fluid}} + V_{\text{Solid}}} = \frac{1}{1 + V_{\text{Solid}}/V_{\text{Fluid}}}.$$

They attributed this behavior to the increase in wall thickness. In addition, thermal conductivity is influenced by geometry, unit cell size, and the surface roughness arising from 3D printing. Compared to the Diamond lattice, the SplitP lattice exhibits lower porosity and higher mass (see Table 4.5), which results in a higher effective conductivity and promotes conduction heat transfer from the heated surface to the back side of the sample.

The temperature increases (relative to initial temperatures) at the backside sensor, TC_3, and the outlet of the samples are illustrated in Figure 4.15. All measured temperatures for the SplitP sample are higher than those of the Diamond sample. In Figures 4.15c and d, the SplitP sample shows a larger increase in outlet temperature compared to the Diamond sample. This observation suggests that the SplitP lattice absorbs more heat overall while experiencing lower heat losses, consistent with the higher backside temperature readings recorded by TC_3 for the SplitP sample, as

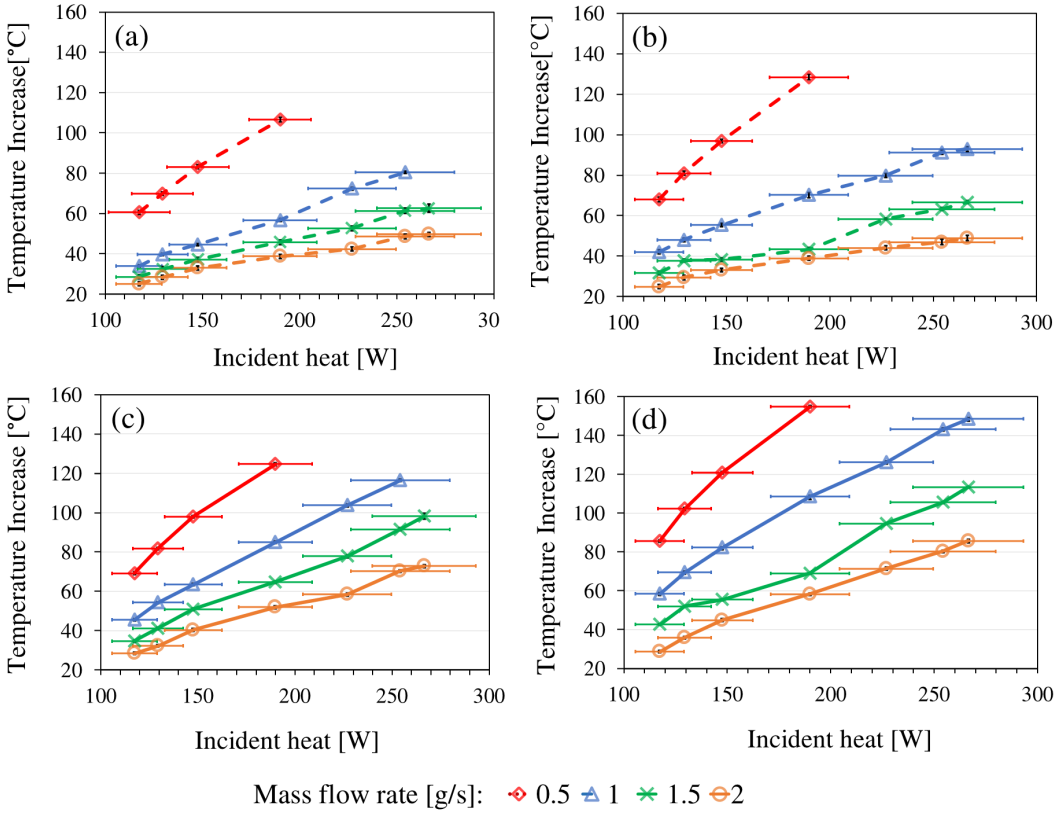


Fig. 4.15 Temperature rise (relative to the initial temperature) at TC_3 for (a) Diamond and (b) SplitP samples, and at the outlet for (c) Diamond and (d) SplitP samples (derived from Ref. [204]).

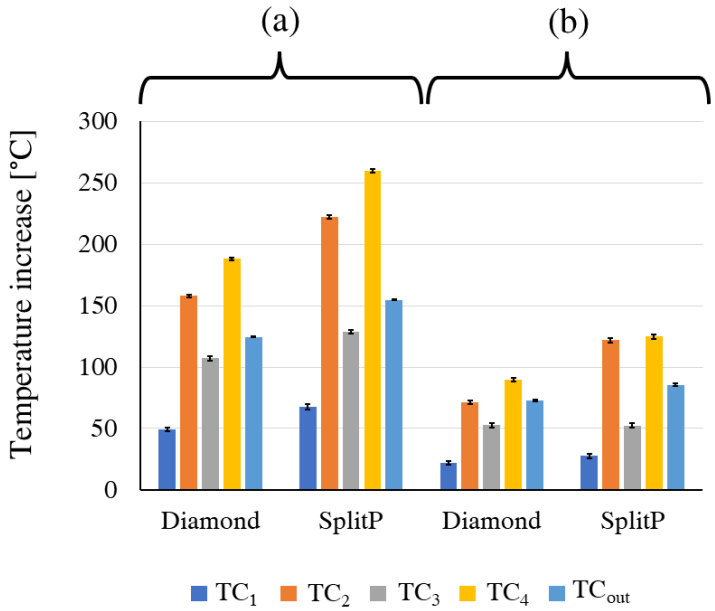


Fig. 4.16 Temperature increase (with respect to initial temperatures) of the four thermocouples on the samples for (a) mass flow rate of 0.5 and incident heat of 200 W and (b) mass flow rate of 2 g/s and the incident heat of 270 W (derived from Ref. [204]).

shown in Figures 4.15a and b. In Figure 4.16, the temperature increases (relative to initial temperatures) of all four thermocouples mounted on the samples, along with the outlet temperature, are shown for mass flow rates of 0.5 and 2 g/s at the highest incident heat flux levels tested for those conditions. For both samples, as expected, the temperatures measured by the thermocouples increase along the flow direction of the fluid. Notably, the temperatures recorded at the back face of the samples (TC_3) are consistently lower than those measured on the sides (TC_2 and TC_4), due to the latter sensors being located closer to the heated surface. Furthermore, the temperatures measured on the SplitP lattice sample are consistently higher than those of the Diamond lattice sample. However, it should be emphasized that direct comparisons of TC_2 and TC_4 between the two samples are not entirely reliable, as discussed in Section 4.2.1.

Useful Heat

The useful heat computed for each sample is presented in Figure 4.17 for different mass flow rates and incident heat fluxes. As expected, the useful heat increases with

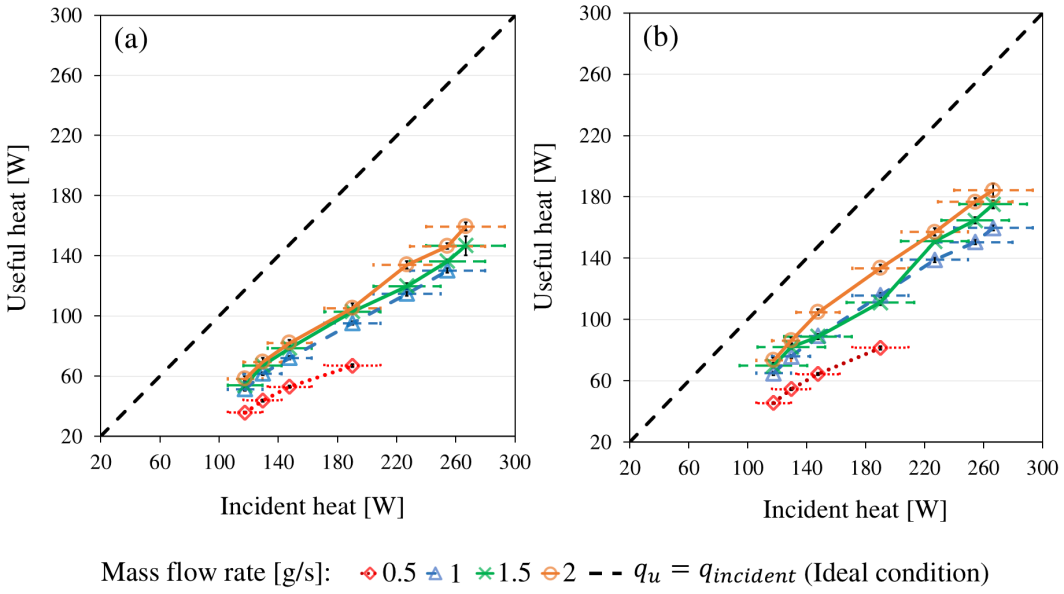


Fig. 4.17 Useful heat absorbed by the samples at different mass flow rates and incident heat fluxes for (a) Diamond and (b) SplitP samples (derived from Ref. [204]).

both mass flow rate and incident heat flux. With increasing heat flux, the useful heat progressively deviates from the ideal condition ($q_u = q_{\text{incident}}$), represented by the bisecting line plotted as a black dashed line in the figure. This deviation arises from the higher temperature levels reached by the samples at elevated incident heat fluxes, which lead to increased heat losses to the ambient. Across all mass flow rates and incident heat flux levels, the SplitP lattice sample demonstrates superior heat removal compared to its Diamond lattice counterpart.

Heat Loss and Efficiency

Figures 4.18a and b show the total heat loss from the receivers (calculated using Equation (4.31)), normalized by the incident heat. The results indicate that a significant fraction of the incident heat is dissipated to the environment—ranging from about 30% in the most favorable case (SplitP lattice at 2 g/s) to about 70% in the least favorable case (Diamond lattice at 0.5 g/s). As expected, increasing the mass flow rate reduces the heat losses for both samples, as more effective cooling occurs, limiting the temperature rise of the receiver for a given incident heat value. Increasing the incident heat from its minimum to maximum value seems to slightly decrease the loss ratio; however, this observation cannot be considered reliable due to the level of

uncertainties. Across all tested conditions, the SplitP lattice sample exhibits a lower loss ratio, which can be attributed to its greater absorption of incident heat. It should be emphasized that temperature measurements were not taken on the heated surface of the samples, as previously discussed in Section 4.2.1. Additional information such as the hotspot temperature on the heated surface are provided through the numerical study in Section 4.3.

To evaluate the thermal performance of each design under different heat flux levels and mass flow rates, the thermal efficiency, defined by Equation (4.19), was calculated and is presented in Figures 4.18c and d. As expected, thermal efficiency increases with higher mass flow rates; however, it shows a tendency to stabilize at the largest flow rate values. The SplitP sample consistently demonstrates superior performance, with the highest efficiency achieved at a mass flow rate of 2 g/s, reaching approximately 70%, compared to nearly 60% for the Diamond sample. Table 4.10 summarizes thermal efficiencies reported for various solar air heaters operating within a comparable range of mass flow rates. Even at lower flow rates, the efficiencies obtained in the present study exceed those typically reported for conventional solar air heaters, highlighting the advantages of TPMS lattice integration. The

Table 4.10 Thermal efficiencies of different solar air heaters, in a mass flow rate range relevant to the present study (derived from Ref. [204]).

Solar air heater	**Maximum η_{th} (%)**	**Flow rate of air**
CSP [a] [211]	$\sim$ 50%	0.0019–0.002 m^3/s
PTC with internal fins [212]	$\sim$ 45%	0.0016–0.0086 m^3/s
Conical concentrator [213]	$\sim$ 20%	8.3 g/s
FPC [b] with CPC [214]	$\sim$ 30%	2.2 g/s
Double-pass unglazed FPC with perforated absorber plate and packing wire mesh layers [215]	$\sim$ 15%	3 g/s
FPC [216]	$\sim$ 35%	4 g/s

[a] Compound parabolic concentrator.
[b] Flat plate collector.

exergetic efficiency, computed from Equations (4.21), is shown in Figures 4.18e and f. Once again, the SplitP sample outperforms the Diamond sample. The maximum exergetic efficiency was observed at a mass flow rate of 1 g/s, reaching about 12% for SplitP at an incident heat of $\sim$270 W, compared to nearly 8.5% for Diamond at

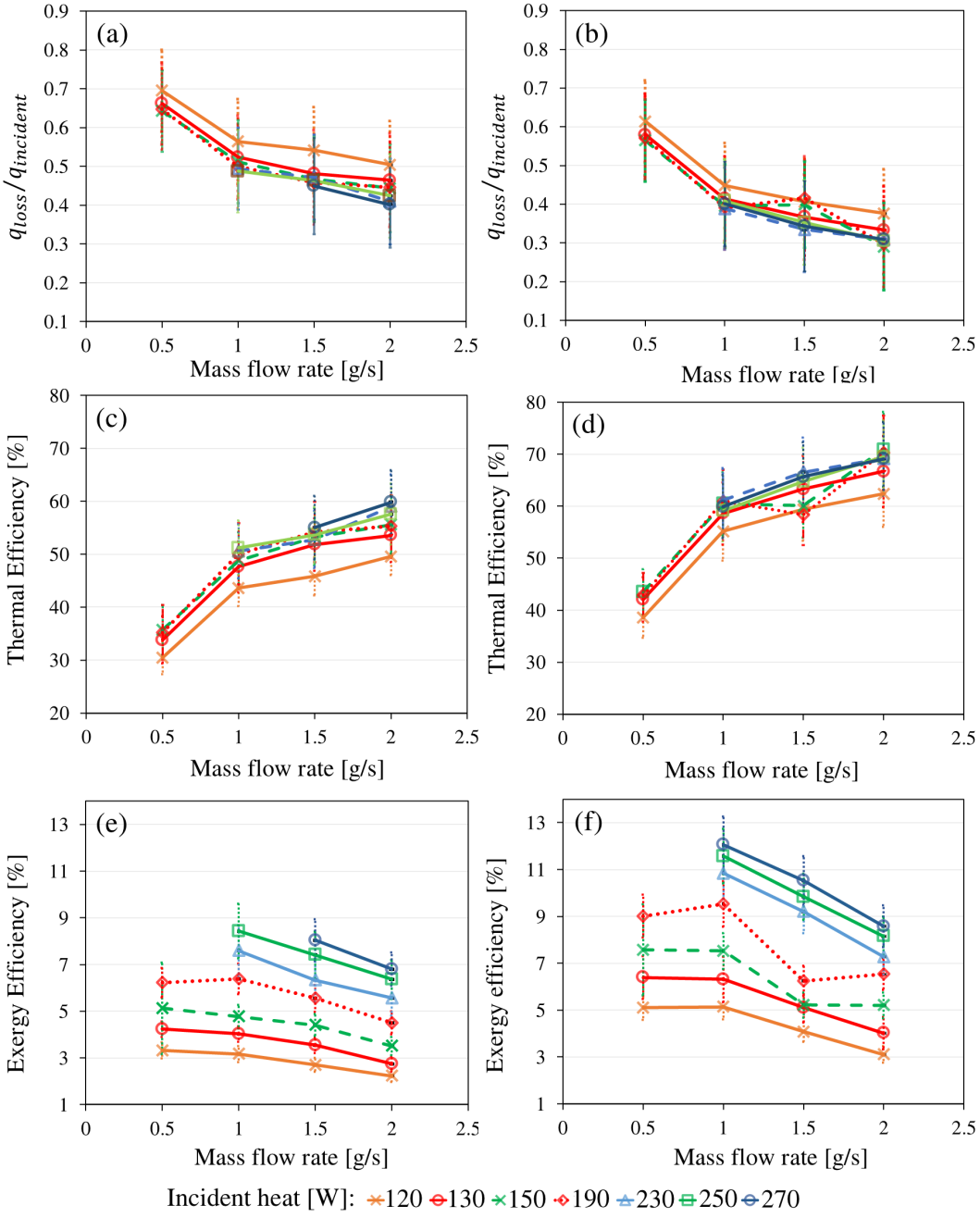


Fig. 4.18 Normalized heat loss for (a) Diamond and (b) SplitP samples, thermal efficiency for (c) Diamond and (d) SplitP samples, and exergetic efficiency for (e) Diamond and (f) SplitP samples (derived from Ref. [204]).

$\sim$250 W. Conversely, the lowest exergetic efficiencies were obtained at the highest flow rate under the lowest incident heat. For a given mass flow rate, exergy efficiency generally increases with higher heat fluxes; however, this is not the case with the increase in the mass flow rate. A review of the literature indicates that solar air heaters with various roughness geometries typically achieve maximum exergy efficiencies below 1.5% at comparable Reynolds numbers [216–218]. Similarly, in concentrated solar power systems employing Raschig Rings as porous insert, maximum exergy efficiencies below 5% have been reported at heat fluxes of 200 kW/m^2 [208].

4.3 Numerical Investigation of Point-focus Receivers with TPMS

Following the experimental investigation of planar high-temperature solar receivers equipped with TPMS lattices, namely Diamond and SplitP, this section focuses on a numerical analysis of the same samples. The motivation for the study is to complement and extend the insights gained from the experiments, enabling a deeper understanding of the thermal behavior of the receivers under controlled conditions. Despite this, the numerical study aims to validate the computational models against experimental data and to identify the most suitable RANS turbulence model. It also provides insights that are difficult to obtain experimentally, such as surface temperature distributions and localized heat transfer characteristics. This section thus bridges the experimental findings with computational predictions, highlighting the capability of numerical modeling to complement and enhance the understanding of TPMS-based solar receivers.

This study was conducted in collaboration with the MAHTEP research group, and the results were published in Ref. [219].

4.3.1 Numerical Model Setup and Boundary Conditions

The three-dimensional CAD models of the two planar receivers, developed in Section 4.2, were imported into *STAR-CCM+* [183] for further numerical investigation. A conjugate heat-transfer model was developed for the samples, where the heat conduction in the solid domains and the convective heat transfer in the fluid domain

were solved in a coupled manner. The model considered the non-uniform, one-sided heat flux applied in the experiments, as well as convection and radiation losses to the ambient environment. In addition, different RANS turbulence models were evaluated to determine their accuracy, namely the Lag EB κ-ε, κ-ω SST (Menter), and Realizable κ-ε two-layer models.

This section aims to replicate the experimental tests under the heat flux of 200 kW/m^2 for different mass flow rates (see Table 4.11). It should be noted that, as mentioned in Section 4.2, hydraulic measurements are not included in this study due to the negligible pressure drops across the samples observed in the experimental study (i.e., below the uncertainty of the pressure gauge). The input variables, including the inlet temperature, ambient temperature, and mass flow rate, were obtained from the recorded data of the experimental campaign. The Reynolds number corresponding

Table 4.11 Experimental test parameters measured during the campaign and used for model development (derived from Ref. [219]).

Mass flow rate (g/s)	**Peak heat flux** (kW/m^2)	$\Delta T_{\text{Diamond}}$ $(T_{outlet} - T_{inlet})\,(K)$	ΔT_{SplitP} $(T_{outlet} - T_{inlet})\,(K)$
0.5	200	125	155
1	200	87	109
1.5	200	66	71
2	200	53	65

to the mass flow rates ranges from 430 to 1700 for the SplitP lattice, and from 530 to 2100 for the Diamond. Therefore, the flow is assumed to be in the inertial regime.

The incident heat flux (HF) used as input in the simulations was modeled using Equation 4.28 derived from the best fit to experimental data along the x and y axes. Radiative, $q_{loss,\text{rad}}$, and convective, $q_{loss,\text{conv}}$, heat loss rates were applied to all surfaces of the receiver except for the bottom surface. In the experiments, the bottom surface was covered with insulation to protect the thermocouples from direct exposure to the incident heat flux (see Figure 4.12b). Consequently, an adiabatic boundary condition was applied to the bottom side of the receivers. Since in the experiments the results were obtained after a quasi-steady-state condition was reached; therefore, the simulations were performed under steady-state conditions.

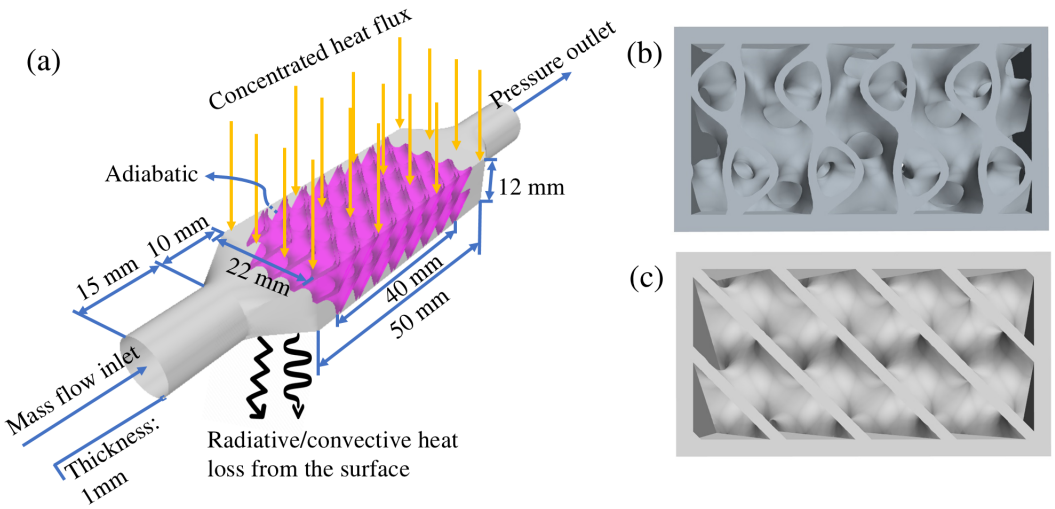


Fig. 4.19 Geometry and boundary conditions of the mock-ups: (a) overall view; cross-sectional view at the middle of the receiver with (b) SplitP lattice and (c) Diamond lattice (derived from Ref. [219] with modifications).

The heat loss rate is calculated as:

$$q_{loss,\mathrm{conv}} = h_{\mathrm{loss}}\,(T_{\mathrm{abs}} - T_{\mathrm{amb}}), \tag{4.38}$$

$$q_{loss,\mathrm{rad}} = \sigma\,\varepsilon_{\mathrm{abs}}\,(T_{\mathrm{abs}}^4 - T_{\mathrm{amb}}^4). \tag{4.39}$$

Where, h_{loss} is the convective heat transfer coefficient associated with heat loss to the ambient, assumed to be 10 W/(m^2·K). This value was chosen consistent with comparable studies in the literature [72, 220]. To assess the influence of this assumption, a sensitivity analysis was performed by varying the convective heat transfer coefficient from 5 to 20 W/(m^2·K) for the worst-case scenario, corresponding to the highest rate of heat loss (Diamond lattice with a mass flow rate of 0.5 g/s). Over this range, the receiver thermal efficiency decreased by 4.15%. The resulting normalized sensitivity coefficient—defined as the relative change in the output (η_{th}) resulting from a relative change in the input parameter (h_{loss})—was −0.0138, indicating that the receiver thermal efficiency exhibits relatively low sensitivity to the assumed convective heat transfer coefficient within the investigated range.

In Eq. 4.39, the symbol σ denotes the Stefan–Boltzmann constant, while $\varepsilon_{\mathrm{abs}}$ is the receiver emissivity. The receiver surface was assumed to be grey, so that $\varepsilon_{\mathrm{abs}} = \alpha$. Moreover, T_{abs} and T_{amb} denote the temperature of the external wall of the receiver and the ambient temperature, respectively. A schematic of the geometry

and boundary conditions is shown in Figure 4.19a, with a cross-sectional view at the middle of the samples presented in Figures 4.19b and c. More information regarding the geometries could be seen in Figure 4.9.

The useful heat can be calculated from

$$q_{\mathrm{u}} = \alpha\, q_{incident} - (q_{loss,\mathrm{conv}} + q_{loss,\mathrm{rad}}) \tag{4.40}$$

where α is the receiver absorptivity, representing the fraction of incident heat absorbed by the samples. Boydağ [221] studied the optical properties of different stainless steels for high-temperature applications. According to Boydağ, the exposure of stainless-steel solar receivers to high-flux solar radiation leads to oxidation, altering the surface optical properties. As observed by Cantone et al. [222], for a similar heat flux range, oxidation occurs on uncoated receivers. In this study, an absorptivity of 0.59 was used, based on Ref. [221], corresponding to a similar level of oxidation. The validity of this value was verified in Figure 4.20, where the thermal efficiency from numerical results was compared to experimental data, showing good agreement.

In the simulations, the specific heat at constant pressure, c_p, was evaluated at the arithmetic mean temperature between the inlet and outlet, while the air inlet and outlet temperatures correspond to the adiabatic mean values. The thermal efficiency is defined as in Equation (4.19).

The HTF in the tests was synthetic air, composed of 79% nitrogen and 21% oxygen. In the simulations, the same non-reacting multi-component gas mixture was assumed to behave as an ideal gas with temperature-dependent properties, matching the experimental composition.

4.3.2 Grid Study

To solve the governing equations, a polyhedral mesh was used with prismatic layers in the fluid region to accurately capture high temperature and velocity gradients near the walls. A comprehensive grid study was performed to assess the accuracy of the results with respect to discretization errors. Four different grids were generated and simulated using various RANS models, comparing both the pressure drop and the useful heat. Table 4.12 presents the grid study results for the Lag EB κ-ε RANS

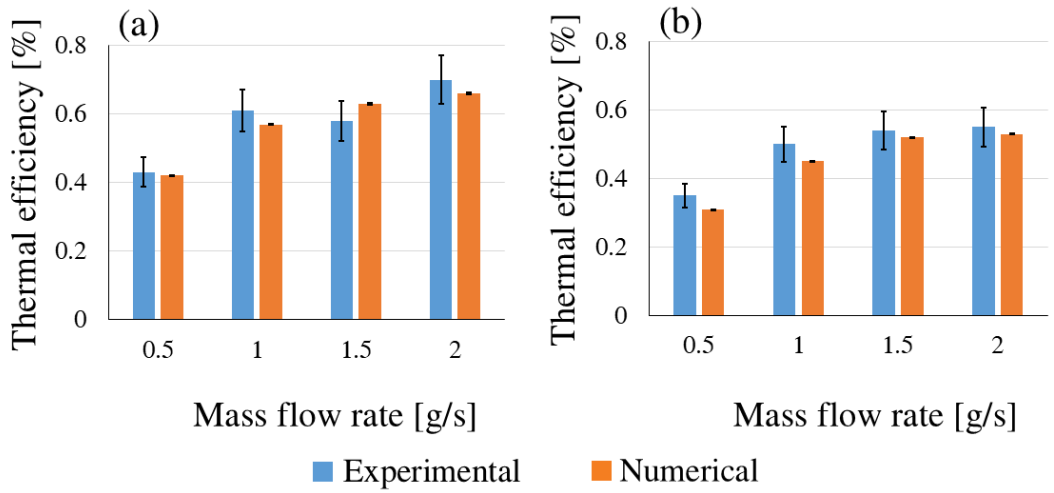


Fig. 4.20 Thermal efficiency comparison between experimental and numerical (from Lag EB κ-ε model) results for different mass flow rates for (a) SplitP lattice (b) Diamond lattice (derived from Ref. [219]).

model. In this table, each grid is identified by the first letter of the lattice and numbered from the finest to the coarsest grid; for example, S3 represents the finest grid for the SplitP lattice, while S0 corresponds to the coarsest. The parameter r_{i3} denotes the ratio of the number of cells in the i-th grid to that of the finest grid (grid number 3). To estimate the uncertainty in the results due to discretization error, the GCI was calculated using the least squares approach.

Table 4.12 Grid study for the Lag EB κ-ε RANS model (derived from Ref. [219]).

Grid ID	**Number of cells**	r_{i3}	**Average cell size** Δh **(m)**	$\Delta p/\Delta p_{finest}$	$q_u/q_{u,finest}$
S3	5.07×10^6	1.000	1.59×10^{-4}	1.000	1.0000
S2	4.21×10^6	0.848	1.69×10^{-4}	1.007	1.0003
S1	3.30×10^6	0.668	1.83×10^{-4}	1.011	0.9983
S0	2.39×10^6	0.484	2.04×10^{-4}	1.072	0.9985
D3	2.84×10^6	1.000	1.92×10^{-4}	1.000	1.0000
D2	2.29×10^6	0.830	2.07×10^{-4}	0.985	1.0003
D1	2.09×10^6	0.760	2.13×10^{-4}	0.963	0.9992
D0	1.95×10^6	0.713	2.07×10^{-4}	0.944	0.9977

4.3.3 Validation of the Results

Effects of the Turbulence Model

In Figure 4.21, q_u obtained from different RANS turbulence models is compared. For both samples, the Lag EB κ-ε and κ-ω SST (Menter) models exhibited the smallest deviation from the experimental results. For nearly all mass flow rates, the experimental values are slightly higher than the corresponding numerical predictions. This discrepancy could be attributed to the effect of surface roughness, which was not considered in the numerical simulations. As shown in Figures 4.10a and b, the surfaces of the manufactured samples are relatively rough, which enhances heat transfer between the receiver and the HTF.

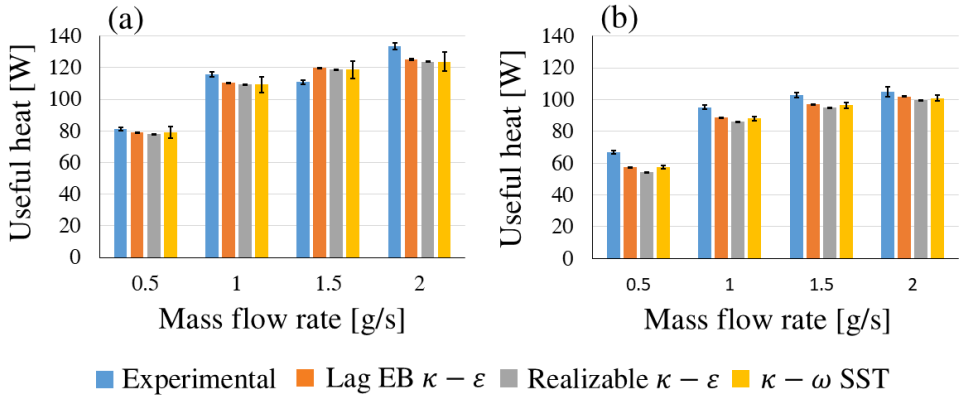


Fig. 4.21 Comparison of numerical results obtained with different RANS turbulence models for (a) SplitP and (b) Diamond lattices (derived from Ref. [219]).

Validation on the Wall Temperature Increases

To further validate the models, the wall temperatures of the samples at TC_2 and TC_4 were compared with experimental data. These two thermocouples were selected because, during the experiments, they exhibited better thermal contact with the samples. This was ensured by a screw-tightened clamp mechanism that held the alumina insulation against the bottom side of the receivers.However, it should be emphasized that the locations of these thermocouples were slightly different in the two mock-ups during the experiments; therefore, the temperature readings are not directly comparable. The locations of TC_2 and TC_4 for the receivers with Diamond

and SplitP lattices can be seen in Figures 4.22a and b, respectively. Figure 4.23 shows the temperature increases of TC_2 and TC_4 relative to their initial temperatures. A good agreement is observed in Figure 4.23 between the results from the Lag EB κ-ε model and the experimental measurements.

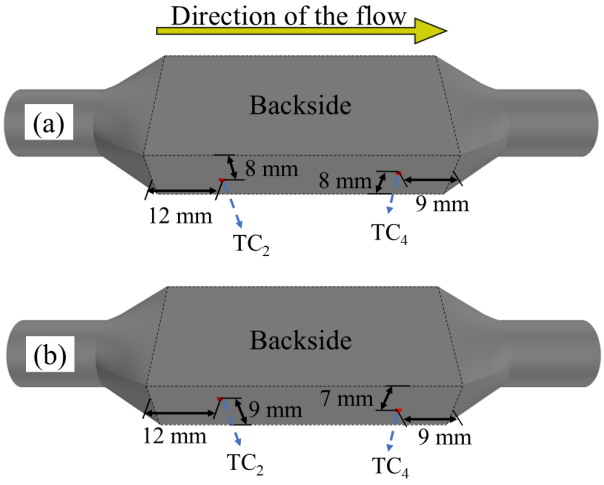


Fig. 4.22 Location of TC_2 and TC_4 for the receiver with (a) the Diamond and (b) the SplitP lattices

Thermal Analyses

The hotspot temperatures of the samples are shown in Figure 4.24a, while the corresponding temperature maps for the most critical mass flow rate (0.5 g/s) are presented in Figures 4.24b and c. The hotspot is located near the outlet, with the SplitP lattice exhibiting a slightly lower maximum temperature. As observed in Figure 4.24b, the high-temperature region extends over a wider area in the Diamond lattice. The superior heat removal of the SplitP lattice can be attributed to its higher effective thermal conductivity compared to the Diamond lattice as discussed in Section 4.2. In addition, its enhanced thermal performance is supported by a larger surface-to-volume ratio (1.43 mm^{-1} for SplitP versus 1.06 mm^{-1} for Diamond) and more complex flow channels, which promote improved mixing of the HTF.

In Figure 4.25, the useful heat predicted by the Lag EB κ-ε model is compared for the two lattices. The results are consistent with the experimental data of Section 4.2, where the SplitP lattice exhibited higher useful heat.

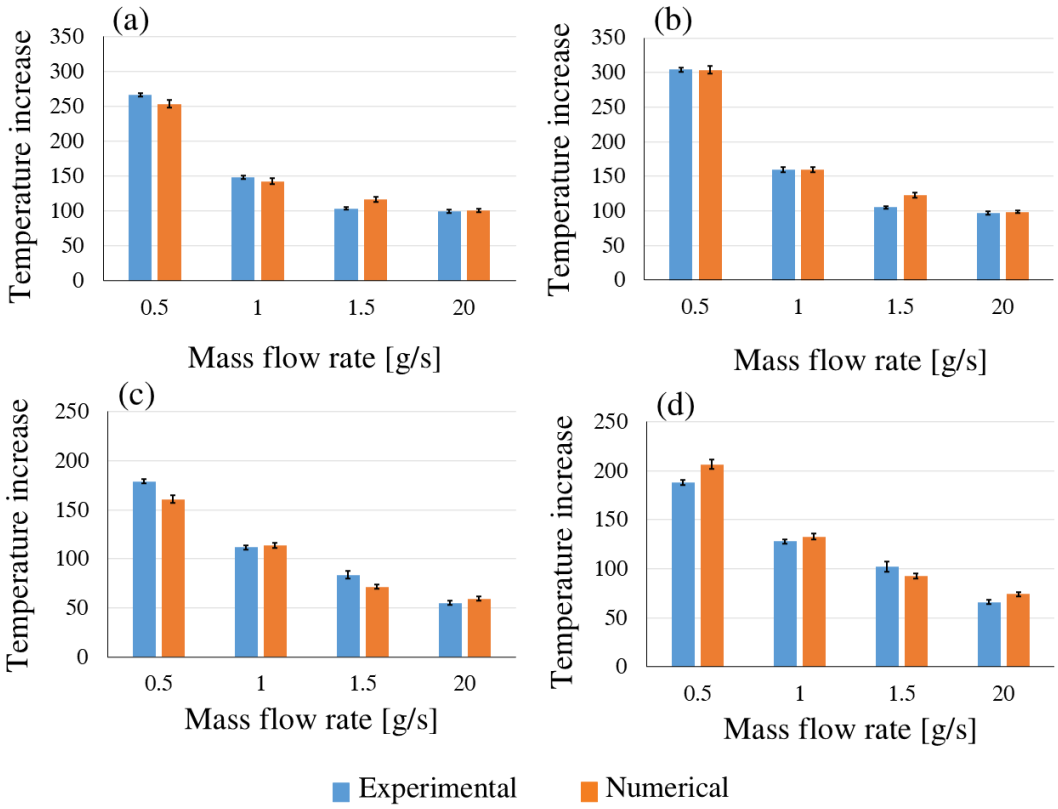


Fig. 4.23 Temperature rise relative to the initial temperature for the SplitP lattice at (a) TC_2 and (b) TC_4, and for the Diamond lattice at (c) TC_2 and (d) TC_4 (derived from Ref. [219]).

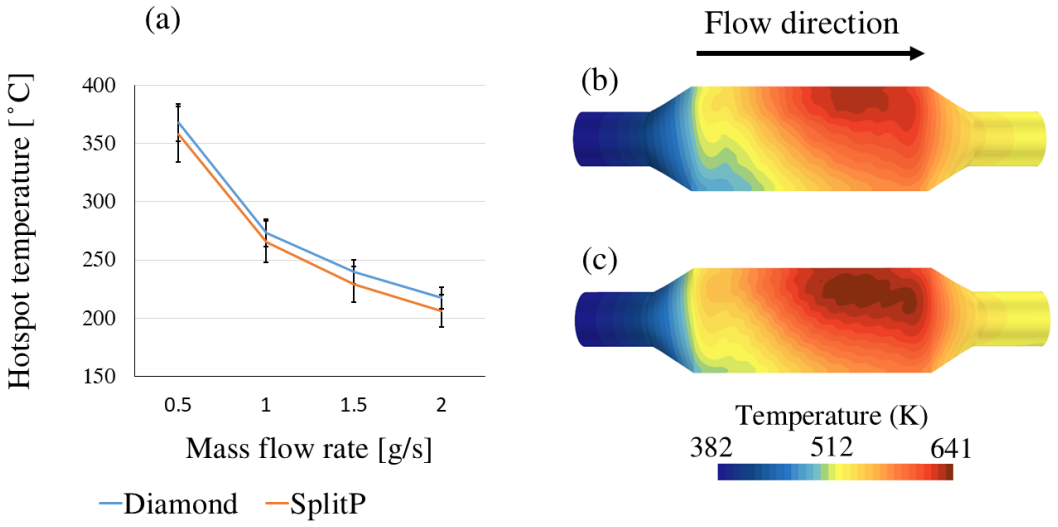


Fig. 4.24 (a) Hotspot temperatures of the mock-ups for the studied mass flow rates; temperature maps at a mass flow rate of 0.5 g/s for (b) SplitP and (c) Diamond lattices (derived from Ref. [219]).

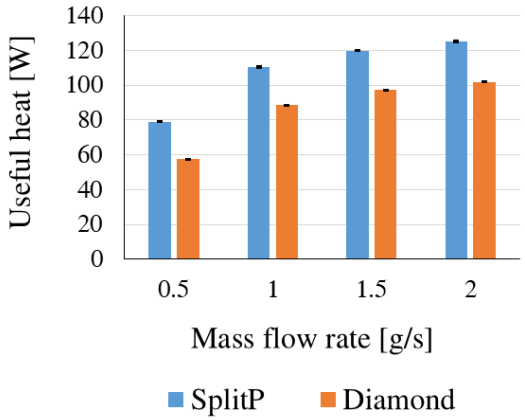


Fig. 4.25 Comparison of useful heat between the two lattices obtained with the Lag EB κ-ε model (derived from Ref. [219]).

4.3.4 Conclusions

This chapter explored the application of TPMS lattices in high-temperature CSP systems. The study began with a numerical analysis of the performance of four TPMS lattices—Diamond, Gyroid, SplitP, and Lidinoid—within a segment of a tubular receiver of a PTC (Section 4.1). Building on this, two planar receivers incorporating Diamond and SplitP lattices were investigated experimentally (Section 4.2) and subsequently examined numerically using different RANS turbulence models (Section 4.3).

The performance of the tubular receivers was examined in terms of the augmentation entropy generation number ($\dot{N}_S$) as well as thermal and exergetic efficiencies, considering two unit-cell sizes (10 mm and 20 mm) under a range of inlet temperatures. Across all configurations, the smaller unit-cell size consistently led to better thermal performance . This improvement can be attributed to enhanced heat transfer between the solid lattice and the working fluid, which resulted in more uniform temperature distributions and lower wall temperatures. Among the lattice geometries, the SplitP and Lidinoid designs stood out. They achieved the lowest wall temperatures and the highest thermal and exergetic efficiencies by promoting efficient heat spreading within the solid, reducing local hotspots, and improving overall thermal uniformity. While the Diamond lattice performed reasonably well, particularly for the smaller unit-cell size, it showed slightly higher external surface temperatures and lower thermal efficiency compared to the SplitP and Lidinoid

lattices. In contrast, the Gyroid lattice exhibited the highest total entropy generation and the lowest thermal efficiency across both unit-cell sizes, while also producing the lowest pressure drop. These findings align well with the experimental results presented in Section 4.2, where the SplitP lattice outperformed the Diamond lattice in exergetic performance. Overall, the results indicate that the SplitP and Lidinoid lattices are the most promising TPMS designs for solar receiver applications, due to their ability to distribute heat more evenly, minimize entropy generation, and obtain high thermal and exergetic efficiencies.

As far as the comparison between the Lidinoid and SplitP lattices is concerned, the former resulted in slightly lower hotspot temperatures but higher pressure drops compared to the SplitP lattice. Nearly equal values of $\dot{N}_S$ for the unit-cell size of 10 mm indicate an almost identical trade-off between these lattices. However, for the unit-cell size of 20 mm, the Lidinoid lattice yields lower values of $\dot{N}_S$, indicating its superiority.

For all cases, $\dot{N}_S$ decreased with increasing inlet temperature up to a certain point—between 450 K and 500 K—and then began to rise again. Smaller unit-cell sizes consistently showed lower entropy generation.With the increase in inlet temperature, the thermal efficiency does not decrease significantly and remains at approximately 70% at the highest inlet temperature, highlighting the ability of TPMS structures to effectively dissipate heat despite the reduced temperature gradient between the solid structure and the HTF.

It should be emphasized that, for all lattices—even in the worst cases—$\dot{N}_S$ remains well below unity and the thermal efficiency is equal to or higher than 70%, demonstrating the significant effectiveness of this family of lattices.

Based on the obtained insights, the SplitP and Diamond lattices (with unit-cell size of 10 mm) were selected for further experimental investigation. Among the four lattices studied previously, SplitP demonstrated one of the highest performances, despite having received relatively little attention in the literature. However, Diamond is a well-known TPMS lattice with promising performance. Two stainless steel planar receiver mock-ups incorporating these lattices were manufactured via additive manufacturing and tested at the IMDEA Energy Institute. Their thermal performance was evaluated under four different mass flow rates and seven incident heat flux levels using synthetic air as the working fluid. Key observations from this experimental campaign include:

- The maximum thermal efficiency was achieved at the highest mass flow rate of 2 g/s, reaching approximately 70% for the SplitP sample and around 60% for the Diamond sample. This result is particularly noteworthy given that the Diamond lattice has previously been considered the superior TPMS choice by several researchers, excluding SplitP.
- The highest exergetic efficiency occurred at a mass flow rate of 1 g/s, attaining approximately 12% for SplitP at ∼270 W, and 8.5% for Diamond at ∼250 W.
- Increasing the mass flow rate reduces the $q_{\text{loss}}/q_{\text{incident}}$ ratio, as a larger fraction of the incident heat is absorbed by the HTF.
- The SplitP lattice sample demonstrated superior thermal performance, with higher useful heat and lower heat losses compared to the Diamond sample. This is likely related to a lower temperature on the heated surface; however, this hypothesis requires verification through numerical modeling, since the heated surface temperature was not measured directly.

The same mock-ups were examined numerically to complement the experimental results and gain a more detailed understanding of their thermal behavior. These simulations provided additional insights that are challenging to obtain experimentally, such as detailed surface temperature distributions and hotspot locations.

Three RANS turbulence models—Lag EB κ-ε, κ-ω SST (Menter), and Realizable κ-ε two-layer—were evaluated against the experimental data. Among them, the Lag EB κ-ε and κ-ω SST (Menter) models showed the closest agreement with experiments. All models slightly underestimated the useful heat, likely due to the roughness of the manufactured surfaces, which was not included in the simulations. Wall temperature increases at locations TC_2 and TC_4 were compared with experimental measurements, showing good agreement. The SplitP lattice consistently outperformed the Diamond lattice, achieving higher thermal efficiency, greater useful heat, and lower hotspot temperatures. Furthermore, the high-temperature region in the SplitP lattice was more confined compared to the Diamond lattice, reflecting more efficient thermal management.

Chapter 5

Conclusions and Perspectives

This dissertation focused on heat transfer enhancement for renewable energy applications. The target technologies were latent heat thermal energy storage systems and high-temperature concentrating solar power receivers. A previously developed high-performance cubic latent heat thermal energy storage system was selected as the reference case, and its thermal performance was improved through a topology optimization approach. In the case of concentrating solar power receivers, a small segment of the tubular receiver of a parabolic trough collector incorporating four different triply periodic minimal surface lattices—namely Diamond, Gyroid, SplitP, and Lidinoid—was first investigated numerically. Subsequently, two planar receivers incorporating Diamond and SplitP lattices were investigated through both experimental and numerical analyses.

5.1 Concluding Remarks

In Chapter 3, the effectiveness of topology optimization in enhancing the thermal performance of latent heat thermal energy storage devices—even with a simplified 2D optimization approach—was demonstrated. The optimized fin geometry, featuring branched structures extending throughout the domain of the phase-change material (paraffin wax), promotes a more uniform temperature distribution and accelerates phase-change processes. Compared to the reference design, the topology-optimized system exhibited notable improvements in thermal response times, with reductions of 5.6% and 7.6% in the time required to store and release 90% of the latent heat,

respectively. The optimized device also achieved faster phase-change dynamics, reaching 90% paraffin solidification 12.3% earlier during discharge and 90% paraffin melting 9.4% earlier during charge, relative to the reference case. These improvements were achieved despite the fact that the reference case already featured a novel design and exhibited significantly high performance.

The Thermal Uniformity Index analysis indicates that the optimized fin geometry generally enhances thermal uniformity compared with the reference case. A short period of reduced performance is observed, attributed to the absence of fins in the central region of the phase change material domain, which results in localized temperature non-uniformities.

Analysis of energy contributions revealed that latent heat accounts for nearly 30% of the total energy stored and released, highlighting the critical role of the phase change material in thermal energy storage. Sensible heat stored in the aluminum matrix contributes about 22% of the total energy, while the paraffin itself stores approximately 50% of the sensible heat outside its phase-change temperature range, demonstrating its significant contribution to the system's thermal inertia. This effective combination of latent and sensible heat storage mechanisms enhances the energy density and allows the system to store substantial energy at relatively lower heat transfer fluid temperatures, improving overall efficiency while minimizing thermal losses.

Overall, the topology-optimized latent heat thermal energy storage design presents a promising approach to improving the thermal performance and efficiency of energy storage systems based on phase-change material. It enables faster charge–discharge cycles and more effective thermal management in practical applications. The development of more efficient latent heat thermal energy storage devices can significantly promote their deployment in real-world applications, including solar thermal energy storage and industrial heat management, by providing faster thermal response, higher energy density, and more effective integration with renewable energy sources.

Chapter 4 investigated the application of lattices based on triply periodic minimal surfaces in high-temperature concentrating solar power receivers through a combined numerical and experimental approach. Four lattice geometries—Diamond, Gyroid, SplitP, and Lidinoid—were first evaluated numerically in tubular receiver configurations, followed by experimental and numerical analyses of planar receivers incorporating selected designs. The results consistently demonstrate that reducing

the unit-cell size enhances thermal performance by promoting more effective heat transfer between the solid lattice and the working fluid, leading to improved temperature uniformity and lower wall temperatures. Among the investigated geometries, the SplitP and Lidinoid lattices exhibited the best overall performance, achieving lower hotspot temperatures, reduced entropy generation, and higher thermal and exergetic efficiencies. In contrast, the Gyroid lattice showed the highest entropy generation and lowest thermal efficiency, despite offering lower pressure drops. A detailed comparison between the SplitP and Lidinoid lattices revealed a similar thermodynamic performance for the smaller unit-cell size, with nearly identical entropy generation levels. For the larger unit-cell size, however, the Lidinoid lattice showed a slight advantage in terms of reduced entropy generation, while the SplitP lattice maintained lower pressure losses, highlighting a trade-off between thermal performance and hydraulic efficiency.

The analysis further showed that entropy generation decreases with increasing inlet temperature up to an intermediate range, after which it increases again. Although the thermal efficiency decreases slightly with increasing inlet temperature, it remains relatively stable and above approximately 70% across all operating conditions, demonstrating the strong heat dissipation capability of triply periodic minimal surface-based receiver designs even at reduced temperature gradients. Notably, all configurations exhibited $\dot{N}_S$ values well below unity, confirming their high thermodynamic effectiveness.

Based on these findings, the SplitP and Diamond lattices were selected for experimental validation. The experimental results demonstrated that the SplitP lattice outperforms the Diamond lattice, achieving higher thermal and exergetic efficiencies, greater useful heat transfer, and lower heat losses. These improvements are attributed to enhanced heat spreading and lower surface temperatures in the SplitP configuration.

Complementary numerical simulations of the experimental configurations provided further insight into their thermal behavior. Among the evaluated Reynolds-averaged Navier-Stokes turbulence models, the Lag EB κ-ε and κ-ω SST models showed the best agreement with experimental data. Minor discrepancies, including slight underprediction of useful heat, were attributed to the omission of surface roughness effects in the simulations. The numerical results confirmed the superior

performance of the SplitP lattice, which exhibited more confined hotspot regions and more effective thermal management compared to the Diamond lattice.

Overall, the results highlight the strong potential of triply periodic minimal surface lattices—particularly SplitP and Lidinoid—for advanced solar receiver applications, offering a favorable balance between heat transfer enhancement, entropy minimization, and thermal efficiency.

5.2 Perspectives

As discussed in Section 3.5, several hotspots appeared during the discharge process of the optimized latent heat thermal energy storage device which took place mainly in areas with limited aluminum connectivity and farther from the heat transfer surface. Achieving a uniform temperature distribution within the phase-change material was the main goal, but this was constrained by the fixed aluminum volume fraction, which was kept constant to allow a fair comparison with the reference device. Although this constraint is necessary for benchmarking, it inevitably lowers the effective thermal conductivity of the structure, slowing heat diffusion and leading to localized hotspots. These temperature non-uniformities can, in turn, influence both the rate and completeness of energy recovery. Increasing the aluminum volume fraction can mitigate hotspots by enhancing the effective thermal conductivity; however, this comes at the cost of reduced content of the phase-change material and, consequently, lower latent heat storage capacity. Future work could investigate how varying the aluminum fraction affects the trade-off between thermal performance and energy density. A multi-objective optimization could then be used to map the Pareto front between discharge speed and latent heat capacity, helping identify the most suitable design for different applications.

It should be noted that the presented topology optimization was conducted in a simplified 2D domain, with the resulting geometry extruded to construct the 3D model used for performance evaluation. This approach significantly reduces computational effort while capturing the essential thermal and structural characteristics, but it inherently limits design freedom compared to a full 3D optimization. Performing the optimization directly in 3D could yield more realistic and potentially more efficient configurations; however, such analyses are considerably more computationally demanding, especially when coupled with transient heat transfer and

phase-change modeling. Full 3D topology optimization is therefore left for future work as computational resources become more accessible.

It is also crucial to consider long-term stability and durability. Although the present study focuses on thermal performance during a single charge–discharge cycle, structural integrity under repeated thermal cycling is a key factor for practical applications. Morciano et al. [40] reported stable performance over repeated cycles, but factors such as thermal expansion, degradation of the phase-change material, and mechanical stresses induced by melting and solidification could affect long-term behavior. Future work should include thermo-mechanical simulations or accelerated thermal cycling tests to evaluate the durability and lifetime of the topology-optimized design. Such studies would clarify whether the branched fin structures can maintain performance and integrity over extended operation.

Moreover, the current numerical model assumes idealized conditions, including negligible heat losses to the environment and a constant temperature at the heat transfer fluid channel surfaces, as in Ref. [112]. In practice, non-ideal phase-change material behavior (e.g., subcooling, hysteresis), thermal contact resistance, and environmental heat losses may lead to deviations from the simulated performance. Given the small scale of the device and the low heat transfer fluid velocity in the reference case, the assumptions of negligible axial temperature gradients and constant wall temperature are reasonable; nevertheless, future studies should incorporate these effects or perform experimental validation to assess the accuracy of the numerical predictions.

Additive manufacturing allows the fabrication of complex geometries, including the proposed topology-optimized structures. Future work could involve producing a small-scale prototype for experimental testing, bridging the gap between the simplified numerical model and real operating conditions, and providing valuable insights into the practical applicability and performance of the optimized design.

Considering the effectiveness of the topology optimization approach, it can be employed to design high-performance solar receivers. By formulating a multi-objective problem that maximizes heat removal while minimizing pressure drop, highly efficient geometries can be achieved. Although a three-dimensional multi-objective topology optimization study is computationally expensive, it shows strong potential for improving the overall performance of solar receivers. In this context, a

simplified two-dimensional optimization study can provide a more computationally economical alternative.

The experimental conditions at the IMDEA Energy Institute imposed constraints that required the fabrication of relatively small receiver samples. The resulting thin wall thickness prevented the use of common techniques for ensuring proper thermocouple contact—such as drilling small holes—due to the risk of cracking or structural failure. In addition, defects such as small holes may be present within the walls of the triply periodic minimal surface lattice. However, verifying their presence would require invasive methods, such as cutting the samples.

Since the pressure drop across the mock-ups was negligible, future studies could investigate their performance using a liquid heat transfer fluid (e.g., water) to better assess their hydraulic behavior.

5.2.1 Artificial Intelligence-assisted Topology Optimization

Despite its benefits, the widespread adoption of topology optimization as a design tool is hindered by its high computational cost, which arises from the large number of design variables and the inherently iterative nature of the optimization process [223]. To mitigate these costs, artificial intelligence–assisted design methods for topology optimization have gained increasing attention. The model is initially trained on a dataset of topology-optimized solutions generated by conventional iterative methods. Once trained, it can be applied to solve topology optimization problems under different design setups and parameter configurations [224]. In such models, the optimized topology is obtained in a fraction of the time required by conventional approaches, as the computationally intensive tasks are shifted to the training phase, which is performed only once. The trained model can subsequently generate results that are used either directly, further refined using conventional optimization methods, or adapted to different target structure sizes [225].

The application of machine learning techniques to topology optimization can be categorized into seven distinct purposes [226]:

- **Acceleration of iteration:** Conventional iterative topology optimization is performed up to the intermediate stages. In the later stages, which are typically

the most time-consuming, machine learning techniques are employed to predict the final optimized topology and accelerate convergence.

- **Non-iterative optimization:** The optimized topology is directly predicted in a single step from the given design parameters, such as loading and boundary conditions, without performing an iterative optimization process.
- **Meta-modeling:** Machine learning models are used to approximate computationally expensive components of topology optimization, such as the objective function, sensitivity information, and constraints, thereby reducing the need for repeated finite element analyses.
- **Dimensionality reduction of design space:** High-dimensional design spaces are mapped into lower-dimensional latent spaces, enabling more efficient exploration and optimization while preserving essential structural features.
- **Improvement of optimizer:** Machine learning is applied to tune optimization parameters, reducing the trial-and-error effort and computational cost associated with manual parameter selection. In addition, density fields may be reparameterized using neural networks to enable more efficient and robust optimization.
- **Generative design:** Generative models are used to rapidly create multiple diverse topology-optimized designs, allowing exploration of a broad design space while maintaining acceptable structural performance.
- **Postprocessing:** Since machine learning-generated topologies are often low-resolution or exhibit gray-scale or unclear boundaries, postprocessing techniques are applied to enhance resolution and improve structural boundaries, resulting in manufacturable and physically meaningful designs.

While current machine-learning approaches offer substantial speed advantages, several practical challenges remain. Many methods rely on large pre-generated training datasets, which are expensive and time-consuming to produce, particularly for complex or three-dimensional problems. Moreover, data-driven predictions may suffer from limited physical reliability, poor connectivity, or manufacturability issues, necessitating additional refinement. Another key limitation is that many models are trained for specific boundary conditions and do not generalize well when these

conditions change, further restricting their applicability. Consequently, there exists a trade-off between efficiency and accuracy, as artificial intelligence-assisted methods, although faster, generally remain less accurate than conventional iterative topology optimization approaches [226]. These limitations suggest promising research directions toward physics-aware, data-efficient, and more generalizable learning methods capable of producing engineering-feasible designs.

Although numerous artificial intelligence-assisted topology optimization studies have focused on structural design, comparatively few have addressed conductive heat transfer [227–231] and fluid flow [232, 231]. This leaves a significant research gap and, consequently, substantial potential for further investigation of artificial intelligence–assisted topology optimization in the fields of fluid dynamics and heat transfer.

References

[1] IEA. Global Energy Review 2025. International Energy Agency, March 2025. https://www.iea.org/reports/global-energy-review-2025.

[2] Hannah Ritchie, Pablo Rosado, and Max Roser. Energy production and consumption. *Our World in Data*, 2020. https://archive.ourworldindata.org/20260402-173937/energy-production-consumption.html.

[3] EI. Statistical Review of World Energy 2025. Energy Institute, June 2025. https://www.energyinst.org/statistical-review.

[4] IEA. Global Energy Review 2024. International Energy Agency, October 2024. https://www.iea.org/reports/world-energy-outlook-2024.

[5] IRENA. Renewable Capacity Statistics 2025. International Renewable Energy Agency, March 2025. https://www.irena.org/Publications/2025/Mar/Renewable-capacity-statistics-2025.

[6] IEA. CO_2 Emissions in 2023. International Energy Agency, March 2024. https://www.iea.org/reports/co2-emissions-in-2023.

[7] UNEP. Global Environment Outlook 6. United Nations Environment Programme, 2019. https://www.unep.org/resources/global-environment-outlook-6.

[8] IPCC. IPCC Sixth Assessment Report. Intergovernmental Panel on Climate Change, 2022. https://www.ipcc.ch/report/ar6/wg2/.

[9] WHO. Ambient Air Pollution: A Global Assessment. World Health Organization, March 2023. https://www.iea.org/reports/co2-emissions-in-2023.

[10] IEA. Global Energy Review 2023. International Energy Agency, October 2023. https://www.iea.org/reports/world-energy-outlook-2023.

[11] IEA. Electricity 2024. International Energy Agency, January 2024. https://www.iea.org/reports/electricity-2024.

[12] Ehsanul Kabir, Pawan , Sandeep Kumar, Adedeji A Adelodun, and Ki-Hyun Kim. Solar energy: Potential and future prospects. *Renewable and Sustainable Energy Reviews*, 82:894–900, 2018. https://doi.org/10.1016/j.rser.2017.09.094.

[13] IEA. Technology Roadmap - Concentrating Solar Power. International Energy Agency, May 2010. https://www.iea.org/reports/technology-roadmap-concentrating-solar-power.

[14] Wenjin Ding and Thomas Bauer. Progress in research and development of molten chloride salt technology for next generation concentrated solar power plants. *Engineering*, 7(3):334–347, 2021. https://doi.org/10.1016/j.eng.2020.06.027.

[15] Basim Belgasim, Yasser Aldali, Mohammad JR Abdunnabi, Gamal Hashem, and Khaled Hossin. The potential of concentrating solar power (CSP) for electricity generation in Libya. *Renewable and sustainable energy reviews*, 90:1–15, 2018. https://doi.org/10.1016/j.rser.2018.03.045.

[16] Keith Lovegrove and Wes Stein. *Concentrating solar power technology: principles, developments and applications, 2nd ed.* Elsevier, 2020. https://doi.org/10.1016/j.rser.2018.03.045.

[17] Enas Taha Sayed, Abdul Ghani Olabi, Abdul Hai Alami, Ali Radwan, Ayman Mdallal, Ahmed Rezk, and Mohammad Ali Abdelkareem. Renewable energy and energy storage systems. *Energies*, 16(3):1415, 2023. https://doi.org/10.3390/en16031415.

[18] Gholamabbas Sadeghi. Energy storage on demand: Thermal energy storage development, materials, design, and integration challenges. *Energy Storage Materials*, 46:192–222, 2022. https://doi.org/10.1016/j.ensm.2022.01.017.

[19] Muhammad Imran Khan, Faisal Asfand, and Sami G Al-Ghamdi. Progress in research and technological advancements of thermal energy storage systems for concentrated solar power. *Journal of Energy Storage*, 55:105860, 2022. https://doi.org/10.1016/j.est.2022.105860.

[20] Mukrimin Sevket Guney and Yalcin Tepe. Classification and assessment of energy storage systems. *Renewable and sustainable energy reviews*, 75:1187–1197, 2017. https://doi.org/10.1016/j.rser.2016.11.102.

[21] Olivier Dumont, Guido Francesco Frate, Aditya Pillai, Steven Lecompte, Vincent Lemort, et al. Carnot battery technology: A state-of-the-art review. *Journal of Energy Storage*, 32:101756, 2020. https://doi.org/10.1016/j.est.2020.101756.

[22] Md Tasbirul Islam, Nazmul Huda, AB Abdullah, and Rahman Saidur. A comprehensive review of state-of-the-art concentrating solar power (CSP) technologies: Current status and research trends. *Renewable and Sustainable Energy Reviews*, 91:987–1018, 2018. https://doi.org/10.1016/j.rser.2018.04.097.

[23] Soteris A Kalogirou. *Solar energy engineering: processes and systems*. Elsevier, 2023. https://doi.org/10.1016/C2021-0-02041-1.

[24] Riheb Mabrouk, Hassane Naji, Ali Cemal Benim, and Hacen Dhahri. A state of the art review on sensible and latent heat thermal energy storage processes in porous media: Mesoscopic simulation. *Applied Sciences*, 12(14):6995, 2022. https://doi.org/10.3390/app12146995.

[25] Luckywell Seyitini, Basim Belgasim, and Christopher Chintua Enweremadu. Solid state sensible heat storage technology for industrial applications–a review. *Journal of Energy Storage*, 62:106919, 2023. https://doi.org/10.1016/j.est.2023.106919.

[26] Ioan Sarbu and Calin Sebarchievici. A comprehensive review of thermal energy storage. *Sustainability*, 10(1):191, 2018. https://doi.org/10.3390/su10010191.

[27] Onder Kizilkan and Ibrahim Dincer. Borehole thermal energy storage system for heating applications: Thermodynamic performance assessment. *Energy Conversion and Management*, 90:53–61, 2015. https://doi.org/10.1016/j.enconman.2014.10.043.

[28] Lazaros Aresti, Paul Christodoulides, Gregoris P Panayiotou, and Georgios Florides. The potential of utilizing buildings' foundations as thermal energy storage (TES) units from solar plate collectors. *Energies*, 13(11):2695, 2020. https://doi.org/10.3390/en13112695.

[29] Emad Ali, Abdelhamid Ajbar, and Bilal Lamrani. Numerical investigation of thermal energy storage systems for collective heating of buildings. *Buildings*, 14(1):141, 2024. https://doi.org/10.3390/buildings14010141.

[30] Iñigo Ortega-Fernández and Javier Rodríguez-Aseguinolaza. Thermal energy storage for waste heat recovery in the steelworks: The case study of the reslag project. *Applied Energy*, 237:708–719, 2019. https://doi.org/10.1016/j.apenergy.2019.01.007.

[31] Andreas König-Haagen, Stephan Höhlein, and Dieter Brüggemann. Detailed exergetic analysis of a packed bed thermal energy storage unit in combination with an organic rankine cycle. *Applied thermal engineering*, 165:114583, 2020. https://doi.org/10.1016/j.applthermaleng.2019.114583.

[32] Hanne Kauko, Daniel Rohde, Brage Rugstad Knudsen, and Terje Sund-Olsen. Potential of thermal energy storage for a district heating system utilizing industrial waste heat. *Energies*, 13(15):3923, 2020. https://doi.org/10.3390/en13153923.

[33] G Zanganeh, A Pedretti, A Haselbacher, and Aldo Steinfeld. Design of packed bed thermal energy storage systems for high-temperature industrial process heat. *Applied energy*, 137:812–822, 2015. https://doi.org/10.1016/j.apenergy.2014.07.110.

[34] Daniel C Stack, Daniel Curtis, and Charles Forsberg. Performance of firebrick resistance-heated energy storage for industrial heat applications and round-trip electricity storage. *Applied Energy*, 242:782–796, 2019. https://doi.org/10.1016/j.apenergy.2019.03.100.

[35] Khadija El Alami, Mohamed Asbik, and Hassan Agalit. Identification of natural rocks as storage materials in thermal energy storage (TES) system of concentrated solar power (CSP) plants–A review. *Solar Energy Materials and Solar Cells*, 217:110599, 2020. https://doi.org/10.1016/j.solmat.2020.110599.

[36] Valentina A Salomoni, Carmelo E Majorana, Giuseppe M Giannuzzi, Adio Miliozzi, Rosa Di Maggio, Fabrizio Girardi, Domenico Mele, and Marco Lucentini. Thermal storage of sensible heat using concrete modules in solar power plants. *Solar Energy*, 103:303–315, 2014. https://doi.org/10.1016/j.solener.2014.02.022.

[37] Ulf Herrmann, Bruce Kelly, and Henry Price. Two-tank molten salt storage for parabolic trough solar power plants. *Energy*, 29(5-6):883–893, 2004. https://doi.org/10.1016/S0360-5442(03)00193-2.

[38] Gang Li. Sensible heat thermal storage energy and exergy performance evaluations. *Renewable and Sustainable Energy Reviews*, 53:897–923, 2016. https://doi.org/10.1016/j.rser.2015.09.006.

[39] Xi Zhang, Hossein Ameli, Zihang Dong, Andrea Vecchi, Alejandro Gallego-Schmid, Goran Strbac, and Adriano Sciacovelli. Values of latent heat and thermochemical energy storage technologies in low-carbon energy systems: Whole system approach. *J Energy Storage*, 50:104126, 2022. https://doi.org/10.1016/j.est.2022.104126.

[40] Matteo Morciano, Matteo Alberghini, Matteo Fasano, Mariella Almiento, Flaviana Calignano, Diego Manfredi, Pietro Asinari, and Eliodoro Chiavazzo. 3d printed lattice metal structures for enhanced heat transfer in latent heat storage systems. *Journal of Energy Storage*, 65:107350, 2023. https://doi.org/10.1016/j.est.2023.107350.

[41] Matteo Morciano, Matteo Fasano, Eliodoro Chiavazzo, and Luigi Mongibello. Trending applications of phase change materials in sustainable thermal engineering: An up-to-date review. *Energy Conversion and Management: X*, page 100862, 2025. https://doi.org/10.1016/j.ecmx.2024.100862.

[42] Mohamed Shameer Peer, Mario Cascetta, Luca Migliari, Mario Petrollese, et al. Nanofluids in thermal energy storage systems: A comprehensive review. *Energies*, 18(3), 2025. https://doi.org/10.3390/en18030707.

[43] Pedro Pardo, Alexandre Deydier, Zoé Anxionnaz-Minvielle, Sylvie Rougé, Michel Cabassud, and Patrick Cognet. A review on high temperature thermochemical heat energy storage. *Renewable and Sustainable Energy Reviews*, 32:591–610, 2014. https://doi.org/10.1016/j.rser.2013.12.014.

[44] Rebeca Salgado-Pizarro, A Calderón, Adela Svobodova-Sedlackova, AI Fernández, and Camila Barreneche. The relevance of thermochemical energy storage in the last two decades: the analysis of research evolution. *Journal of Energy Storage*, 51:104377, 2022. https://doi.org/10.1016/j.est.2022.104377.

[45] DS Jayathunga, HP Karunathilake, M Narayana, and S Witharana. Phase change material (PCM) candidates for latent heat thermal energy storage (LHTES) in concentrated solar power (CSP) based thermal applications-a review. *Renewable and Sustainable Energy Reviews*, 189:113904, 2024. https://doi.org/10.1016/j.rser.2023.113904.

[46] Sara Rostami, Masoud Afrand, Amin Shahsavar, M Sheikholeslami, Rasool Kalbasi, Saeed Aghakhani, Mostafa Safdari Shadloo, and Hakan F Oztop. A review of melting and freezing processes of pcm/nano-pcm and their application in energy storage. *Energy*, 211:118698, 2020. https://doi.org/10.1016/j.energy.2020.118698.

[47] FS Javadi, HSC Metselaar, and PJSE Ganesan. Performance improvement of solar thermal systems integrated with phase change materials (PCM), a review. *Solar Energy*, 206:330–352, 2020. https://doi.org/10.1016/j.solener.2020.05.106.

[48] Mingyang Sun, Tong Liu, Haonan Sha, Mulin Li, Tianze Liu, Xinlei Wang, Guijun Chen, Jiadian Wang, and Dongyue Jiang. A review on thermal energy storage with eutectic phase change materials: Fundamentals and applications. *Journal of Energy Storage*, 68:107713, 2023. https://doi.org/10.1016/j.est.2023.107713.

[49] Luigi Calabrese, Vincenza Brancato, Valeria Palomba, and Edoardo Proverbio. An experimental study on the corrosion sensitivity of metal alloys for usage in PCM thermal energy storages. *Renewable Energy*, 138:1018–1027, 2019. https://doi.org/10.1016/j.renene.2019.02.013.

[50] Shamseldin A Mohamed, Fahad A Al-Sulaiman, Nasiru I Ibrahim, Md Hasan Zahir, Amir Al-Ahmed, R Saidur, BS Yılbaş, and AZ Sahin. A review on current status and challenges of inorganic phase change materials for thermal energy storage systems. *Renewable and Sustainable Energy Reviews*, 70:1072–1089, 2017. https://doi.org/10.1016/j.rser.2016.12.012.

[51] Abhishek Anand, Muhamad Mansor, Kamal Sharma, Amritanshu Shukla, Atul Sharma, Md Irfanul Haque Siddiqui, Kishor Kumar Sadasivuni, Neeraj Priyadarshi, and Bhekisipho Twala. A comprehensive review on eutectic phase change materials: Development, thermophysical properties, thermal stability, reliability, and applications. *Alexandria Engineering Journal*, 112:254–280, 2025. https://doi.org/10.1016/j.aej.2024.10.054.

[52] Srikar Rao Chalivendula and Hariprasad Tarigonda. Recent advances in organic phase change materials for thermal energy storage: A review on sustainable development applications. *International Journal of Thermophysics*, 46(6):1–56, 2025. https://doi.org/10.1007/s10765-025-03559-9.

[53] Manish K Rathod and Jyotirmay Banerjee. Thermal stability of phase change materials used in latent heat energy storage systems: A review. *Renewable and sustainable energy reviews*, 18:246–258, 2013. https://doi.org/10.1016/j.rser.2012.10.022.

[54] Evangelos Bellos and Christos Tzivanidis. Investigation of a star flow insert in a parabolic trough solar collector. *Applied Energy*, 224:86–102, 2018. https://doi.org/10.1016/j.apenergy.2018.04.099.

[55] Gen Ou, Peng Liu, Zhichun Liu, and Wei Liu. Performance analyses and heat transfer optimization of parabolic trough receiver with a novel single conical strip insert. *Renewable Energy*, 199:335–350, 2022. https://doi.org/10.1016/j.renene.2022.08.131.

[56] Waleed Al-Aloosi, Yaser Alaiwi, and Hudhaifa Hamzah. Thermal performance analysis in a parabolic trough solar collector with a novel design of inserted fins. *Case Studies in Thermal Engineering*, 49:103378, 2023. https://doi.org/10.1016/j.csite.2023.103378.

[57] Evangelos Bellos, Christos Tzivanidis, and Kimon A Antonopoulos. A detailed working fluid investigation for solar parabolic trough collectors. *Applied Thermal Engineering*, 114:374–386, 2017. https://doi.org/10.1016/j.applthermaleng.2016.11.201.

[58] Jonathan Flesch, Luca Marocco, Andreas Fritsch, Klarissa Niedermeier, and Thomas Wetzel. Entropy generation minimization analysis of solar salt, sodium, and lead–bismuth eutectic as high temperature heat transfer fluids. *Journal of Heat Transfer*, 142(4):042103, 2020. https://doi.org/10.1115/1.4046302.

[59] Alberto Giaconia, Anna Chiara Tizzoni, Salvatore Sau, Natale Corsaro, Emiliana Mansi, Annarita Spadoni, and Tiziano Delise. Assessment and perspectives of heat transfer fluids for CSP applications. *Energies*, 14(22):7486, 2021. https://doi.org/10.3390/en14227486.

[60] Teresa Aguilar, Iván Carrillo-Berdugo, Rodrigo Alcantara, and Javier Navas. Enhanced thermophysical properties in spinel CuFe2O4-based nanofluids for concentrated solar power. *International Journal of Energy Research*, 46(4):4908–4918, 2022. https://doi.org/10.1002/er.7484.

[61] Y-R Galindo-Luna, Heriberto Sánchez-Mora, Gilberto Espinosa-Paredes, and E-G Espinosa-Martinez. Performance comparison of PTCs with nanoparticles in water and nanoparticle in thermal oil. *Case Studies in Thermal Engineering*, 50:103478, 2023. https://doi.org/10.1016/j.csite.2023.103478.

[62] Klaus Burlafinger, Andreas Vetter, and Christoph J Brabec. Maximizing concentrated solar power (CSP) plant overall efficiencies by using spectral selective absorbers at optimal operation temperatures. *Solar Energy*, 120:428–438, 2015. https://doi.org/10.1016/j.solener.2015.07.023.

[63] Mehdi Shokrnia, Mattia Cagnoli, Roberto Grena, Antonio D'Angelo, Michela Lanchi, and Roberto Zanino. Photo-thermal optimization of a parabolic trough collector with arrayed selective coatings. *Energies*, 17(13):3221, 2024. https://doi.org/10.3390/en17133221.

[64] Gabriella Rossi, Antonio D'Angelo, Claudia Diletto, Salvatore Esposito, Antonio Guglielmo, and Michela Lanchi. New spectrally selective coatings for CSP linear receivers operating in air at high temperature. *Applied Research*, 3(2):e202200117, 2024. https://doi.org/10.1002/appl.202200117.

[65] Pusci Wang, DY Liu, and C Xu. Numerical study of heat transfer enhancement in the receiver tube of direct steam generation with parabolic trough by inserting metal foams. *Applied energy*, 102:449–460, 2013. https://doi.org/10.1016/j.apenergy.2012.07.026.

[66] Aggrey Mwesigye, Tunde Bello-Ochende, and Josua P Meyer. Heat transfer and thermodynamic performance of a parabolic trough receiver with centrally placed perforated plate inserts. *Applied energy*, 136:989–1003, 2014. https://doi.org/10.1016/j.apenergy.2014.03.037.

[67] Sehwa Lim, Yongheack Kang, Hyunjin Lee, and Seungwon Shin. Design optimization of a tubular solar receiver with a porous medium. *Applied Thermal Engineering*, 62(2):566–572, 2014. https://doi.org/10.1016/j.applthermaleng.2013.10.025.

[68] Milad Tajik Jamal-Abad, Seyfollah Saedodin, and Mohammad Aminy. Experimental investigation on a solar parabolic trough collector for absorber tube filled with porous media. *Renewable Energy*, 107:156–163, 2017. https://doi.org/10.1016/j.renene.2017.02.004.

[69] Mohammad Mahdi Heyhat and Murtadha Zahi Khattar. On the effect of different placement schemes of metal foam as volumetric absorber on the thermal performance of a direct absorption parabolic trough solar collector. *Energy*, 266:126428, 2023. https://doi.org/10.1016/j.energy.2022.126428.

[70] Laura Savoldi, Andrea Allio, Antonio Bonvento, Marco Cantone, and Jesus Fernandez Reche. Experimental and numerical investigation of a porous receiver equipped with Raschig Rings for CSP applications. *Solar Energy*, 212:309–325, 2020. https://doi.org/10.1016/j.solener.2020.11.006.

[71] Hossein Ebadi, Antonio Cammi, Nima Fathi, and Laura Savoldi. Pore-scale simulation of a tubular solar absorber partially filled with raschig ring porous medium for efficiency enhancement purposes. In *ASME Power Conference*, volume 87172, page V001T05A007. American Society of Mechanical Engineers, 2023. https://doi.org/10.1115/POWER2023-108768.

[72] Hossein Ebadi, Antonio Cammi, Eleonora Gajetti, and Laura Savoldi. Development, verification and experimental validation of a 3D numerical model for tubular solar receivers equipped with Raschig Ring porous inserts. *Solar Energy*, 267:112236, 2024. https://doi.org/10.1016/j.solener.2023.112236.

[73] H. H. Gerke and M. T. Van Genuchten. A dual-porosity model for simulating the preferential movement of water and solutes in structured porous media. *Water resources research*, 29(2):305–319, 1993. https://doi.org/10.1029/92WR02339.

[74] J Tian, T Kim, TJ Lu, HP Hodson, DT Queheillalt, DJ Sypeck, and HNG Wadley. The effects of topology upon fluid-flow and heat-transfer within cellular copper structures. *International Journal of Heat and Mass Transfer*, 47(14-16):3171–3186, 2004. https://doi.org/10.1016/j.ijheatmasstransfer.2004.02.010.

[75] J Tian, TJ Lu, HP Hodson, DT Queheillalt, and HNG Wadley. Cross flow heat exchange of textile cellular metal core sandwich panels. *International journal of heat and mass transfer*, 50(13-14):2521–2536, 2007. https://doi.org/10.1016/j.ijheatmasstransfer.2006.11.042.

[76] Jin Yao Ho, Kai Choong Leong, and Teck Neng Wong. Additively-manufactured metallic porous lattice heat exchangers for air-side heat transfer enhancement. *International Journal of Heat and Mass Transfer*, 150:119262, 2020. https://doi.org/10.1016/j.ijheatmasstransfer.2019.119262.

[77] Uzair Sajjad, Tauseef-ur Rehman, Mubasher Ali, Cheol Woo Park, and Wei-Mon Yan. Manufacturing and potential applications of lattice structures in thermal systems: A comprehensive review of recent advances. *International Journal of Heat and Mass Transfer*, 198:123352, 2022. https://doi.org/10.1016/j.ijheatmasstransfer.2022.123352.

[78] Inderjot Kaur and Prashant Singh. Critical evaluation of additively manufactured metal lattices for viability in advanced heat exchangers. *International Journal of Heat and Mass Transfer*, 168:120858, 2021. https://doi.org/10.1016/j.ijheatmasstransfer.2020.120858.

[79] Eric A Lord and Alan L Mackay. Periodic minimal surfaces of cubic symmetry. *Current Science*, pages 346–362, 2003. http://www.jstor.org/stable/24108665.

[80] Seo-Hyeon Oh, Chan-Hee An, Bomin Seo, Jungwoo Kim, Chang Yong Park, and Keun Park. Functional morphology change of tpms structures for design and additive manufacturing of compact heat exchangers. *Additive Manufacturing*, 76:103778, 2023. https://doi.org/10.1016/j.addma.2023.103778.

[81] Guanghan Yan, Mingrui Sun, Yiqiang Liang, Shuai Li, Zhaoda Zhang, Xiaokai Zhang, Yongchen Song, Yu Liu, and Jiafei Zhao. Simulation and experimental study on flow and heat transfer performance of sheet-network and solid-network disturbance structures based on triply periodic minimal surface. *International Journal of Heat and Mass Transfer*, 219:124905, 2024. https://doi.org/10.1016/j.ijheatmasstransfer.2023.124905.

[82] Mohamed G Gado, Shinichi Ookawara, and Hamdy Hassan. Utilization of triply periodic minimal surfaces for performance enhancement of adsorption

cooling systems: Computational fluid dynamics analysis. *Energy Conversion and Management*, 277:116657, 2023. https://doi.org/10.1016/j.enconman.2023.116657.

[83] Wei Tang, Hua Zhou, Yun Zeng, Minglei Yan, Chenglu Jiang, Ping Yang, Qing Li, Zhida Li, Junheng Fu, Yi Huang, et al. Analysis on the convective heat transfer process and performance evaluation of Triply Periodic Minimal Surface (TPMS) based on Diamond, Gyroid and Iwp. *International Journal of Heat and Mass Transfer*, 201:123642, 2023. https://doi.org/10.1016/j.ijheatmasstransfer.2022.123642.

[84] Dong Liang, Chenwei Shi, Weihong Li, Wei Chen, and Minking K Chyu. Design, flow characteristics and performance evaluation of bioinspired heat exchangers based on triply periodic minimal surfaces. *International Journal of Heat and Mass Transfer*, 201:123620, 2023. https://doi.org/10.1016/j.ijheatmasstransfer.2022.123620.

[85] Weihong Li, Guopeng Yu, and Zhibin Yu. Bioinspired heat exchangers based on triply periodic minimal surfaces for supercritical co2 cycles. *Applied Thermal Engineering*, 179:115686, 2020. https://doi.org/10.1016/j.applthermaleng.2020.115686.

[86] Mohamad Khalil, Mohamed I Hassan Ali, Kamran A Khan, and Rashid Abu Al-Rub. Forced convection heat transfer in heat sinks with topologies based on triply periodic minimal surfaces. *Case Studies in Thermal Engineering*, 38:102313, 2022. https://doi.org/10.1016/j.csite.2022.102313.

[87] Mohamad Modrek, Asha Viswanath, Kamran A Khan, Mohamed I Hassan Ali, and Rashid K Abu Al-Rub. An optimization case study to design additively manufacturable porous heat sinks based on triply periodic minimal surface (TPMS) lattices. *Case Studies in Thermal Engineering*, 36:102161, 2022. https://doi.org/10.1016/j.csite.2022.102161.

[88] Guanghan Yan, Mingrui Sun, Zhaoda Zhang, Yiqiang Liang, Nan Jiang, Xiaodong Pang, Yongchen Song, Yu Liu, and Jiafei Zhao. Experimental study on flow and heat transfer performance of triply periodic minimal surface structures and their hybrid form as disturbance structure. *International Communications in Heat and Mass Transfer*, 147:106942, 2023. https://doi.org/10.1016/j.icheatmasstransfer.2023.106942.

[89] Mohamad Modrek, Asha Viswanath, Kamran A Khan, Mohamed I Hassan Ali, and Rashid K Abu Al-Rub. Multi-objective topology optimization of passive heat sinks including self-weight based on triply periodic minimal surface lattices. *Case Studies in Thermal Engineering*, 42:102684, 2023. https://doi.org/10.1016/j.csite.2022.10268.

[90] Eleonora Gajetti, Massimiliano Bonesso, Alessandro Bruschi, Francesco Fanale, Saul Garavaglia, Gustavo Granucci, Alessandro Moro, Adriano Pepato, Afra Romano, and Laura Savoldi. A new efficient mirror cooling for

the transmission line of fusion reactor ECH systems based on triply periodic minimal surfaces. *IEEE Transactions on Plasma Science*, 52(9):3765–3771, 2024. https://doi.org/10.1109/TPS.2024.3383275.

[91] Gerard L Vignoles, Denis Rochais, and Sylvain Chupin. Computation of the conducto-radiative effective heat conductivity of porous media defined by triply periodic minimal surfaces. *International Journal of Thermal Sciences*, 159:106598, 2021. https://doi.org/10.1016/j.ijthermalsci.2020.106598.

[92] Zekai Mu, Xianglei Liu, Chao Song, Nan Sun, Cheng Tian, and Yimin Xuan. Direct solar-driven thermochemical co2-to-fuel conversion with efficiency over 39% employing hierarchical triply periodic minimal surfaces biomimetic foam reactors. *Next Energy*, 1(3):100051, 2023. https://doi.org/10.1016/j.nxener.2023.100051.

[93] Nurten Şahan, Magali Fois, and Halime Paksoy. Improving thermal conductivity phase change materials—a study of paraffin nanomagnetite composites. *Solar Energy Materials and Solar Cells*, 137:61–67, 2015. https://doi.org/10.1016/j.solmat.2015.01.027.

[94] Farid Bahiraei, Amir Fartaj, and Gholam-Abbas Nazri. Experimental and numerical investigation on the performance of carbon-based nanoenhanced phase change materials for thermal management applications. *Energy Conversion and Management*, 153:115–128, 2017. https://doi.org/10.1016/j.enconman.2017.09.065.

[95] Kin Yuen Leong, Mohd Rosdzimin Abdul Rahman, and Balamurugan A Gurunathan. Nano-enhanced phase change materials: A review of thermophysical properties, applications and challenges. *Journal of Energy Storage*, 21:18–31, 2019. https://doi.org/10.1016/j.est.2018.11.008.

[96] Alessandro Ribezzo, Matteo Morciano, Gabriel Zsembinszki, Sara Risco Amigó, Saranprabhu Mani Kala, Emiliano Borri, Luca Bergamasco, Matteo Fasano, Eliodoro Chiavazzo, Cristina Prieto, et al. Enhancement of heat transfer through the incorporation of copper metal wool in latent heat thermal energy storage systems. *Renewable Energy*, 231:120888, 2024. https://doi.org/10.1016/j.renene.2024.120888.

[97] Waqar Ahmed, Abid Hussain, Hanzla Shahid, Imran Ali, and Hafiz Muhammad Ali. Experimental study on heat storage properties comparison of paraffin/metal foams phase change material composites. *Journal of Thermal Science*, 33(2):469–478, 2024. https://doi.org/10.1007/s11630-023-1828-5.

[98] Mohamad Aramesh and Bahman Shabani. Metal foams application to enhance the thermal performance of phase change materials: A review of experimental studies to understand the mechanisms. *Journal of Energy Storage*, 50:104650, 2022. https://doi.org/10.1016/j.est.2022.104650.

[99] Kasra Ghasemi, Syeda Tasnim, and Shohel Mahmud. PCM, nano/microencapsulation and slurries: A review of fundamentals, categories, fabrication, numerical models and applications. *Sustainable Energy Technologies and Assessments*, 52:102084, 2022. https://doi.org/10.1016/j.seta.2022.102084.

[100] David Vérez, Emiliano Borri, Alicia Crespo, Boniface Dominick Mselle, Álvaro de Gracia, Gabriel Zsembinszki, and Luisa F Cabeza. Experimental study on two pcm macro-encapsulation designs in a thermal energy storage tank. *Applied Sciences*, 11(13):6171, 2021. https://doi.org/10.3390/app11136171.

[101] AliReza Rezaeishaker, Ali Ahmadpour, and MohammadReza Hajmohammadi. A novel design for macro encapsulation of phase change materials for energy storage systems. *Journal of Energy Storage*, 113:115631, 2025. https://doi.org/10.1016/j.est.2025.115631.

[102] Tingwei Zhang, Gaofeng Lu, and Xiaoqiang Zhai. Design and experimental investigation of a novel thermal energy storage unit with phase change material. *Energy Reports*, 7:1818–1827, 2021. https://doi.org/10.1016/j.egyr.2021.03.029.

[103] Aurang Zaib, Abdur Rehman Mazhar, Shahid Aziz, Tariq Talha, and Dong-Won Jung. Heat transfer augmentation using duplex and triplex tube phase change material (PCM) heat exchanger configurations. *Energies*, 16(10):4037, 2023. https://doi.org/10.3390/en16104037.

[104] Xianzhe Zhang, Wenbin Cui, Shanyu Yang, Zhilu Wu, Ziyu Xiong, and Sixiang Zhang. Influence of inclined non-uniform fins on the melting of phase change materials under constant-power heating condition. *Energies*, 18(7):1733, 2025. https://doi.org/10.3390/en18071733.

[105] Zijian He, Hongting Ma, and Shilei Lu. Design and experimental investigation of topology-optimized fin structures for enhanced heat transfer in latent heat thermal energy storage units. *Journal of Energy Storage*, 80:110272, 2024. https://doi.org/10.1016/j.est.2023.110272.

[106] Alberto Pizzolato, Ashesh Sharma, Kurt Maute, Adriano Sciacovelli, and Vittorio Verda. Topology optimization for heat transfer enhancement in latent heat thermal energy storage. *International Journal of Heat and Mass Transfer*, 113:875–888, 2017. https://doi.org/10.1016/j.ijheatmasstransfer.2017.05.098.

[107] Jun Wu, Ole Sigmund, and Jeroen P Groen. Topology optimization of multi-scale structures: a review. *Structural and Multidisciplinary Optimization*, 63:1455–1480, 2021. https://doi.org/10.1007/s00158-021-02881-8.

[108] Martin Philip Bendsøe and Noboru Kikuchi. Generating optimal topologies in structural design using a homogenization method. *Computer methods in applied mechanics and engineering*, 71(2):197–224, 1988. https://doi.org/10.1016/0045-7825(88)90086-2.

[109] Joe Alexandersen, Ole Sigmund, Knud Erik Meyer, and Boyan Stefanov Lazarov. Design of passive coolers for light-emitting diode lamps using topology optimisation. *International Journal of Heat and Mass Transfer*, 122:138–149, 2018. https://doi.org/10.1016/j.ijheatmasstransfer.2018.01.103.

[110] David Martínez-Maradiaga, Alberto Damonte, Alessandro Manzo, Jan HK Haertel, and Kurt Engelbrecht. Design and testing of topology optimized heat sinks for a tablet. *International Journal of Heat and Mass Transfer*, 142:118429, 2019. https://doi.org/10.1016/j.ijheatmasstransfer.2019.07.079.

[111] V Subramaniam, T Dbouk, and J-L Harion. Topology optimization of conductive heat transfer devices: an experimental investigation. *Applied Thermal Engineering*, 131:390–411, 2018. https://doi.org/10.1016/j.applthermaleng.2017.12.026.

[112] Alberto Pizzolato, Ashesh Sharma, Kurt Maute, Adriano Sciacovelli, and Vittorio Verda. Design of effective fins for fast pcm melting and solidification in shell-and-tube latent heat thermal energy storage through topology optimization. *Applied Energy*, 208:210–227, 2017. https://doi.org/10.1016/j.apenergy.2017.10.050.

[113] Imad Ait Laasri, Zakaria Elmaazouzi, Abdelkader Outzourhit, and Mohamed Oualid Mghazli. Investigation of different topology-optimized fin structures in a cylindrical latent heat thermal energy storage unit. *Thermal Science and Engineering Progress*, 33:101372, 2022. https://doi.org/10.1016/j.tsep.2022.101372.

[114] Xinyu Zhang, Xiaohong Yang, Yannan Zhang, Jiakun Xu, and Xiao Guo. Phase change heat transfer enhancement based on topology optimization of fin structure. *International Journal of Heat and Mass Transfer*, 214:124402, 2023. https://doi.org/10.1016/j.ijheatmasstransfer.2023.124402.

[115] Maiqiang Zhou, N Pagaldipti, HL Thomas, and YK Shyy. An integrated approach to topology, sizing, and shape optimization. *Structural and Multidisciplinary Optimization*, 26(5):308–317, 2004. https://doi.org/10.1007/s00158-003-0351-2.

[116] COMSOL Multiphysics®. *Optimization Module User's Guide*. Stockholm, Sweden, version 6.3 edition, 2024. https://doc.comsol.com/6.3/doc/com.comsol.help.opt/OptimizationModuleUsersGuide.pdf.

[117] J. A. Nelder and R. Mead. A simplex method for function minimization. *The Computer Journal*, 7(4):308–313, 1965. https://doi.org/10.1093/comjnl/7.4.308.

[118] Michael JD Powell et al. The BOBYQA algorithm for bound constrained optimization without derivatives. *Cambridge NA Report NA2009/06, University of Cambridge, Cambridge*, 26(26-46):1, 2009. https://www.damtp.cam.ac.uk/user/na/NA_papers/NA2009_06.pdf.

[119] Michael JD Powell. A direct search optimization method that models the objective and constraint functions by linear interpolation. In *Advances in optimization and numerical analysis*, pages 51–67. Springer, 1994. https://doi.org/10.1007/978-94-015-8330-5.

[120] Donald R Jones, Matthias Schonlau, and William J Welch. Efficient global optimization of expensive black-box functions. *Journal of Global optimization*, 13(4):455–492, 1998. https://doi.org/10.1023/A:1008306431147.

[121] Philip E Gill, Walter Murray, and Michael A Saunders. SNOPT: An SQP algorithm for large-scale constrained optimization. *SIAM review*, 47(1):99–131, 2005. https://doi.org/10.1137/S0036144504446096.

[122] Andreas Wächter and Lorenz T Biegler. On the implementation of an interior-point filter line-search algorithm for large-scale nonlinear programming. *Mathematical programming*, 106(1):25–57, 2006. https://doi.org/10.1007/s10107-004-0559-y.

[123] Krister Svanberg. The method of moving asymptotes—a new method for structural optimization. *International journal for numerical methods in engineering*, 24(2):359–373, 1987. https://doi.org/10.1002/nme.1620240207.

[124] Ole Sigmund and Kurt Maute. Topology optimization approaches: A comparative review. *Structural and multidisciplinary optimization*, 48(6):1031–1055, 2013. https://doi.org/10.1007/s00158-013-0978-6.

[125] Martin P Bendsøe. Optimal shape design as a material distribution problem. *Structural optimization*, 1(4):193–202, 1989. https://doi.org/10.1007/BF01650949.

[126] Ming Zhou and George IN Rozvany. The COC algorithm, Part II: Topological, geometrical and generalized shape optimization. *Computer methods in applied mechanics and engineering*, 89(1-3):309–336, 1991. https://doi.org/10.1016/0045-7825(91)90046-9.

[127] HP Mlejnek. Some aspects of the genesis of structures. *Structural optimization*, 5(1):64–69, 1992. https://doi.org/10.1007/BF01744697.

[128] Grégoire Allaire, François Jouve, and Anca-Maria Toader. A level-set method for shape optimization. *Comptes rendus. Mathématique*, 334(12):1125–1130, 2002. https://doi.org/10.1016/S1631-073X(02)02412-3.

[129] Grégoire Allaire, François Jouve, and Anca-Maria Toader. Structural optimization using sensitivity analysis and a level-set method. *Journal of computational physics*, 194(1):363–393, 2004. https://doi.org/10.1016/j.jcp.2003.09.032.

[130] Michael Yu Wang, Xiaoming Wang, and Dongming Guo. A level set method for structural topology optimization. *Computer methods in applied mechanics and engineering*, 192(1-2):227–246, 2003. https://doi.org/doi.org/10.1016/S0045-7825(02)00559-5.

[131] Jan Sokolowski and Antoni Zochowski. Topological derivative in shape optimization. In *Encyclopedia of Optimization*, pages 3908–3918. Springer, 2008. https://doi.org/doi.org/10.1007/978-0-387-74759-0_682.

[132] Blaise Bourdin and Antonin Chambolle. Design-dependent loads in topology optimization. *ESAIM: Control, Optimisation and Calculus of Variations*, 9:19–48, 2003. https://doi.org/doi.org/10.1051/cocv:2002070.

[133] Yi Min Xie and Grant P Steven. A simple evolutionary procedure for structural optimization. *Computers & structures*, 49(5):885–896, 1993. https://doi.org/doi.org/10.1016/0045-7949(93)90035-C.

[134] Behrooz Hassani and E Hinton. A review of homogenization and topology opimization II—analytical and numerical solution of homogenization equations. *Computers & structures*, 69(6):719–738, 1998. https://doi.org/10.1016/S0045-7949(98)00132-1.

[135] Martin P Bendsøe and Ole Sigmund. Material interpolation schemes in topology optimization. *Archive of applied mechanics*, 69(9):635–654, 1999. https://doi.org/doi.org/10.1007/s004190050248.

[136] Ole Sigmund. On the usefulness of non-gradient approaches in topology optimization. *Structural and Multidisciplinary Optimization*, 43(5):589–596, 2011. https://doi.org/10.1007/s00158-011-0638-7.

[137] Martin P.. Bendsøe and Ole Sigmund. *Topology optimization: theory, methods, and applications*. Springer Berlin, Germany, 2004. https://doi.org/10.1007/978-3-662-05086-6.

[138] Krister Svanberg. MMA and GCMMA-two methods for nonlinear optimization. KTH, Stockholm, Sweden, 2007. https://people.kth.se/~krille/mmagcmma.pdf.

[139] Alberto Pizzolato et al. *Topology optimization for energy problems*. PhD thesis, Politecnico di Torino, Department of Energy, 2018.

[140] Christian Zillober. A globally convergent version of the method of moving asymptotes. *Structural optimization*, 6(3):166–174, 1993. https://doi.org/10.1007/BF01743509.

[141] Susana Rojas-Labanda and Mathias Stolpe. Benchmarking optimization solvers for structural topology optimization. *Structural and Multidisciplinary Optimization*, 52(3):527–547, 2015. https://doi.org/10.1007/s00158-015-1250-z.

[142] Kurt Maute, Melike Nikbay, and Charbel Farhat. Sensitivity analysis and design optimization of three-dimensional non-linear aeroelastic systems by the adjoint method. *International Journal for Numerical Methods in Engineering*, 56(6):911–933, 2003. https://doi.org/10.1002/nme.599.

[143] Sajjad Zargham, Thomas Arthur Ward, Rahizar Ramli, and Irfan Anjum Badruddin. Topology optimization: a review for structural designs under vibration problems. *Structural and Multidisciplinary Optimization*, 53(6):1157–1177, 2016. https://doi.org/10.1007/s00158-015-1370-5.

[144] Daniel Yago, Juan Cante, Oriol Lloberas-Valls, and Javier Oliver. Topology optimization methods for 3D structural problems: a comparative study. *Archives of Computational Methods in Engineering*, 29(3):1525–1567, 2022. https://doi.org/10.1007/s11831-021-09626-2.

[145] A Rietz. Sufficiency of a finite exponent in SIMP (power law) methods. *Structural and Multidisciplinary Optimization*, 21(2):159–163, 2001. https://doi.org/10.1007/s001580050180.

[146] Ole Sigmund and Joakim Petersson. Numerical instabilities in topology optimization: a survey on procedures dealing with checkerboards, mesh-dependencies and local minima. *Structural optimization*, 16(1):68–75, 1998. https://doi.org/10.1007/BF01214002.

[147] Alejandro Diaz and Ole Sigmund. Checkerboard patterns in layout optimization. *Structural optimization*, 10(1):40–45, 1995. https://doi.org/10.1007/BF01743693.

[148] Chandrashekhar S Jog and Robert B Haber. Stability of finite element models for distributed-parameter optimization and topology design. *Computer methods in applied mechanics and engineering*, 130(3-4):203–226, 1996. https://doi.org/10.1016/0045-7825(95)00928-0.

[149] Ole Sigmund. Morphology-based black and white filters for topology optimization. *Structural and Multidisciplinary Optimization*, 33(4):401–424, 2007. https://doi.org/10.1007/s00158-006-0087-x.

[150] Gang-Won Jang, Je Hyun Jeong, Yoon Young Kim, Dongwoo Sheen, Chunjae Park, and Myoung-Nyoun Kim. Checkerboard-free topology optimization using non-conforming finite elements. *International Journal for Numerical Methods in Engineering*, 57(12):1717–1735, 2003. https://doi.org/10.1002/nme.738.

[151] Thomas A Poulsen. A simple scheme to prevent checkerboard patterns and one-node connected hinges in topology optimization. *Structural and Multidisciplinary Optimization*, 24(5):396–399, 2002. https://doi.org/10.1007/s00158-002-0251-x.

[152] Luigi Ambrosio and Giuseppe Buttazzo. An optimal design problem with perimeter penalization. *Calculus of variations and partial differential equations*, 1(1):55–69, 1993. https://doi.org/10.1007/BF02163264.

[153] Robert B Haber, Chandrashekhar S Jog, and Martin P Bendsøe. A new approach to variable-topology shape design using a constraint on perimeter. *Structural optimization*, 11(1):1–12, 1996. https://doi.org/10.1007/BF01279647.

[154] Tyler E Bruns and Daniel A Tortorelli. Topology optimization of non-linear elastic structures and compliant mechanisms. *Computer methods in applied mechanics and engineering*, 190(26-27):3443–3459, 2001. https://doi.org/10.1016/S0045-7825(00)00278-4.

[155] Robert B Haber, Chandrashekhar S Jog, and Martin P Bendsøe. Variable-topology shape optimization with a control on perimeter. In *International Design Engineering Technical Conferences and Computers and Information in Engineering Conference*, volume 97683, pages 261–272. American Society of Mechanical Engineers, 1994. https://doi.org/10.1115/DETC1994-0136.

[156] Thomas Borrvall. Topology optimization of elastic continua using restriction. *Archives of Computational Methods in Engineering*, 8(4):351–385, 2001. https://doi.org/10.1007/BF02743737.

[157] M Zhou, YK Shyy, and HL Thomas. Checkerboard and minimum member size control in topology optimization. *Structural and Multidisciplinary Optimization*, 21(2):152–158, 2001. https://doi.org/10.1007/s001580050179.

[158] Thomas Borrvall and Joakim Petersson. Topology optimization using regularized intermediate density control. *Computer Methods in Applied Mechanics and Engineering*, 190(37-38):4911–4928, 2001. https://doi.org/10.1016/S0045-7825(00)00356-X.

[159] Thomas A Poulsen. A new scheme for imposing a minimum length scale in topology optimization. *International Journal for Numerical Methods in Engineering*, 57(6):741–760, 2003. https://doi.org/10.1002/nme.694.

[160] Thomas A Poulsen. Topology optimization in wavelet space. *International Journal for Numerical Methods in Engineering*, 53(3):567–582, 2002. https://doi.org/10.1002/nme.285.

[161] Blaise Bourdin. Filters in topology optimization. *International journal for numerical methods in engineering*, 50(9):2143–2158, 2001. https://doi.org/10.1002/nme.116.

[162] Boyan Stefanov Lazarov and Ole Sigmund. Filters in topology optimization based on helmholtz-type differential equations. *International journal for numerical methods in engineering*, 86(6):765–781, 2011. https://doi.org/10.1002/nme.3072.

[163] Erich Zauderer. *Partial differential equations of applied mathematics*. John Wiley & Sons, 2011.

[164] Atsushi Kawamoto, Tadayoshi Matsumori, Shintaro Yamasaki, Tsuyoshi Nomura, Tsuguo Kondoh, and Shinji Nishiwaki. Heaviside projection based topology optimization by a PDE-filtered scalar function. *Structural and Multidisciplinary Optimization*, 44(1):19–24, 2011. https://doi.org/10.1007/s00158-010-0562-2.

[165] James K Guest, Jean H Prévost, and Ted Belytschko. Achieving minimum length scale in topology optimization using nodal design variables and projection functions. *International journal for numerical methods in engineering*, 61(2):238–254, 2004. https://doi.org/10.1002/nme.1064.

[166] Fengwen Wang, Boyan Stefanov Lazarov, and Ole Sigmund. On projection methods, convergence and robust formulations in topology optimization. *Structural and multidisciplinary optimization*, 43(6):767–784, 2011. https://doi.org/10.1007/s00158-010-0602-y.

[167] Shengli Xu, Yuanwu Cai, and Gengdong Cheng. Volume preserving nonlinear density filter based on heaviside functions. *Structural and Multidisciplinary Optimization*, 41(4):495–505, 2010. https://doi.org/10.1007/s00158-009-0452-7.

[168] Oraib Al-Ketan and Rashid K Abu Al-Rub. Multifunctional mechanical metamaterials based on triply periodic minimal surface lattices. *Advanced Engineering Materials*, 21(10):1900524, 2019. https://doi.org/10.1002/adem.201900524.

[169] Fenglei Li, Jiakang Gan, Long Zhang, Hailun Tan, Eric Li, and Bing Li. Enhancing impact resistance of hybrid structures designed with triply periodic minimal surfaces. *Composites Science and Technology*, 245:110365, 2024. https://doi.org/10.1016/j.compscitech.2023.110365.

[170] Derya Karaman and Hojjat Ghahramanzadeh Asl. The effects of sheet and network solid structures of similar TPMS scaffold architectures on permeability, wall shear stress, and velocity: A CFD analysis. *Medical Engineering and Physics*, 118:104024, 2023. https://doi.org/10.1016/j.medengphy.2023.104024.

[171] Oraib Al-Ketan and Rashid K Abu Al-Rub. MSLattice: A free software for generating uniform and graded lattices based on triply periodic minimal surfaces. *Material Design & Processing Communications*, 3(6):e205, 2021. https://doi.org/10.1002/mdp2.205.

[172] Oraib Al-Ketan, Dong-Wook Lee, Reza Rowshan, and Rashid K Abu Al-Rub. Functionally graded and multi-morphology sheet tpms lattices: Design, manufacturing, and mechanical properties. *Journal of the mechanical behavior of biomedical materials*, 102:103520, 2020. https://doi.org/10.1016/j.jmbbm.2019.103520.

[173] Abdallah Barakat and BeiBei Sun. Enhanced convective heat transfer in new triply periodic minimal surface structures: Numerical and experimental investigation. *International Journal of Heat and Mass Transfer*, 227:125538, 2024. https://doi.org/10.1016/j.ijheatmasstransfer.2024.125538.

[174] Jack Walles. What equations are used to create the TPMS types? nTopSupport, May 2026. https://support.ntop.com/hc/en-us/articles/360053267814-What-equations-are-used-to-create-the-TPMS-types.

[175] Adriano Sciacovelli, Flavio Gagliardi, and Vittorio Verda. Maximization of performance of a PCM latent heat storage system with innovative fins. *Applied Energy*, 137:707–715, 2015. https://doi.org/10.1016/j.apenergy.2014.07.015.

[176] Ran Zheng, Bing Yi, Xiang Peng, and Gil-Ho Yoon. An efficient code for the multi-material topology optimization of 2D/3D continuum structures written in MATLAB. *Applied Sciences*, 14(2):657, 2024. https://doi.org/10.3390/app14020657.

[177] Biruk Agegnehu, Karl Liebezeit, Matteo Fasano, Matteo Morciano, and Eliodoro Chiavazzo. Dynamic pcm for high-performance latent thermal energy storage: A numerical and parametric study. *International Communications in Heat and Mass Transfer*, 167:109277, 2025. https://doi.org/10.1016/j.icheatmasstransfer.2025.109277.

[178] Indra Kumar Lokhande and Nishant Tiwari. A numerical investigation of novel segmented pcm blocks filled with different phase change material cooling for lithium-ion battery. *Applied Thermal Engineering*, 252:123673, 2024. https://doi.org/10.1016/j.applthermaleng.2024.123673.

[179] Mariam Jadal, Jérôme Soto, Nicolas Boyard, and Didier Delaunay. Experimental determination of crystallization kinetic model of CENG-PCM composite material. Validation at macro and meso scales. *Thermal Science and Engineering Progress*, 33:101336, 2022. https://doi.org/10.1016/j.tsep.2022.101336.

[180] Soteris A Kalogirou. Solar thermal collectors and applications. *Progress in energy and combustion science*, 30(3):231–295, 2004. https://doi.org/10.1016/j.pecs.2004.02.001.

[181] Marco Binotti, Guangdong Zhu, Allison Gray, Giampaolo Manzolini, and Paolo Silva. Geometric analysis of three-dimensional effects of parabolic trough collectors. *Solar Energy*, 88:88–96, 2013. https://doi.org/10.1016/j.solener.2012.10.025.

[182] nTop Inc. nTop. https://www.ntop.com/, 2024. Release 5.1.

[183] Siemens Industries Digital Software. Simcenter STAR-CCM+, 2022. Version 2022.1.1, Siemens.

[184] Thibaut De Terris, Thierry Baffie, and Celine Ribiere. Additive manufacturing of pure copper: a review and comparison of physical, microstructural, and mechanical properties of samples manufactured with Laser-Powder Bed Fusion (L-PBF), Electron Beam Melting (EBM) and Metal Fused Deposition Modelling (MFDM) technologies. *International Journal of Material Forming*, 16(4):32, 2023. https://doi.org/10.1007/s12289-023-01755-2.

[185] Khashayar Morshed-Behbahani, Ahmed Aliyu, Donald Paul Bishop, and Ali Nasiri. Additive manufacturing of copper-based alloys for high-temperature aerospace applications: A review. *Materials Today Communications*, 38:108395, 2024. https://doi.org/10.1016/j.mtcomm.2024.108395.

[186] Joseph R. Davis. *Metals Handbook Desk Edition (2nd Edition)*. ASM International, 1998. https://doi.org/10.31399/asm.hb.mhde2.9781627081993.

[187] Xiaoxin Zhang, Yingli Yuan, Sanqing Zhao, Jun Zhang, and Qingzhi Yan. Microstructure stability, softening temperature and strengthening mechanism of pure copper, CuCrZr and Cu-Al2O3 up to 1000°C. *Nuclear Materials and Energy*, 30:101123, 2022. https://doi.org/10.1007/s11831-021-09626-2.

[188] Dow Chemicals. Properties of SYLTHERM™ 800 Stabilized Heat Transfer Fluid, November 2001. https://www.dow.com/en-us/pdp.syltherm-800-stabilized-heat-transfer-fluid.39260z.html?productCatalogFlag=1#properties.

[189] Jaisree Iyer, Thomas Moore, Du Nguyen, Pratanu Roy, and Joshuah Stolaroff. Heat transfer and pressure drop characteristics of heat exchangers based on triply periodic minimal and periodic nodal surfaces. *Applied Thermal Engineering*, 209:118192, 2022. https://doi.org/10.1016/j.applthermaleng.2022.118192.

[190] André Gonçalves Pereira Passos. *Laminar flow and heat transfer in triply periodic minimal surfaces*. PhD thesis, Lund University: Lund, Sweden, 2020.

[191] Benjamin W Reynolds, Conan J Fee, Ken R Morison, and Daniel J Holland. Characterisation of heat transfer within 3D printed TPMS heat exchangers. *International Journal of Heat and Mass Transfer*, 212:124264, 2023. https://doi.org/10.1016/j.ijheatmasstransfer.2023.124264.

[192] Efstathios Kaloudis, E Papanicolaou, and VJRE Belessiotis. Numerical simulations of a parabolic trough solar collector with nanofluid using a two-phase model. *Renewable Energy*, 97:218–229, 2016. https://doi.org/10.1016/j.renene.2016.05.046.

[193] Mukundjee Pandey, Biranchi Narayana Padhi, and Ipsita Mishra. Numerical simulation of solar parabolic trough collector with viscous dissipation in slits of arc-plug insertion. *Solar Energy*, 230:810–824, 2021. https://doi.org/10.1016/j.solener.2021.11.008.

[194] K Arshad Ahmed and E Natarajan. Thermal performance enhancement in a parabolic trough receiver tube with internal toroidal rings: A numerical investigation. *Applied Thermal Engineering*, 162:114224, 2019. https://doi.org/10.1016/j.applthermaleng.2019.114224.

[195] Evangelos Bellos and Christos Tzivanidis. Thermal analysis of parabolic trough collector operating with mono and hybrid nanofluids. *Sustainable Energy Technologies and Assessments*, 26:105–115, 2018. https://doi.org/10.1016/j.seta.2017.10.005.

[196] Oveepsa Chakraborty, Biplab Das, Rajat Gupta, and Sumita Debbarma. Heat transfer enhancement analysis of parabolic trough collector with straight and helical absorber tube. *Thermal Science and Engineering Progress*, 20:100718, 2020. https://doi.org/10.1016/j.tsep.2020.100718.

[197] John A Duffie and William A Beckman. *Solar engineering of thermal processes*. John Wiley & Sons, 2013. http://refhub.elsevier.com/S0360-5442(17)31704-8/sref14.

[198] Adrian Bejan and Peter A Pfister Jr. Evaluation of heat transfer augmentation techniques based on their impact on entropy generation. *Letters in heat and mass transfer*, 7(2):97–106, 1980. https://doi.org/10.1016/0094-4548(80)90037-5.

[199] Oscar A López-Núñez, J Arturo Alfaro-Ayala, OA Jaramillo, JJ Ramírez-Minguela, J Carlos Castro, Cesar E Damian-Ascencio, and Sergio Cano-Andrade. A numerical analysis of the energy and entropy generation rate in a Linear Fresnel Reflector using computational fluid dynamics. *Renewable Energy*, 146:1083–1100, 2020. https://doi.org/10.1016/j.renene.2019.06.144.

[200] Fabian Kock and Heinz Herwig. Local entropy production in turbulent shear flows: A high-reynolds number model with wall functions. *International journal of heat and mass transfer*, 47(10-11):2205–2215, 2004. https://doi.org/10.1016/j.ijheatmasstransfer.2003.11.025.

[201] R. Petela. Exergy of heat radiation. *Journal of Heat Transfer*, 86(2):187–192, 1964. https://doi.org/10.1115/1.3687092.

[202] ASME. Standard for verification and validation in computational fluids and heat transfer, 2009. Standard No. ASME V&V 20–2009.

[203] Cecilia Piatti, Alex Hicks, Eleonora Gajetti, Caleb Ward, Mahyar Pourghasemi, Luca Marocco, Laura Savoldi, and Nima Fathi. Verification and validation of turbulence modeling of flow through triply periodic minimal surfaces porous structures. *Proceedings of the ASME 2024 Verification, Validation, and Uncertainty Quantification Symposium*, May 15-17, 2024, College Station, Texas. https://doi.org/10.1115/VVUQ2024-133017.

[204] Arsham Mortazavi, AL Avila-Marin, Hossein Ebadi, Eleonora Gajetti, Cecilia Piatti, Luca Marocco, and Laura Savoldi. Experimental investigation of triply periodic minimal surfaces for high-temperature solar receivers. *Case Studies in Thermal Engineering*, 60:104771, 2024. https://doi.org/10.1016/j.csite.2024.104771.

[205] Jian Li, José Gonzalez-Aguilar, Carlos Pérez-Rábago, Hussein Zeaiter, and Manuel Romero. Optical analysis of a hexagonal 42kwe high-flux solar simulator. *Energy Procedia*, 57:590–596, 2014. https://doi.org/10.1016/j.egypro.2014.10.213.

[206] J Li, J Gonzalez-Aguilar, and M Romero. Line-concentrating flux analysis of 42kwe high-flux solar simulator. *Energy procedia*, 69:132–137, 2015. https://doi.org/10.1016/j.egypro.2015.03.016.

[207] David Jonathan D'souza. *Application of compact flow channel geometries to pressurised solar receivers: a numerical and experimental analysis*. PhD thesis, UNED. Universidad Nacional de Educación a Distancia, 2023.

[208] Hossein Ebadi, Antonio Cammi, Rosa Difonzo, José Rodríguez, and Laura Savoldi. Experimental investigation on an air tubular absorber enhanced with raschig rings porous medium in a solar furnace. *Applied Energy*, 342:121189, 2023. https://doi.org/10.1016/j.apenergy.2023.121189.

[209] J.P. Holman. *Experimental Methods for Engineers*. McGraw-Hill Education, 2011.

[210] Sam Catchpole-Smith, Richard RJ Sélo, AW Davis, IA Ashcroft, Christopher J Tuck, and AJAM Clare. Thermal conductivity of tpms lattice structures manufactured via laser powder bed fusion. *Additive Manufacturing*, 30:100846, 2019. https://doi.org/10.1016/j.addma.2019.100846.

[211] Pin-Yang Wang, Hong-Yang Guan, Zhen-Hua Liu, Guo-San Wang, Feng Zhao, and Hong-Sheng Xiao. High temperature collecting performance of a new all-glass evacuated tubular solar air heater with u-shaped tube heat exchanger. *Energy Conversion and Management*, 77:315–323, 2014. https://doi.org/10.1016/j.enconman.2013.08.019.

[212] Magdalena Nemś and Jacek Kasperski. Experimental investigation of concentrated solar air-heater with internal multiple-fin array. *Renewable Energy*, 97:722–730, 2016. https://doi.org/10.1016/j.renene.2016.06.038.

[213] İnci Türk Toğrul and Dursun Pehlıvan. The performance of a solar air heater with conical concentrator under forced convection. *International journal of thermal sciences*, 42(6):571–581, 2003. https://doi.org/10.1016/S1290-0729(03)00023-1.

[214] Réné Tchinda. Thermal behaviour of solar air heater with compound parabolic concentrator. *Energy conversion and Management*, 49(4):529–540, 2008. https://doi.org/10.1016/j.enconman.2007.08.004.

[215] Afaq Jasim Mahmood. Thermal evaluation of a double-pass unglazed solar air heater with perforated plate and wire mesh layers. *Sustainability*, 12(9):3619, 2020. https://doi.org/10.3390/su12093619.

[216] Arsham Mortazavi and Mehran Ameri. Conventional and advanced exergy analysis of solar flat plate air collectors. *Energy*, 142:277–288, 2018. https://doi.org/10.1016/j.energy.2017.10.035.

[217] MK Gupta and SC Kaushik. Performance evaluation of solar air heater for various artificial roughness geometries based on energy, effective and exergy efficiencies. *Renewable Energy*, 34(3):465–476, 2009. https://doi.org/10.1016/j.renene.2008.06.001.

[218] H Hüseyin Öztürk and Y Demirel. Exergy-based performance analysis of packed-bed solar air heaters. *International Journal of Energy Research*, 28(5):423–432, 2004. https://doi.org/10.1002/er.974.

[219] Arsham Mortazavi, Hossein Ebadi, Cecilia Piatti, Eleonora Gajetti, Luca Marocco, and Laura Savoldi. Numerical Modelling of Solar Receivers Equipped With TPMS Structures. In *SolarPACES Conference Proceedings*, volume 3, 2024. https://doi.org/10.52825/solarpaces.v3i.2416.

[220] Hossein Ebadi, Antonio Cammi, Nima Fathi, and Laura Savoldi. Heat transfer enhancement on CSP tubular receivers using partially filled Raschig Ring porous inserts: A numerical study. *Solar Energy*, 297:113635, 2025. https://doi.org/10.1016/j.solener.2025.113635.

[221] FS Boydağ. The optical properties of some steel surfaces with different surface preparations for high temperature use. *Solar energy materials*, 13(3):185–195, 1986. https://doi.org/10.1016/0165-1633(86)90017-1.

[222] Marco Cantone, Mattia Cagnoli, Jesus Fernandez Reche, and Laura Savoldi. One-side heating test and modeling of tubular receivers equipped with turbulence promoters for solar tower applications. *Applied Energy*, 277:115519, 2020. https://doi.org/10.1016/j.apenergy.2020.115519.

[223] Yonggyun Yu, Taeil Hur, Jaeho Jung, and In Gwun Jang. Deep learning for determining a near-optimal topological design without any iteration. *Structural and Multidisciplinary Optimization*, 59:787–799, 2019. https://doi.org/10.1007/s00158-018-2101-5.

[224] Fernando V Senhora, Heng Chi, Yuyu Zhang, Lucia Mirabella, Tsz Ling Elaine Tang, and Glaucio H Paulino. Machine learning for topology optimization: Physics-based learning through an independent training strategy. *Computer Methods in Applied Mechanics and Engineering*, 398:115116, 2022. https://doi.org/10.1016/j.cma.2022.115116.

[225] Alex Halle, Lucio Flavio Campanile, and Alexander Hasse. An artificial intelligence–assisted design method for topology optimization without pre-optimized training data. *Applied Sciences*, 11(19):9041, 2021. https://doi.org/10.3390/app11199041.

[226] Seungyeon Shin, Dongju Shin, and Namwoo Kang. Topology optimization via machine learning and deep learning: a review. *Journal of Computational Design and Engineering*, 10(4):1736–1766, 2023. https://doi.org/10.1093/jcde/qwad072.

[227] Qiyin Lin, Jun Hong, Zheng Liu, Baotong Li, and Jihong Wang. Investigation into the topology optimization for conductive heat transfer based on deep learning approach. *International Communications in Heat and Mass Transfer*, 97:103–109, 2018. https://doi.org/10.1016/j.icheatmasstransfer.2018.07.001.

[228] Zeyu Zhang, Yu Li, Weien Zhou, Xiaoqian Chen, Wen Yao, and Yong Zhao. TONR: An exploration for a novel way combining neural network with topology optimization. *Computer Methods in Applied Mechanics and Engineering*, 386:114083, 2021. https://doi.org/10.1016/j.cma.2021.114083.

[229] Vahid Keshavarzzadeh, Mitra Alirezaei, Tolga Tasdizen, and Robert M Kirby. Image-based multiresolution topology optimization using deep disjunctive normal shape model. *Computer-Aided Design*, 130:102947, 2021. https://doi.org/10.1016/j.cad.2020.102947.

[230] Baotong Li, Congjia Huang, Xin Li, Shuai Zheng, and Jun Hong. Non-iterative structural topology optimization using deep learning. *Computer-Aided Design*, 115:172–180, 2019. https://doi.org/10.1016/j.cad.2019.05.038.

[231] Changyu Deng, Yizhou Wang, Can Qin, Yun Fu, and Wei Lu. Self-directed online machine learning for topology optimization. *Nature communications*, 13(1):388, 2022. https://doi.org/10.1038/s41467-021-27713-7.

[232] Audrey Gaymann and Francesco Montomoli. Deep neural network and Monte Carlo tree search applied to fluid-structure topology optimization. *Scientific reports*, 9(1):15916, 2019. https://doi.org/10.1038/s41598-019-51111-1.

Appendix A

Local Entropy Generation for the Turbulent Studies

As noted in Section 4.1.2, to verify the validity of the laminar flow assumption, the cases were also investigated using a RANS turbulent model. The procedure for obtaining model equations for entropy generation in turbulent shear flows is well documented by Kock and Herwig [200]. In this approach, four types of entropy generation are identified:

- $\dot{S}_{\mathrm{PRO},\overline{D}}$ = Entropy generation rate by direct (viscous) dissipation
- $\dot{S}_{\mathrm{PRO},D'}$ = Entropy generation rate by turbulent dissipation,
- $\dot{S}_{\mathrm{PRO},\overline{C}}$ = Entropy generation rate by heat transfer with mean temperature gradients,
- $\dot{S}_{\mathrm{PRO},C'}$ = Entropy generation rate by heat transfer with fluctuating temperature gradients.

Here, $\dot{S}_{\mathrm{PRO},\overline{D}}$ refers to entropy generation by dissipation in the mean flow field, $\dot{S}_{\mathrm{PRO},D'}$ is caused by fluctuations in the flow field, $\dot{S}_{\mathrm{PRO},\overline{C}}$ arises from heat transfer due to time-averaged temperature gradients, and $\dot{S}_{\mathrm{PRO},C'}$ originates from heat transfer due to fluctuating temperature gradients.

Although the calculation of the mean terms is straightforward, the fluctuating contributions must be modeled in a way that allows their evaluation using results

from a RANS turbulence model. Kock and Herwig [200] modeled the fluctuating parts as:

$$\dot{S}_{\mathrm{PRO},D'} = \frac{\rho\,\varepsilon}{\overline{T}}, \tag{A.1}$$

$$\dot{S}_{\mathrm{PRO},C'} = \frac{\alpha_t}{\alpha}\frac{k}{\overline{T}^2}\left[\left(\frac{\partial\overline{T}}{\partial x}\right)^2 + \left(\frac{\partial\overline{T}}{\partial y}\right)^2 + \left(\frac{\partial\overline{T}}{\partial z}\right)^2\right], \tag{A.2}$$

where ε, the dissipation rate of turbulent kinetic energy, is obtained from a κ–ε analysis. In Equation A.2, α denotes the thermal diffusivity, while α_t represents the eddy (or turbulent) diffusivity.

The mean values of entropy generation can be obtained from:

$$\begin{aligned}\dot{S}_{\mathrm{PRO},\overline{D}} = \frac{\mu}{\overline{T}}\Bigg[2\left(\left(\frac{\partial\overline{u}}{\partial x}\right)^2 + \left(\frac{\partial\overline{v}}{\partial y}\right)^2 + \left(\frac{\partial\overline{w}}{\partial z}\right)^2\right) \\ + \left(\frac{\partial\overline{u}}{\partial y} + \frac{\partial\overline{v}}{\partial x}\right)^2 + \left(\frac{\partial\overline{u}}{\partial z} + \frac{\partial\overline{w}}{\partial x}\right)^2 + \left(\frac{\partial\overline{v}}{\partial z} + \frac{\partial\overline{w}}{\partial y}\right)^2\Bigg]\end{aligned} \tag{A.3}$$

$$\dot{S}_{\mathrm{PRO},\overline{C}} = \frac{k}{\overline{T}^2}\left[\left(\frac{\partial\overline{T}}{\partial x}\right)^2 + \left(\frac{\partial\overline{T}}{\partial y}\right)^2 + \left(\frac{\partial\overline{T}}{\partial z}\right)^2\right]. \tag{A.4}$$

Accordingly, viscous entropy generation and heat-transfer entropy generation are defined as:

$$\dot{S}_{\mathrm{Viscous}} = \dot{S}_{\mathrm{PRO},\overline{D}} + \dot{S}_{\mathrm{PRO},D'}, \tag{A.5}$$

$$\dot{S}_{\mathrm{Heat}} = \dot{S}_{\mathrm{PRO},\overline{C}} + \dot{S}_{\mathrm{PRO},C'}, \tag{A.6}$$

and the total entropy generation is obtained as:

$$\dot{S}_{\mathrm{gen}} = \dot{S}_{\mathrm{Viscous}} + \dot{S}_{\mathrm{Heat}}. \tag{A.7}$$

Each component of entropy generation was implemented as a field function in *STAR-CCM+*, and the total entropy generation was calculated by volume integration of these field functions.

Appendix B

Benchmarking the Hydraulic Model of the Tubular Receivers against Experimental Data

Due to the lack of experimental data, only the hydraulic performance of the tubular receiver equipped with TPMS lattices was compared with the experimental results of Piatti et al. [203]. In their study, they investigated a pipe incorporating the same TPMS lattices, material, and dimensions as those used in the present work. Subcooled water flowed through the pipes at different mass flow rates. To ensure a fair comparison, the simulations with a lattice unit-cell size of 20 mm were performed using subcooled water and the same mass flow rates as in Ref. [203]. The numerical results were obtained using the Lag EB κ–ε turbulence model.

The comparison is shown in Figure B.1. The results demonstrate very good agreement in terms of pressure drop at lower mass flow rates, with deviations appearing as the flow rate increases. It should be noted that in Ref. [203], the pressure transducers were placed before and after the fittings connecting the mock-up to the inlet and outlet pipes. Therefore, the discrepancies at higher flow rates may stem from additional pressure drops due to minor losses in these fittings. Since the simulations in Section 4.1 were carried out in the laminar regime, they appear to provide accurate predictions for such low Reynolds numbers.

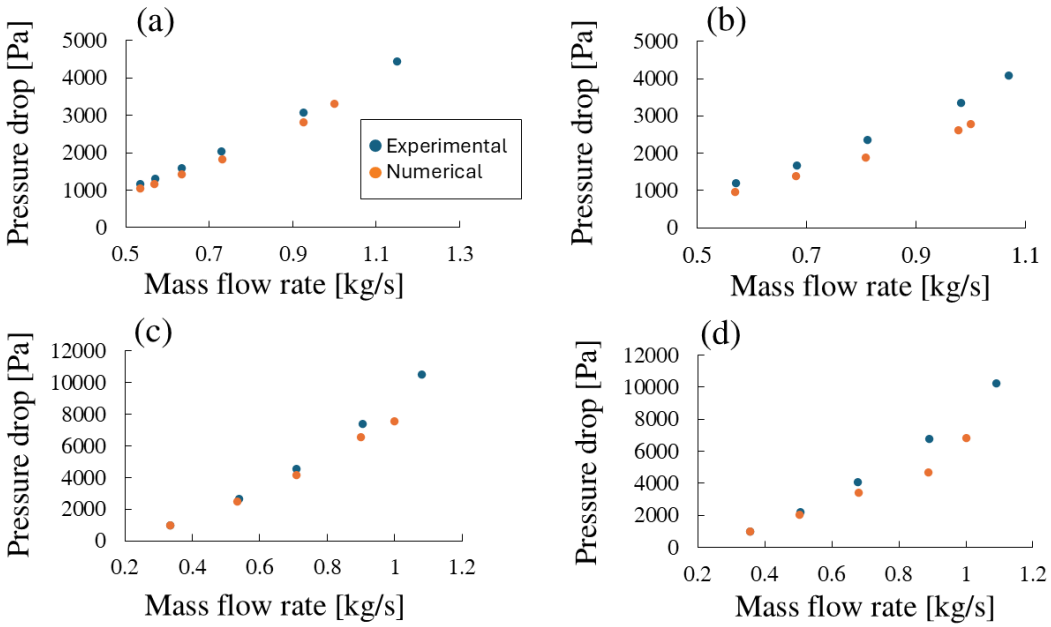


Fig. B.1 Comparison of the hydraulic model of the TPMS-equipped tubular receivers with experimental data of Piatti et al. [203]: for (a) Diamond, (b) Gyroid, (c) SplitP and (d) Lidinoid lattices with unit cell-size of 20 mm.